Phonon and spin dynamics of $(VO)_2P_2O_7$

vorgelegt von
Diplom-Physiker
Uwe Kuhlmann
aus Berlin

von der Fakultät II - Mathematik und Naturwissenschaften
der Technischen Universität Berlin
zur Erlangung des akademischen Grades

Doktor der Naturwissenschaften
– Dr. rer.nat. –

genehmigte Dissertation

Promotionsausschuss:

Vorsitzender:	Prof. Dr. Andreas Knorr
Berichter:	Prof. Dr. Christian Thomsen
Berichter:	Prof. Dr. Wolfgang Richter

Tag der wissenschaftlichen Aussprache: 9 August 2005

Berlin 2005
D 83

Zusammenfassung

Gegenstand der vorliegenden Arbeit ist die Übergangsmetallverbindung $(VO)_2P_2O_7$ (VPO). In dieser Verbindung ist vom elektronischen Standpunkt aus gesehen ein eindimensionales Spinsystem, eine antiferromagnetische Spinkette realisiert. Die phononischen Anregungen (Gitterschwingungen) und Anregungen des Spinsystems sowie ihre gegenseitige Wechselwirkung als Spin-Phononkopplung wurden mit Raman- und Infrarotspektroskopie untersucht. Die Ramanmessungen wurden in einem weiten Temperaturbereich (2-300 K) durchgeführt, wobei insbesonders Messungen bei tiefen Temperaturen im Vordergrund standen, weil nur hier die magnetischen Eigenschaften von VPO untersucht werden können. Die Infrarot-Reflexionsspektroskopie diente hauptsächlich zur Vervollständigung der Phononenspektren von VPO und wurde bei Raumtemperatur durchgeführt. Um insbesondere den Einfluß von Bindungswinkeln und Bindungslängen auf die magnetischen Anregungen und die Spin-Phononkopplung zu untersuchen wurden Ramanmessungen unter hohem hydrostatischen Druck in einer Diamantstempel-Druckzelle durchgeführt. Diese Messungen erfolgten ebenfalls bei variablen Temperaturen bis herab zu ca. 4 K.

VPO kristallisiert in zwei verschiedenen Modifikationen, deren wesentlicher Unterschied ist daß in der Normal-Phase (AP-VPO) zwei kristallographisch nichtäquivalente Spinkettensysteme vorliegen, die in der zweiten, der Hochdruck-Phase (HP-VPO) aufgrund höherer Symmetrie zu einem Spinkettensystem entarten. Grundlage der Untersuchung der Gitterdynamik stellt eine Normalmodenanalyse für beide Phasen von VPO dar. Hierzu wurde ein Faktorgruppenanalyse der Strukturen durchgeführt und die möglichen Eigenmoden nach Symmetrie und Charakter der Schwingung klassifiziert. Darauf aufbauend konnte eine Zuordnung der beobachteten Phononenlininen zu Eigenmoden der Gitter weitgehend durchgeführt werden. Des weiteren wurde in Weiterentwicklung eines aus der Literatur bekannten Kraftfeldes die Eigenmoden von AP-VPO und HP-VPO mit Molekulardynamik berechnet. Hierbei war die Modellierung der ungewöhnlichen Gitteranharmonizitäten und der für die Spin-Phononkopplung in Frage kommenden Phononen beabsichtigt. Obwohl das Phononenspektrum von AP-VPO und HP-VPO im allgemeinen widergegeben werden konnte und weitere Informationen für die Zuordnung der Moden erlangt wurden, ist dieser Projektteil noch nicht abgeschlossen. Es zeigte sich daß das verwendete Kraftfeld einige Aspekte der Gitterdynamik von VPO nicht wiedergeben kann, hier muss noch weiter geforscht werden.

Wichtigstes Ergebnis der Ramanmessungen an AP-VPO war der spektroskopische Nachweis der zweiten Singlet-Triplet-Anregung (Spin-Gap) bei $\approx$ 90 cm-1 zusätzlich zu der vorher beobachteten bei $\approx$ 45 cm^{-1}. Zusammengenommen liefern sie ein starkes

Argument zugunsten des Modells zweier unabhängiger Spinketten in AP-VPO, welches mittlerweile allgemein anerkannt wird. Die bei niedrigen Energien beobachtbare starke Wechselwirkung bestimmter Phononen mit dem Spinsystem – starke Energieverschiebung und Linienverbreiterung mit zunehmender Temperatur – wurde eingehend untersucht, mit vorhandenen Modellrechnungen verglichen und neu bewertet. Ramanmessungen unter hohen Druck an HP-VPO erlaubten hier die Identifizierung einer Mode, die der Spin-Phonon-Mode in AP-VPO entspricht.

Ein weiteres wesentliches Resultat ergab sich aus der Untersuchung von HP-VPO. Beide Kristallphasen sind strukturell sehr ähnlich so das 1. eine Singlet-Triplet-Anregungen bei ca. 30 cm^{-1}, herrührend vom Spinkettensystem erwartet wurde und 2. das Auftreten von ähnlich wie in AP-VPO mit dem Spinsystem wechselwirkenden Phononen bei niedrigen Wellenzahlen. Der Spin-Gap konnte nicht beobachtet werden, es ist davon auszugehen das die Streuintensität dieser Anregung, die schon bei AP-VPO sehr schwach war, in HP-VPO zu gering ist um mit Ramanspektroskopie beobachtet werden zu können. Überraschend war die starke und von AP-VPO sehr deutlich verschiedene Wechselwirkung einiger Phononen um 150 cm^{-1} mit dem Spinsystem, welches sich im nur bei tiefen Temperaturen zu beobachtenden Fano-Linienprofil der Moden zeigte. Die Messungen unter hohen Druck zeigten u.a. daß die beobachtete Wechselwirkung sensitiv auf Gitterverzerrungen reagiert und ab ca. 4 GPa vollständig unterdrückt werden kann. Die genauere Analyse ergab, dass sich dieses Verhalten nicht mit dem Modell vereinbaren lässt, welches für die Spin-Phononkopplung in AP-VPO entwickelt wurde. Die Diskussion über eine mögliche Alternativerklärung ist noch nicht abgeschlossen.

Schliesslich wurden in beiden Kristallphasen bei höheren Energien (um 900 cm^{-1}) eine ungewöhnliche Gitteranharmonizität der Vanadyl-Bindung beobachtet, deren Schwingungsfrequenz mit sinkender Temperatur abnimmt. Diese Anharmonizität, die etwa gleichstark auch in HP-VPO zu beobachten ist, kann durch die stark anisotrope Gitterkontraktion bei abnehmender Temperatur und damit einhergehend durch eine zunehmende Zwischengitterebenen-Wechselwirkung beschrieben werden.

List of publications

Raman scattering of magnetic excitations of independent antiferromagnetic spin chains in $(VO)_2P_2O_7$*.*
U. Kuhlmann, C. Thomsen, A. V. Prokofiev, F. Büllesfeld, E. Uhrig, and W. Assmus
Phys. Rev. B **62** (2000) 12262.

Polarized Raman and infrared vibrational analysis of $(VO)_2P_2O_7$ *single crystals.*
U. Kuhlmann, C. Thomsen, A. V. Prokofiev, F. Büllesfeld, E. Uhrig, and W. Assmus
Physica B **301** (2001) 276.

Phonon anomalies in the two phases of the low-dimensional spin compound $(VO)_2P_2O_7$*.*
U. Kuhlmann, C. Thomsen, A. V. Prokofiev, F. Büllesfeld, E. Uhrig, M. Anton, C. Gross, and W. Assmus
Phys. Rev. B **66** (2002) 064420.

Spin-phonon coupling in the high pressure phase of the low-dimensional spin compound $(VO)_2P_2O_7$
U. Kuhlmann, C. Thomsen, A. V. Prokofiev, F. Büllesfeld, E. Uhrig, M. Anton, C. Gross, and W. Assmus
phys. stat. sol. (a) **196** (2003) 185.

Polarized far-infrared and Raman spectra of $SrCuO_2$ *single crystals.*
Z. Popović, M. Konstantinović, R. Gajić, C. Thomsen, U. Kuhlmann, and A. Vietkin
Physica C **351** (2001) 386.

Magnetic exitations in $SrCu_2O_3$*: a Raman scattering study.*
A. Gößling, U. Kuhlmann, C. Thomsen, A. Löffert, C. Gross, and W. Assmus
Phys. Rev. B **67** (2003) 52403.

Raman response of magnetic excitations in cuprate ladders and planes.
K. Schmidt, A. Gössling, U. Kuhlmann, C. Thomsen, A. Löffert, C. Gross, and W. Assmus
Phys. Rev. B **72** (2005) 094419.

Contents

1. Introduction

The physics of low dimensions is an area of principal interest in solid state physics and many important discoveries in the recent years are related to the reduced dimensionality of the systems in question, to name only exemplarily the quantum hall effect or quantum dots. The concept of one-dimensional metals lead to the proposition of a novel quantum state, the Luttinger Liquid, and the low dimensional magnetism of cuprate sheets plays a crucial role for the explanation of high-temperature superconductivity. In fact low-dimensional magnetism has attracted research since Bethe theoretically examined the one-dimensional spin chain in 1931. Ensuing theoretical studies revealed much of the peculiar properties of these systems, their excitation spectrum and phase transitions as e.g. the Peierls transition of one-dimensional metals and its counterpart in isolating Heisenberg spin-chain compounds, the spin-Peierls transition. On the experimental side, verification of these theoretical predictions is often complicated by the fact that the number of systems exhibiting the effects purely is limited since most natural structures are only approximations of theoretical model systems. In their initial work on the magnetic properties of $(VO)_2P_2O_7$ (VPO) in 1987 Johnston *et al.* noted that "There exist roughly twenty compounds for which the theoretical predictions of the physical properties of the alternating Heisenberg antiferromagnetic chain have been confirmed ..." [1].

The orthorhombic compound vanadyl pyrophosphate (VPO) has been known for long owing to its catalytic properties. It is employed as a highly selective catalyst in the oxidation of n-butane to maleic anhydride,– an industrial process of fundamental importance since the latter compound is the starting material for the production of resins, lubricants, pharmaceuticals and other. Despite the long-time prevalent application of VPO as a catalyst the reaction mechanism and the active center of VPO is still a matter of debate [2].

In vanadium oxides V is often found in oxidation states 4+ and therefore possesses an electron spin $\frac{1}{2}$. Johnston and coworkers were led by structural considerations when they examined VPO among other compounds bearing the potential for low-dimensional magnetism and expected the electron spins to interact according to a spin-ladder topology. Surprisingly they found that the temperature dependence of the magnetic susceptibility was accurately described by the predictions for a spin-$\frac{1}{2}$ alternating antiferromagnetic Heisenberg chain. This contradiction was later resolved by inelastic neutron scattering (INS) by which the ladder geometry was unequivocally disproved. These experiments revealed a second excitation at an energy just below $2\Delta_{01}$, in addition to the expected magnon with magnetic zone-center energy gap $\Delta_{01} = 3.1$ meV. The examination of this feature by Raman scattering will be one of the topics in the focus of this work.

Another focal point will be the investigation of the phonon spectrum of VPO. Besides the assignment of the observed lines to vibrations of the lattice certain phonons show-

ing rather unusual anharmonicities were examined closely by temperature dependent Raman scattering and by Raman scattering under high hydrostatic pressure. Most of the observed phonon anharmonicities are pure lattice effects but for some low-energy phonons the anharmonic effects are due to unusual strong spin-phonon coupling.

Only recently a second crystal modification of VPO has been grown under high pressure conditions denoted high pressure(HP)-VPO, in contrast to the ambient pressure phase AP-VPO. Both phases are very similar. HP-VPO is orthorhombic, too, but has a higher symmetry. First measurements of the magnetic susceptibility indicated that HP-VPO is an antiferromagnetic alternating Heisenberg chain, too, with a singlet-triplet gap of ≈ 1.9 meV. The creation of HP-VPO gave the opportunity to study two closely related spin-chain systems with only small structural differences and a significant part of the work is devoted to the comparison of both compounds and the study of how these structural differences affect the vibrational and magnetic properties of VPO.

The thesis is organized as follows: In the following Chapter 2 I will present some of the theoretical basics necessary for the discussion of one dimensional spin chain systems and for the Raman experiments. After a brief presentation of the experimental setup in Chapter 3 the next Chapter 4 discusses the structure of both phases of VPO and summarizes the state of knowledge of their magnetic properties. In Chapter 5 the discussion of the structure of VPO will be extended from a group theoretical angle and a full factor group analysis on both crystal phases will be presented to reveal the possible lattice eigenmodes.

The experimental part of the work starts with Chapter 6 where I give an overview of the experiments performed. Chapter 7 then deals with the results of the experiments as far as the lattice vibrations are concerned and discusses the assignment of the observed phonon lines to the eigenmodes presented in the foregoing Chapter. The following Chapter 8 is — in a sense — of experimental character, too. Here I will report on the results of a simulation of the lattice dynamics of VPO by molecular dynamics. In the final experimental Chapter 9 the focus is on the discussion of light scattering of magnetic excitations and the strong spin-phonon coupling found in both phases of VPO. A summary of the main results of this work will be given in 10.

2. Theory

In this chapter I will summarize the theory, in particular that of low dimensional magnets which is the essential background for the interpretation of the spectroscopic results. Far from comprehensive it is rather meant as a collection of basic theorems and concepts for the purpose of understanding of the later chapters. Since VPO is a good insulator, I will restrict the discussion in respect to the magnetic properties to insulating compounds and therefore treat magnetic centers always as localized moments.

2.1. Exchange Interaction

When the phenomenon of collective magnetism, i.e. ferromagnetism or antiferromagnetism was considered within the framework of the Maxwell theory of electromagnetism and one tried to give on that basis a justification for e.g. the Curie- or Néel-temperature, which is in many cases in the range of some 10^2 Kelvin, it became soon clear that this does not apply. The inter-atomic fields which would be required to maintain long range order over thermal disorder even at hundreds of Kelvin are much stronger than that generated from the supposed elementary magnetic dipoles, whether they are orbital moments or electron spins. This shall be illustrated by a short textbook calculation [3]: The dipole-dipole interaction energy between two magnetic moments is

$$E(\mathbf{r}) = -\frac{\mu_0}{4\pi r^3}\left[\boldsymbol{\mu_1}\cdot\boldsymbol{\mu_2} - \frac{3}{r^2}(\boldsymbol{\mu_1}\cdot\mathbf{r})(\boldsymbol{\mu_2}\cdot\mathbf{r})\right]. \tag{2.1}$$

If we assume parallel electron spins and a distance $\boldsymbol{r} \approx 1.5$ Å with $\mid \boldsymbol{\mu} \mid = \mu_{\mathrm{Bor}}$ then 2.1 gives an energy of ≈ 0.1 meV, which corresponds to 1.2 K. Hence any long-range order originating from dipole-dipole interaction cannot exist but at very low temperatures, at higher temperatures it would immediately be destroyed by thermal motion. The explanation for the interaction between electronic spins which allows for collective magnetic phenomena was eventually found with the development of quantum mechanics.

2.1.1. Direct Exchange

In insulating compounds the dominant force between electron spins is generated by the *exchange interaction*. This form of interaction was proposed independently by Heisenberg and Dirac in 1926 [4, 5], only short after the concept of electron spin had been suggested by Uhlenbeck and Goudsmit in 1925 [6]. The exchange interaction is of complete electrostatic nature and is a consequence of the fact that the electrons, as well as other quantum objects of a quantum mechanical system are non-distinguishable particles. This fact has lead to the notion of two different classes of microscopic particles, to

which the particles belong depending on their spin being either even or odd, the Bosons and Fermions, respectively. Bosons have to be described by symmetric wavefunctions. The Fermions, to which the electrons as spin-$\frac{1}{2}$ particles belong have to be described by antisymmetric wavefunctions. This crucial point gives rise to the fundamental Pauli-exclusion principle: the quantum-state of electrons of a quantum mechanical system differs at least by one quantum number, it is not possible to measure two electrons of the same quantum system in exactly the same state.
The electron spins of neighboring magnetic ions interact through their overlapping electronic orbitals, as depicted in Fig. 2.1a. Following the argumentation in [7] the expectation value of their mutual Coulomb interaction is

$$H_{\mathrm{Coul}} = \frac{1}{2}\int\int \psi^*(\boldsymbol{r_1})\psi^*(\boldsymbol{r_2})\frac{e^2}{\mid \boldsymbol{r_1}-\boldsymbol{r_2} \mid}\psi(\boldsymbol{r_2})\psi(\boldsymbol{r_1})d\tau_1 d\tau_2. \tag{2.2}$$

The antisymmetric nature of the electron wavefunction $\psi(\boldsymbol{r}_1, \boldsymbol{r}_2)$ leads, after some manipulation, to a spin-dependent component in the Hamiltonian which is given by

$$H_{\mathrm{Coul}} = C_{ij} - 2J_{ij}(\boldsymbol{S}_i\boldsymbol{S_j} + \frac{1}{4}) \quad \text{, where} \tag{2.3}$$

$$C_{ij} = \frac{1}{2}\int\int \phi_i^*(\boldsymbol{r_1})\phi_j^*(\boldsymbol{r_2})\frac{e^2}{\mid \boldsymbol{r_1}-\boldsymbol{r_2} \mid}\phi_i(\boldsymbol{r_1})\phi_j(\boldsymbol{r_2})d\tau_1 d\tau_2 \tag{2.4}$$

is the usual Coulomb integral and

$$J_{ij} = \frac{1}{2}\int\int \phi_i^*(\boldsymbol{r_1})\phi_j^*(\boldsymbol{r_2})\frac{e^2}{\mid \boldsymbol{r_1}-\boldsymbol{r_2} \mid}\phi_i(\boldsymbol{r_2})\phi_j(\boldsymbol{r_1})d\tau_1 d\tau_2 \tag{2.5}$$

is the exchange integral. $\phi_{i,j}$ and $\boldsymbol{S}_{i,j}$ are the angular and the spin part of the electron wavefunctions, respectively. The exchange integral is always positive [7] and therefore the direct exchange coupling leads to a parallel spin arrangement, thus to ferromagnetism.

It should be annotated that the Heisenberg model of the direct exchange interaction is of more abstract importance since only few compounds exhibit ferromagnetism from overlapping electron orbitals of localized magnetic ions. The prototypic ferromagnetic metal iron e.g. has its magnetic properties due to the strongly correlated *itinerant* $3d$-electrons. However, the magnetic properties of conducting materials is beyond the scope of this work.

2.1.2. Indirect Exchange - Superexchange

A closer examination of compounds with collective magnetic phenomena revealed that the direct exchange mechanism as outlined above is rather the exception and, since the integral J_{ij} is always positive, it cannot account for antiferromagnetism. In many compounds which exhibit antiferromagnetism the magnetic ions are separated from each other by non-magnetic ions, sketched in fig 2.1b. The direct exchange interaction would be too weak and is therefore precluded. As an extension of ideas already formulated by Kramers in 1934 [8] Anderson developed a theory of the superexchange mechanism [9].

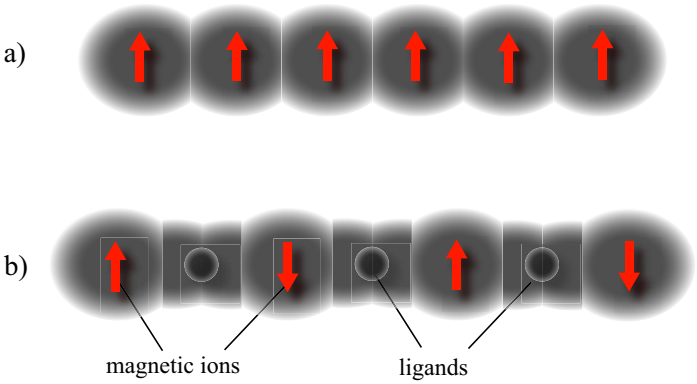

Figure 2.1.: a) Direct exchange interaction by orbital overlap of magnetic ions. b) Superexchange through overlapping orbitals of non-magnetic ligands.

Its principle shall be explained by the the example of the situation in CaMnO3 [10]. In CaMnO3 the $3d$-orbitals of the Mn^{4+} ions are filled with three electrons. They overlap with the p_σ orbitals of the oxygen atoms and one of the p_σ-electrons hops over to a Mn^{4+}-ion. The remaining unpaired p electron then enters a direct exchange with the other Mn^{4+}-ion and the whole process thus gives an effective spin correlation between the two Mn sites. Essential for this type of interaction is the strong orbital overlap between the magnetic ion and the mediating non-magnetic ligands. The role of the spatial arrangement of the atoms involved in the superexchange is expressed by the Goodenough-Kanamori-Anderson rule [11, 12]: a 180 superexchange path renders $J_{ij} < 0$ and therefore favors antiferromagnetic order whereas a 90 exchange path leads to $J_{ij} > 0$, i.e. ferromagnetic coupling. A notable exception to this rule is the spin-Peirls compound CuGeO3, which is antiferromagnetic despite having bond angles of ≈ 90 between the Cu-ions and the oxygen ligands [13].
The superexchange interaction is not restricted to the case of only one ligand being located between the magnetic ions. Provided the orbital overlap is strong enough a whole chain of ligands can in principle mediate the exchange interaction, thus establishing a super-superexchange interaction,– and I shall show below that this is the case in VPO.

If only the magnetic properties of a crystal are being considered, it is sufficient to examine only the magnetic part of the Hamiltonian in 2.3 as $H_{ij} = -2J_{ij}\boldsymbol{S}_i \cdot \boldsymbol{S}_j$ the Hamiltonian of two spins. By summing over all pairs of spins of the crystal we obtain the complete spin-Hamiltonian

$$H = -2 \sum_{<i,j>} J_{i,j} \boldsymbol{S}_i \cdot \boldsymbol{S}_j \tag{2.6}$$

or, with the spin components explicitely given

$$H = -2 \sum_{<i,j>} J_{i,j} \left[a S_i^x S_j^x + b S_i^y S_j^y + c S_i^z S_j^z \right] . \tag{2.7}$$

The isotropic case when $a = b = c$ is the *Heisenberg* model and it is the best approximation for most real systems. The anisotropic cases $a = b = 0$ (Ising-model) and $a = b, c = 0$ (XY-model) are often used in calculations due to their greater simplicity.

2.2. The one-dimensional antiferromagnetic Spin chain

2.2.1. Magnetic Order - Néel-state versus RVB-state

Before the discussion of the properties of the one-dimensional antiferromagnetic spin-chain I want to introduce briefly two general concepts of the description of low-dimensional quantum-antiferromagnets. For a more comprehensive discussion see [14]. If a quantum system orders antiferromagnetically, the crystal can be conceived as divided into two sublattices **A** and **B** with finite sub-lattice magnetization $< \boldsymbol{S}_{\mathbf{A}} > - < \boldsymbol{S}_{\mathbf{B}} > \neq 0$. This is the well known Néel-state. The long-range order such formed poses a break of the rotational symmetry of the spins. For systems where a continuous symmetry is broken spontaneously infinitesimal low lying excitations are predicted, the so called Goldstone bosons [15]. Hence, the excitation spectrum of such a quantum system is gapless.

A counterdraft to the Néel-state is the Resonating-Valence-Bond (RVB)-state. Here the whole system is conceived as a superposition of singlet $S = 0$ product states [16, 17], i.e. all spins are combined into pairs or *spin-dimers*, respectively. Figure 2.2 depicts these two conceptions. In contrast to the Néel state the RVB-state exhibits no long range order

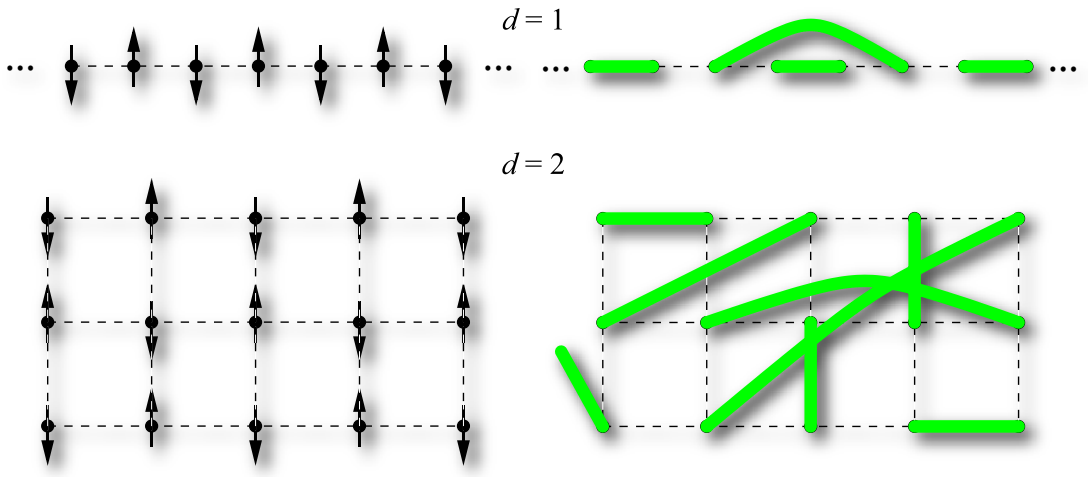

Figure 2.2.: Néel state (left) and RVB-state (right) of an AF-spin-chain ($d = 1$) and a AF square lattice ($d = 2$), from [14].

and no net magnetization, thus representing a *spin-liquid*. A crucial quantity of such systems is the correlation length S_{corr} of the spin-dimers. If S_{corr} is finite the excitation spectrum has an energy gap and the size of the gap is determined by the energy required to break one spin-dimer. However, in the extreme case of $S_{corr} \rightarrow \infty$ even the Néel state can be represented by a suitable RVB-state [17]. Hence, long-range correlations imply a vanishing spin-gap. Whether a quantum-antiferromagnet can be better described by a Néel state or a RVB-state depends, among other quantities, on the dimension or the coordination number, respectively, of the system [14]. Lower coordination number favors the RVB-state, therefore the ground state of a one-dimensional AF-spin-chain has no

long range order. A frustration of the spin-system, which will be introduced below favors a RVB-state, too.

2.2.2. Uniform Chain

If the coupling of the electron spins occurs predominantly in one direction and coupling in the other directions is of negligible weakness, a spin chain is formed. If only nearest-neighbor (NN) interactions are taken into account the spin-Hamiltonian of this *Heisenberg chain* is given by:

$$H = J \sum_i \boldsymbol{S}_i \cdot \boldsymbol{S}_{i+1} \ . \tag{2.8}$$

The Heisenberg chain is of principal importance since the ground state as well as excited states can exactly be determined by the *Bethe-ansatz*[1] [18]. The *groundstate* of the Heisenberg chain is a spin-singlet, i.e. neighboring spins are oriented antiparallel. However, as stated above the system does not possess long range order at finite temperature. According to the theorem of Hohenberg, Mermin and Wagner [19] a long range ordered Néel-state state is precluded in systems with dimension $d = 1$ and $d = 2$ by quantum fluctuations. In the case of the one-dimensional Heisenberg chain, this gives rise to algebraically decaying quasi long range spin-spin correlations. From this ground state the elementary excitations are not, as one would naively expect, $\Delta S^z = \pm 1$ spin-flips. Instead of that the elementary excitations, the *spinons* possess spin $S^z = 1/2$ and can be understood as domain-walls, which is illustrated in Fig. 2.3. The excitation

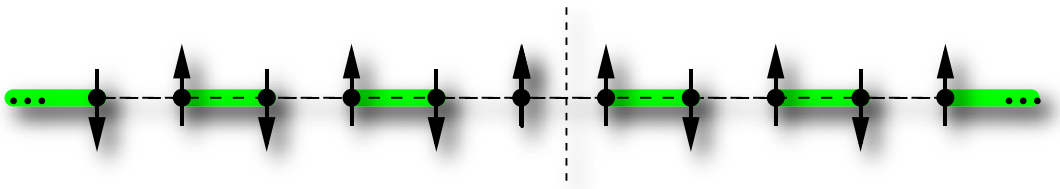

Figure 2.3.: A $S = 1/2$ spinon conceived as a domain wall between ground state patterns. The spin-dimers of a possible RVB-groundstate are represented by green bars. From the RVB-groundstate a lone spin represents a $S = 1/2$ excitation.

spectrum of the uniform Heisenberg chain [20, 21] has the dispersion

$$\omega_l(q) = \frac{\pi}{2} J \mid \sin q \mid \tag{2.9}$$

The spinons can only be excited in pairs. Thus for any total momentum $q = q_1 + q_2$ a continuum of two spinon excitations with energies $\omega(q) = \omega(q_1) + \omega(q_1)$ exists. In

[1] Hans Albrecht Bethe, 2.7.1906-6.3.2005, Nobel laureate 1967

addition to the lower boundary 2.9 with the condition that one of the spinons has zero energy, an upper branch with $q_1 = q_2$ is formed with the dispersion

$$\omega_u(q) = \pi J \mid \sin q/2 \mid \tag{2.10}$$

The excitation spectrum of the uniform AF Heisenberg chain is depicted in Fig. 2.4. The major part of the spectral weight is concentrated at the lower boundary [22]. The

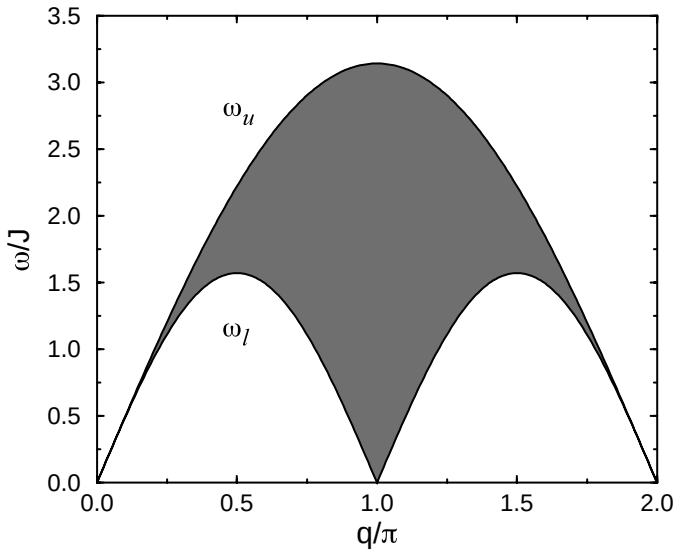

Figure 2.4.: Excitation continuum (shaded area) of the uniform AF Heisenberg chain between lower and upper bound ω_l and ω_u.

excitations of the uniform chain consist at least of two spinons, thus they can be described as combined to one spin $S = 0$ singlet, which is also the groundstate, or three $S = 1$ triplet excitations. At $E = 0$ the excitation spectrum is degenerate. However, this degeneracy can be lifted by additional interactions.

2.2.3. Frustrated Spin Chain

By the term *frustration* a competing interaction in addition to the NN-interaction of 2.2.2 is denoted. This could be a next-nearest-neighbor (NNN) interaction. A Heisenberg chain with frustration from NNN interactions is represented by the Hamiltonian

$$H = J \sum_i (\boldsymbol{S}_i \cdot \boldsymbol{S}_{i+1} + \alpha \boldsymbol{S}_i \cdot \boldsymbol{S}_{i+2}) \tag{2.11}$$

with the frustration parameter $\alpha = J_{nnn}/J_{nn}$, the ratio of the NNN-exchange energy to the NN-exchange energy. From this *Majumdar*-model [23] the uniform chain of 2.8 is obtained by setting $\alpha = 0$. The effect of frustration is illustrated in Fig. 2.5. The system evades the competition between the two competing AF-couplings by breaking the translational symmetry and formation of spin-dimers of neighboring spins which lowers its total energy. The Majumdar model has been studied intensively [23] and is exactly solvable at the *Majumdar-Ghosh*-point $\alpha = 0.5$. Here the system is in a RVB-state, the

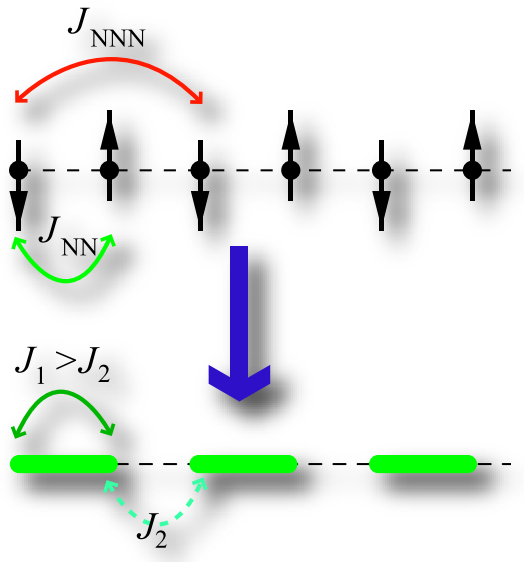

Figure 2.5.: Frustration driven (J_{NNN}) dimerization of an uniform AF-spin-chain. By forming spin-dimers with exchange coupling J_1 the system lowers its energy

spin-spin correlation function is restricted to the dimers and vanishes outside of them. The system thus exhibits an energy gap [24]. If the parameter α is varied between zero and 0.5 the gap in the excitation spectrum opens at the critical value $\alpha_c \approx 0.2411$ [25, 26].

2.2.4. Alternating Spin Chain

The alternating or dimerized spin-chain is another system where the degeneracy of the ground state of the homogenous chain is lifted. In a dimerized chain (see lower part of Fig. 2.5) the NN-coupling constants from a given magnetic center to its neighbors possess different values on either sides. This situation is realized in VPO where the alteration is caused by differences of the chemical bonds between the magnetic ions. Another example of a dimerized system is the spin-Peierls antiferromagnet $CuGeO_3$ at temperatures below the transition temperature. The spin-Peierls transition will briefly be addressed below in the discussion of the spin-phonon coupling. A frustration as it was introduced above induces a dimerization, too, and therefore renders similar properties of the system.

The Hamiltonian of a dimerized (and frustrated) spin-chain is given by

$$H = J \sum_i \left[(1 + (-1)^i \delta) \boldsymbol{S}_i \cdot \boldsymbol{S}_{i+1} + \alpha \boldsymbol{S}_i \cdot \boldsymbol{S}_{i+2} \right] \tag{2.12}$$

with the dimerization parameter $\delta = (J_2 - J_1)/(J_2 + J_1)$ and $0 \leq \delta \leq 1$. A frustration may be present, too, if $\alpha \neq 0$. The uniform limit is given by $\delta = 0$.

The system is not solvable analytically but its major properties can be deduced from approximative calculations. From the extreme case of $\delta = 1$ it is easy to understand that the system possesses an energy gap. Here the chain is fully dimerized with a dimer coupling of $2J$ and with vanishing dimer-dimer interactions. This situation resembles

the problem of the H_2 molecule. This system possesses a singlet ground state and a triplet excited state with energies

$$E = \begin{cases} \frac{1}{4}(2J) & S = 1 \\ -\frac{3}{4}(2J) & S = 0. \end{cases} \tag{2.13}$$

Hence, an excitation from the ground state requires the energy $2J$. In the case of $\delta < 1$ the singlet-triplet gap is reduced and the triplets are no longer independent of the pseudo-momentum $\boldsymbol{q}$, instead they exhibit a dispersion in the $\boldsymbol{q}$-space. The size of the energy gap obeys a scaling law: $\Delta_{\text{trip}} \propto \delta^{2/3}$, see [27] and references therein.

The excitations of the dimerized chain shall now be considered more closely. Depending on the strength of the dimerization this can be done with two different approaches. In the picture of spin-1/2 spinon excitations two spinons of a homogenous chain are asymptotically free since their mutual interaction vanishes with increasing distance. If a dimerization is present, however, one of the dimerization patterns on either side of the spinons is energetically favored, as depicted in Fig. 2.6. The energy of the finite piece of the dimerized chain between the two spinons is lifted compared to the regions outside. In effect this establishes a confining potential between two spinons which depends on the

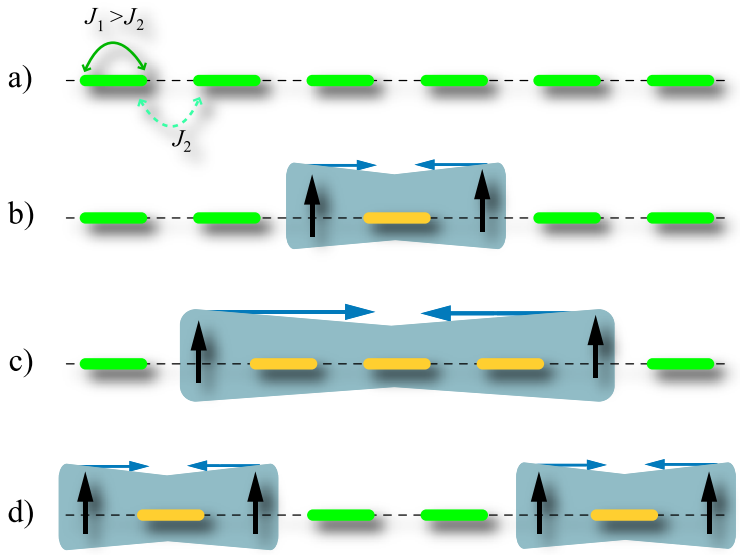

Figure 2.6.: Spinon excitations in a dimerized AF-spin-chain. An excitation from the ground state (a) creates a spinon-pair (b). The energy of the intermediate piece of the chain is lifted proportional to the length of the segment, effectively inducing a confinement potential (b,c). Further increase of the energy of the spinon-pair creates another spinon pair (d).

spinon distance [28, 27]. The gap in the excitation spectrum marks the energy where another spinon pair is created between two spinons instead of breaking up the pair. It

has been noted that the situation here has its analogy in elementary particle physics in the confinement of quark-antiquark-pairs, which cannot be broken because with increased energy new quark-antiquark-pairs will be created [29]. The bound spinons can either form a triplet with spin $S = 1$ or a singlet with $S = 0$. The bound triplets possess a lower energy and thus the excitation spectrum consists of a triplet branch above the $S = 0$ groundstate with minimum energy Δ_{01}, a second singlet branch and the lower boundary of a 4-spinon continuum at $2\Delta_{01}$.

Due to their pairwise interaction, however, the spinons are not the elementary excitations of the dimerized spin chain. The elementary excitations are spin $S = 1$ magnons[2]. Their excitation spectrum can qualitatively be understood by first order perturbation theory [30]. In zero order the elementary excitations are local triplets on the spin dimers, as described on the above. In first order perturbation these triplets can hop from one dimer site to the next with a given probability t_1, therefore obtaining a dispersion along the chain. Simultaneously the triplets exhibit an interaction which depends on their mutual spin orientation. The interaction between two parallel triplets, i.e. a pair of triplets with $S_{tot} = 2$ is strongly repulsive whereas in the case of antiparallel triplets $S_{tot} = 0$ it is attractive, thus establishing a singlet bound state. A third possibility is the weakly bounded intermediate case when $S_{tot} = 0$, the triplet bound state. Figure 2.7 displays the full excitation spectrum. If frustration is included in the Hamiltonian

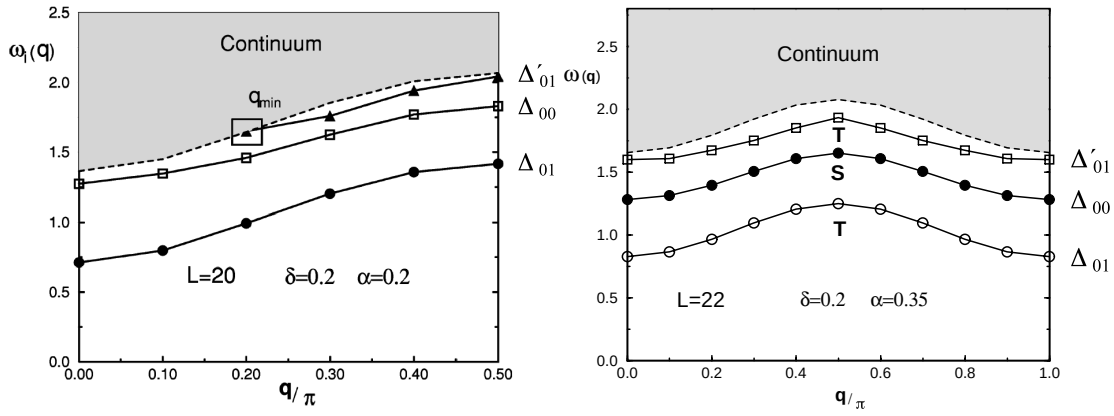

Figure 2.7.: Excitation spectrum of the dimerized spin chain with finite frustration from density matrix renormalization group (DMRG) calculations [31, 32], with frustration $\alpha = 0.2$ (left side) and $\alpha = 0.35$ (right side), respectively. Note the different scale of the momentum $\boldsymbol{q}$. Above the low lying one-triplet branch Δ_{01} two-magnon singlet Δ_{00} and triplet Δ'_{01} bound states are formed. The antibound $S_{tot} = 2$ pair excitation merges with the two-magnon continuum starting at $2\Delta_{01}$. Frustration increases the bounding energy of the bound states such that with larger frustration the triplet bound state Δ'_{01} detaches fully from the two magnon continuum.

[2] these *heavy* magnons, the mass representing their mutual interaction, have to be distinguished from *massless* magnons e.g. in 3D-antiferromagnets, thus in newer literature these quasi-particles are sometimes denoted as *triplons*

2.12 the spectra are altered such that with increasing frustration the binding energy of the bound states rises. Thus it depends on the strength of the dimerization δ and the frustration α whether the triplet bound state merges partly with the two magnon continuum or not (Fig. 2.7).

Crucial for experimental observations, as presented in this work, is the spectral weight of the magnon excitations. This question has recently been addressed by Schmidt *et al.* [33] with continuous unitary transformation (CUT) techniques in high-order perturbation. They calculated Raman lineshapes for several values of the dimerization and frustration, which are reproduced in Fig. 2.8. An important result of their calculation

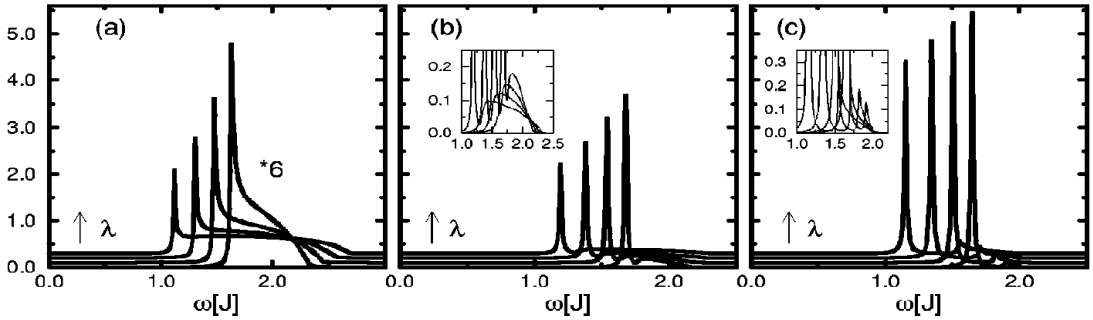

Figure 2.8.: Calculation of the Raman line shape of two-magnon excitations of a dimerized spin-chain, reproduced from [33]. The pictures (a),(b) and (c) refer to frustration $\alpha = 0,\ 0.25,\ 0.5$, respectively. In each picture the curves are shifted accordingly to the chain dimerization.

is that with increased frustration the spectral weight in the Raman spectra is moving from the two-magnon continuum towards the singlet bound state. In chapter 9 I will compare these results with my Raman measurements of VPO.

In summary, the excitation spectrum of a dimerized AF spin-chain exhibits a singlet-triplet gap Δ_{01}, a one-magnon triplet branch and a two-magnon continuum above $2\Delta_{01}$. In addition to the triplet branch a singlet and a triplet bound-state are formed. The relative energy of these excitations depend strongly on the strength of an additional frustrating NNN interaction.

2.3. Spin Ladders

The *spin-ladder* geometry is an interesting variation of spin-chains, and since it had been suggested that VPO was a realization of this model I will occasionally refer to it. In the ladder geometry two (or more) adjacent spin-chains (with coupling $J_{\|}$) are coupled by a rung coupling $J_{\perp}$, see Fig. 2.9. If the coupling along the legs $J_{\|}$ is small compared to $J_{\perp}$, then a two-leg ladder can be described as a system of dimers with a singlet groundstate and a finite singlet-triplet gap [34]. The excitation spectrum of a two-leg spin-ladder is thus closely related with that of a dimerized AF-spin-chain, therefore these systems are experimentally difficult to distinguish by measurements of macroscopic

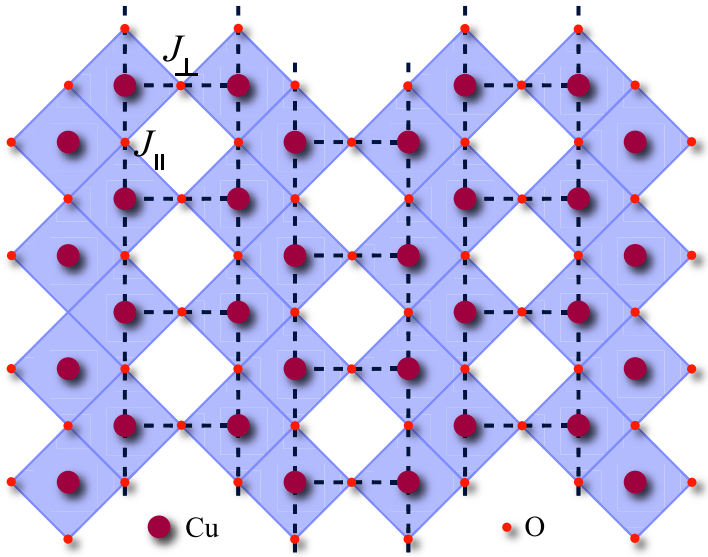

Figure 2.9.: Spin-ladder configuration of the Cu_2O_3 sheets in $SrCu_2O_3$. The dominant AF exchange paths are those where the Cu-O-Cu bonds couple with 180^o angles. The interladder coupling is weak due to the 90^o couplings between next-neighbor Cu-atoms.

properties, as e.g. magnetic susceptibility. In general, whether a N-leg-ladder exhibits a gap or not depends presumably on N being even or odd [35, 36, 37], even N-system possess a gap and odd N-systems not. The ladder geometry is realized e.g. in some modifications of the system $Sr_{n-1}Cu_{n+1}O_{2n}$, $n = (3, 5, 7, \cdots)$, which is a homologous series of high pressure phases where $Cu_{n+1}O_{2n}$ sheets alternate with Sr_{n-1} sheets along the c axes of their orthorhombic cells [38]. The cuprate sheets play an important role in the high-T_c superconductors and the hole-doped compound $Sr_{14-x}Ca_xCu_{24}O_{41}$ becomes superconducting under pressure [39]. In $Sr_{14}Cu_{24}O_{41}$ the cuprate sheets consist of spin chains and spin ladders. $SrCu_2O_3$ and $Sr_2Cu_3O_5$ have two-leg and three-leg geometry, respectively [40]. The two-leg ladder $SrCu_2O_3$ has been studied intensively by Raman scattering, see [41, 42] and references therein.

2.4. Spin-Phonon Coupling

An important aspect of real spin systems is the influence of the lattice dynamics on the spin-spin interaction. Since the strength of the exchange forces depends crucial on bond length and bond angles, any change of the local arrangement of the magnetic ion lattice modulates the exchange interaction and thus allows for a coupling between the phonon and spin dynamics. A renowned effect of coupling between spins and phonons is the spin-Peierls transition of a homogenous spin chain, which is the magnetic analogy of the electronic Peierls instability of a one-dimensional metallic atom chain [43]. A linear coupling between the lattice vibrations and the spin-spin interaction is sufficient to induce a competing interaction into the spin system, a situation comparable to frustration described above. If the coupling strength exceeds a certain critical value the interplay between elastic energy and magnetic energy results in a spontaneous lattice distortion

and the system undergoes a phase transition into a dimerized phase [44] and a singlet-triplet gap Δ_{01} opens. The transition occurs at the critical temperature T_{SP} which is connected to the energy gap as

$$\Delta_{01,T=0} = 1.765 k_B T_{SP}. \tag{2.14}$$

Moreover, the fact that spin-phonon coupling induces a competing interaction to the NN-interaction of neighboring spins can promote the formation of magnetic bound states [45, 46, 47]. The prominent example exhibiting a spin-Peierls transition is CuGeO, which was in fact the first inorganic compound known with this property [48]. The transition temperature for CuGeO is $\approx 14K$.

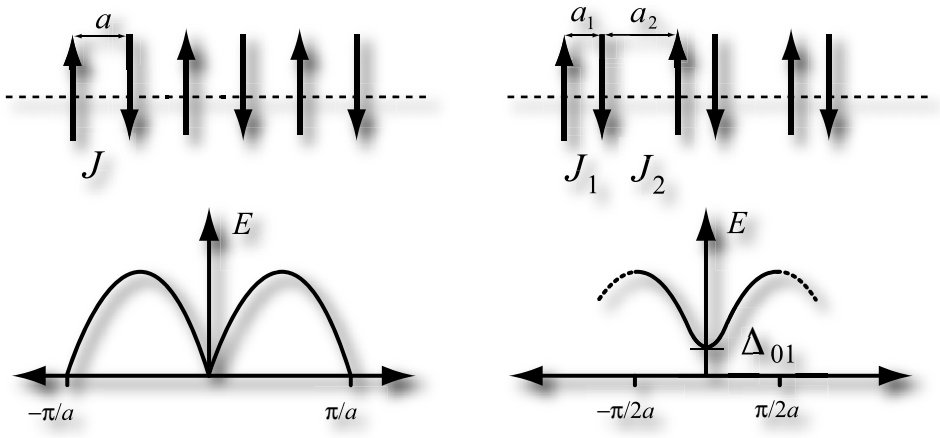

Figure 2.10.: Schematic depiction of the spin-Peierls transition. Note the similarity to frustration driven dimerization of Fig. 2.5. Phonons coupling to the spin system soften and produce a static dimerization of the lattice below the transition temperature T_{SP}. The unit cell is doubled and correspondingly the first Brillouin zone halves associated by the opening of a gap in the excitation spectrum.

On the phonon side spin-phonon coupling induces a magnetic contribution to the phonon self energy in the form of phonon energy renormalization (real part of self-energy) or alteration of the phonon linewidth (imaginary part). A much discussed problem was whether the spin-Peierls transition is always accompanied by a "weak" phonon (see [49, 50, 51] and references therein). It was found that the frequency shift of the phonons involved in the transition depends strongly on the ratio of their energy to the energy of the resulting spin-gap. For phonons with $\omega < \Delta_{01}$ the frequency softens on approach to the transition temperature whereas for phonons with $\omega > \Delta_{01}$ the energy hardens [51].

In the case of an already structurally dimerized spin chain the coupling results in renormalization effects of the phonons involved. For VPO this has been modelled by Uhrig and Normand [46, 52]. They found that phonons interacting with the spin system show a pronounced mode shift and softening, which at low temperatures agrees well with the experiments. Another prediction which has yet to be confirmed is a flattening of the

magnon dispersion at higher temperatures. The spin-phonon coupling effects in VPO

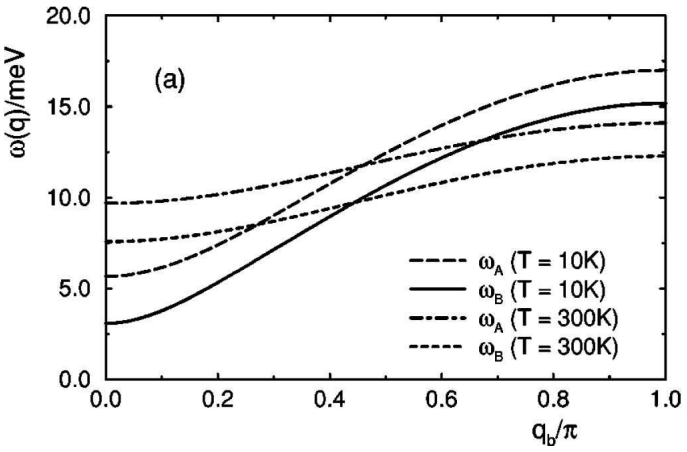

Figure 2.11.: Proposed magnon dispersion flattening of dimerized spin chains in VPO due to spin-phonon coupling, reproduced from [52]

and the Uhrig/Normand-model will be further discussed together with my experimental results in chapter 9.

2.5. Raman Scattering

The experimental method which was mainly used in this work was Raman scattering. I will therefore summarize in this section the basic theory of Raman scattering from lattice vibrations and magnetic excitations. Inelastic light scattering has been predicted as early as 1922 by Brillouin and others and was first observed by C. V. Raman in 1928 [53], after whom this effect is named. The importance of this discovery had been rewarded by the Nobel price in 1930 but it was only with the advent of the Laser that powerful light source became available so that what in the beginning had been a mere physical effect became now an important examination tool indispensable in particular for the study of crystals.

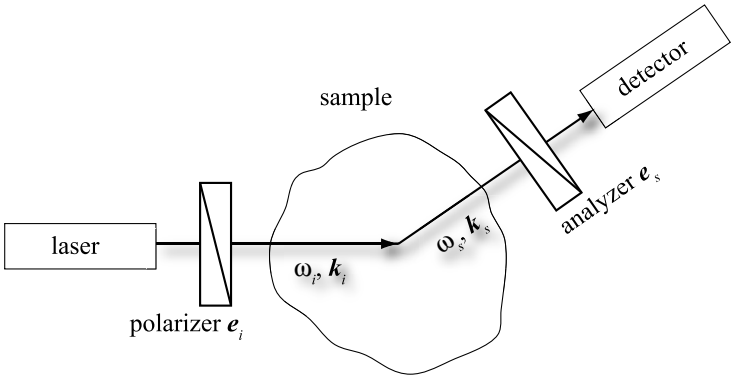

Figure 2.12.: Geometry of a Raman-scattering experiment.

The geometry of a Raman experiment is sketched in Fig. 2.12. Light with energy ω_i and polarization $\boldsymbol{e}_i$ is incident onto the sample volume. In the sample the electromagnetic wave $\boldsymbol{E}_i(\omega_i)$ is propagating along $\boldsymbol{k}_i$, where

$$\mid \boldsymbol{k}_i \mid = \frac{2\pi n_s}{\lambda_i} = \frac{n_s \omega_i}{c}, \tag{2.15}$$

with n_s the refractive index of the scattering medium, λ_s the vacuum wavelength of the wave and c the vacuum speed of light. By the incident wave E_i a polarization field P_s is generated within the sample with

$$P^{\mu}(\boldsymbol{r}, t) = \epsilon_0 \sum_{\nu} \chi^{\mu\nu}(\boldsymbol{r}, t) E_i^{\nu}(\boldsymbol{r}, t). \tag{2.16}$$

Here ϵ_0 denotes the vacuum permittivity and $\chi^{\mu\nu}$ is the susceptibility tensor of the material under investigation. The susceptibility, or dielectric function is the crucial quantity for the light scattering since any vibrational or electronic excitation of the material will modulate $\boldsymbol{\chi}$ and therefore induce fluctuations in the polarization field $\boldsymbol{P}$. The scattered light originating from $\boldsymbol{P}$ spreads in all directions but will usually be detected only in one direction, defined in analogy to the incident wave by the vector

$$\mid \boldsymbol{k}_s \mid = \frac{2\pi n_s}{\lambda_s} = \frac{n_s \omega_s}{c} \tag{2.17}$$

for a given wavelength λ_s. An analyzer selects only scattered light with polarization $\boldsymbol{e}_s$. The geometry of a Raman experiment is usually denoted by the short hand Porto notation as $[\boldsymbol{k}_i(\boldsymbol{e}_i \boldsymbol{e}_s)\boldsymbol{k}_s]$ [54].

The scattering strength of the sample is given by the scattering cross section σ, i.e. the ratio of the flux of scattered particles to the flux density of incident particles. Usually it will be formulated as a differential cross section. By applying the Maxwell equations to 2.16 a differential equation for the scattered field $\boldsymbol{E}_s(\omega_s)$ can be set up:

$$(\nabla^2 + k_s^2)\boldsymbol{E}_s(\boldsymbol{r}, \omega_s) = -\frac{\omega_s^2}{\epsilon_0 c^2} \boldsymbol{P}(\boldsymbol{r}, \omega_s) \tag{2.18}$$

With some manipulation (see. [55]) and with the assumption of a plane incident wave the differential scattering cross section can be obtained from the solution of this equation in the form

$$\frac{d\sigma^2}{d\Omega d\omega_s} = \frac{\omega_i \omega_s^3 n_s V}{16\pi^2 c^4 n_i} \sum_{\alpha,\beta,\mu,\nu} e_i^{\alpha} e_s^{\beta} e_i^{\mu} e_s^{\nu} \langle (\chi_{\boldsymbol{k}}^{\alpha\beta})^* \chi_{\boldsymbol{k}}^{\mu\nu} \rangle_{\omega}, \tag{2.19}$$

with the correlation function

$$\langle (\chi_{\boldsymbol{k}}^{\alpha\beta})^* \chi_{\boldsymbol{k}}^{\mu\nu} \rangle_{\omega} = \int\int e^{i\boldsymbol{k}\cdot(\boldsymbol{r}' - \boldsymbol{r}'')} \langle (\chi^{\alpha\beta}(\boldsymbol{r}', t))^* \chi^{\mu\nu}(\boldsymbol{r}'', t) \rangle d^3(\boldsymbol{r}' - \boldsymbol{r}'') dt \tag{2.20}$$

In this expression the angular brackets denote an average over the fluctuations of $\boldsymbol{\chi}$, V denotes the scattering volume and the wavevector $\boldsymbol{k}$ and the frequency ω are given by

$$\boldsymbol{k} = \boldsymbol{k}_i - \boldsymbol{k}_s \tag{2.21}$$

$$\omega = \omega_i - \omega_s. \tag{2.22}$$

The other symbols are defined as before. These relations state the conservation of momentum and energy in the scattering process. Since $\omega_i \approx \omega_s$, it follows that the cross section is proportional to the fourth power of the excitation energy, thus in practice for the examination of weakly scattering samples it is sometimes desirable to use as short an excitation wavelength as it is allowed by the spectrometer optics. The determining quantity for the cross section is the correlation function $\langle (\chi^{\alpha\beta}_{\boldsymbol{k}})^* \chi^{\mu\nu}_{\boldsymbol{k}} \rangle_\omega$ and therefore the susceptibility $\boldsymbol{\chi}$. From that an effective Raman Hamiltonian representing the interaction between the polarization field $\boldsymbol{P}$ of 2.16 and the scattered electric field $\boldsymbol{E}_s$ can be formulated as

$$\boldsymbol{R}(\boldsymbol{r}) = \sum_{\boldsymbol{r}} \sum_{\alpha,\beta} E_i^\alpha \chi^{\alpha\beta}(\boldsymbol{r}) E_s^\beta \tag{2.23}$$

A standard method for obtaining the cross section is the expansion of $\boldsymbol{\chi}$ in terms of the variables that describe the excitation in question. In the following I will summarize the relevant expression for inelastic light scattering from lattice and spin excitations.

2.5.1. Vibrational Light Scattering

In order to evaluate the correlation function in 2.19 for lattice vibrations a common approach is to expand the susceptibility tensor $\boldsymbol{\chi}$ in terms of phonon normal coordinates Q_i [56]:

$$\boldsymbol{\chi}(Q_i) = \boldsymbol{\chi}_0 + \sum_i \left[\frac{\partial \chi}{\partial Q_i} Q_i e^{-i\omega_i t} + \frac{\partial \chi}{\partial Q_i^*} Q_i^* e^{+i\omega_i t} \right] \tag{2.24}$$

$$+ \sum_i \left[\frac{1}{2} \frac{\partial^2 \chi}{\partial Q_i^2} Q_i^2 e^{-2i\omega_i t} + \frac{1}{2} \frac{\partial^2 \chi}{\partial Q_i^{*2}} Q_i^{*2} e^{+2i\omega_i t} \right] \tag{2.25}$$

$$+ \sum_{i,j} \frac{1}{2} \frac{\partial^2 \chi}{\partial Q_i \partial Q_j^*} \left[Q_i Q_j^* e^{-i(\omega_i - \omega_j)} + Q_i Q_j^* e^{+i(\omega_i - \omega_j)} \right] + ... \tag{2.26}$$

Here ω_i denotes the phonon frequency and $\boldsymbol{\chi}$ the static susceptibility. First order Raman scattering is induced by the first sum with $\omega_s = \omega \pm \omega_i$, where ω denotes the frequency of the incident light. The second sum induces second order scattering with $\omega_s = \omega \pm 2\omega_i$ and the third sum represents combination scattering with $\omega_s = \omega \pm (\omega_i \pm \omega_j)$ if $i \neq j$. If $i = j$ this term represents Rayleigh scattering with $\omega_s = \omega$. If 2.19 is evaluated with the first-order term of 2.24 the scattering cross sections for Stokes and anti-Stokes scattering

are

$$\frac{d\sigma^2}{d\Omega d\omega_s} = \frac{\omega_i \omega_s^3 n_s V}{16\pi^2 c^4 n_i} \left| \boldsymbol{e}_s \cdot \frac{\partial \chi}{\partial Q_i} \cdot \boldsymbol{e}_i \right|^2 \frac{\hbar}{2\omega_i} [n(\omega_i) + 1] \qquad \text{(Stokes)} \tag{2.27}$$

$$\frac{d\sigma^2}{d\Omega d\omega_s} = \frac{\omega_i \omega_s^3 n_s V}{16\pi^2 c^4 n_i} \left| \boldsymbol{e}_s \cdot \frac{\partial \chi}{\partial Q_i^*} \cdot \boldsymbol{e}_i \right|^2 \frac{\hbar}{2\omega_i} [n(\omega_i)] \qquad \text{(anti} - \text{Stokes)}, \tag{2.28}$$

with the Bose-Einstein population factor $n(\omega) = [\exp(\hbar\omega/K_B T) - 1]^{-1}$. The tensor product $|\boldsymbol{e}_s \cdot \partial\chi/\partial Q_i \cdot \boldsymbol{e}_i|$ defines selection rules for the orientation of the polarization of incident and scattered light. They depend on the symmetry of the *Raman tensor* $\boldsymbol{R} = (\partial\chi/\partial Q_i)$ which itself is fully determined by the symmetry of the crystal. The possible Raman tensors for all crystallographic point group have been derived and are tabulated [57, 56]. The Raman selection rules which apply for the symmetry groups of VPO will be discussed in detail in chapter 5.

2.5.2. Magnetic Light Scattering

For magnetic materials the correlation function 2.19 can be evaluated by expanding the susceptibility $\boldsymbol{\chi}$ in terms of spin operators. By following the approach of Moriya [58, 55] $\chi_i^{\alpha\beta}$ can be expressed at lattice site i as

$$\chi_i^{\alpha\beta} = \chi_0^{\alpha\beta} + \sum_{\mu} K_i^{\alpha\beta\mu} S_i^{\mu} + \sum_{\mu,\nu} G_i^{\alpha\beta\mu\nu} S_i^{\mu} S_i^{\nu} \tag{2.29}$$

$$+ \sum_{\delta} \sum_{\mu,\nu} M_{i,\delta}^{\alpha\beta\mu\nu} S_i^{\mu} S_{i+\delta}^{\nu} + \text{ higher order terms.} \tag{2.30}$$

The lowest order term, the static susceptibility corresponds to an elastic scattering contribution to the scattering cross section. The next two terms are linear and quadratic in the spin operators and induce spin excitations at a *single* ionic site i. The complex tensors $\boldsymbol{K}$ and $\boldsymbol{G}$ describe the strength of the coupling of light to the spin system. The following term involves spin operators at two *different* magnetic sites i and $i + \delta$ and thus corresponds to *two-magnon* light scattering. Of experimental importance are the selection rules for magnetic light scattering, which were derived by Fleury and Loudon [59]. They found that the linear one-magnon part of the susceptibility $\boldsymbol{\chi}_K$ is total antisymmetric and thus inelastic light scattering is only possible if the polarizations $\boldsymbol{e}_i$ and $\boldsymbol{e}_s$ are not parallel. However, there is some parallel contribution to the signal from the quadratic term $\boldsymbol{\chi}_G$ which possesses nonzero diagonal elements. In the absence of significant optical absorption the ratio of these contributions can be determined from measurements of the magneto-optic effects. The linear coefficient K is directly proportional to the magnetic circular birefringence strength (Faraday rotation), while the quadratic coefficient G is proportional to the magnetic linear birefringence ([55] and references herein).

2.5.3. Two-Magnon Light Scattering of antiferromagnetic spin chains

In the Raman spectra of antiferromagnets the ratio of the intensities of one-magnon scattering to two-magnon scattering is rather unusual. In most cases the two-magnon contribution is similar or even larger than the one-magnon signal. This suggests a different mechanism for this scattering process which has been described by Loudon and Fleury as *exchange scattering* [59]. In the expanded susceptibility in 2.29 it is represented by the fourth term. The process of exchange scattering shall now be described for the special case of the quasi one-dimensional AF spin chain, as this is the relevant model for the compound examined in this work. Due to the strong anisotropy in those systems Raman scattering from two-magnon excitations can only be observed if the polarizations of the incoming and the scattered light are both *parallel* to the dominant exchange path. If the two-magnon term of 2.29 is inserted in the expression 2.23 the effective Raman Hamiltonian for the alternating spin chain is given by

$$\boldsymbol{R} = \sum_i (1 + \gamma(-1)^i) \boldsymbol{S}_i \boldsymbol{S}_{i+1}. \tag{2.31}$$

In the limit of large dimerization the exchange scattering process can be illustrated by four spins $\boldsymbol{S}_{1\ldots4}$ [60]. The singlet ground state of the chain $|s, s\rangle$ is a product of two singlets $s_{1,2}$ and $s_{3,4}$. In this case the effective Raman Hamiltonian simplifies to $R_{23} = \boldsymbol{S}_2 \boldsymbol{S}_3$ and, with the spin operators S_i^z and $S_i^\pm S_i = S_i^x \pm S_i^y$, we obtain

$$\boldsymbol{R}_{23} = S_2^z S_3^z + \frac{1}{2}(S_2^+ S_3^- + S_2^- S_3^+). \tag{2.32}$$

The exchange light scattering process is then given by

$$\boldsymbol{R}_{23} \, |s_{12} \cdot s_{34}\rangle = (1/4)(- \left|t_{12}^0 \cdot t_{34}^0\right\rangle + \left|t_{12}^1 \cdot t_{34}^{-1}\right\rangle + \left|t_{12}^{-1} \cdot t_{34}^1\right\rangle) \tag{2.33}$$

where $t_{i,i+1}^{0,\pm1}$ denotes the triplet states with the corresponding S^z component. In this process $\Delta S^z = 0$ as required for inelastic light scattering.

3. Experimental setup

3.1. Raman Spectroscopy

The examination of low lying excitations as for example the magnetic excitations in VPO requires the Raman measurements to be made close to the excitation line. Therefore a good suppression of the elastically scattered light and possible stray light has to be achieved. The experiments have been performed with a Dilor XY-800 triple Raman spectrometer and an Ar^+/Kr^+-ion-laser as the excitation source. In the Dilor XY-800 a double foremonochromator is used for the suppression of the laser line and stray light which allows measurements at very low Raman-shifts close to the excitation energy. The final stage of the spectrometer comprises a 1800 lines/mm grating (alternatively 1200 l/mm) to perform the spectral dispersion. The spectra were recorded on a *l*-nitrogen cooled CCD camera (Wright Instruments). For the measurements at low temperatures the sample was mounted in an Oxford *l*-He bath cryostat to allow measurements at temperatures down to 1.6 K. In all experiments backscattering geometry was applied. Raman scattered light was collected and collimated either by a commercial photo objec-

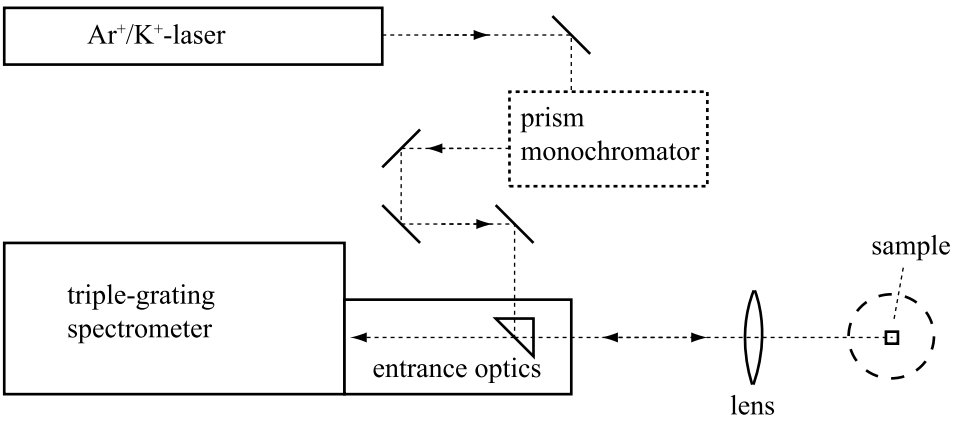

Figure 3.1.: Experimental setup for the Raman measurements. The sample position was alternatively occupied by a He-flow cryostat (Oxford Instruments Optistat), the diamond anvil cell (DAC) or by a He-bath cryostat (Cryovac Kombi) with the DAC mounted therein.

tive with f-number $f/1.7$ or, in the experiments with the cryostats, by a custom made triplet with a f-number of $f/1.8$ and a working distance of 60 mm. A diagram of the experimental setup is depicted in Fig. 3.1.

3.2. High-Pressure Raman Spectroscopy

For the Raman measurements under high hydrostatic pressure a diamond anvil cell (DAC - Syassen/Holzapfel) was used. Its principle is illustrated by Fig. 3.2. The sample volume of the DAC is formed by the central bore ($\approx$ 0.2 mm dia.) of an inconel[1] gasket (thickness $\approx$ 0.3 mm), which is squeezed tight between two opposing faces -the culets- of cone-shaped diamond anvils. The sample volume is filled with a sample chip and a pressure transfer medium in order to achieve hydrostatic pressure. At room temperature

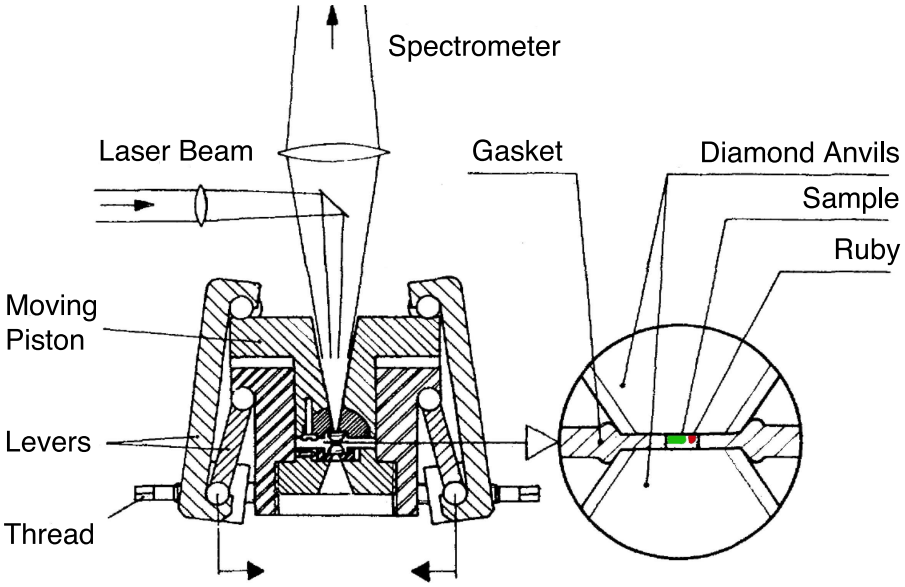

Figure 3.2.: Mechanical design of the Holzapfel-Syassen type DAC with magnified view of the sample volume. The force on the diamonds is generated by turning the threads and transmitted via the knee-levers. This allowed a very compact design of the DAC suitable for application in a cryostat. Mounted into the cryostat the DAC can be operated from outside by extensions of the threads.

a 4:1 methanol/ethanol mixture was used, which still remains a liquid at high pressure. By a thread and lever system the diamonds can be pressed together in order to reduce the sample volume and thus increase hydrostatic pressure. Since the diamond anvil culets have a diameter of only 0.6 mm in principle high pressure up to 10-15 GPa can be obtained easily by moderate external torques on the threads. It was found that after measurements at roughly 10 GPa the sample volume had diminished to a thickness of $\approx$ 0.05 mm and less than $\approx$ 0.1 mm diameter, which therefore limits the size of the samples suitable for investigation in the DAC. Due to the small dimension of the sample volume the charging of the DAC has to be done with observation under a microscope with suitable magnification. After filling in of the alcohol mixture the DAC is closed rapidly to prevent the evaporation of the pressure medium. The orientation of the sample can

[1] Inconel is a very high strength austenitic nickel-chromium-iron alloy

only be determined after the charge procedure by observation of the Raman spectra. If a certain orientation is required, it may take several charges until a proper one is found. It is then still possible that the sample rotates as the pressure is increased so that the orientation is lost. This is a major drawback for the examination of spectral structures which depend strongly on selection rules, as e.g the magnetic excitations in VPO.

The parallel faces of the diamond anvils enable optical access to the sample volume with a f-number of $\approx f/1.6$. Optical access is possible from both sides of the DAC and the positioning of the laser spot on the sample was observed from behind, after attenuation of the laser by several orders of magnitude, by a reading telescope which could be flipped out of the optical axis after use.

The pressure in the DAC was measured by the commonly used ruby luminescence method [61]. A tiny ruby chip was added to the sample volume and its luminescence was observed when the pressure was adjusted. The ruby luminescence lines R1 and R2 around 693 nm show a pronounced pressure induced shift which can be described by an empirical relation between the pressure in GPa and the wavenumber ν [62]:

$$P = 284.4[(\nu_o/\nu)^{7.665} - 1]$$

Independently from a pressure induced shift the ruby luminescence varies with temperature, too. This had to be taken into account in the measurements at low temperature and a control of the temperature of the DAC was then required. For the temperature dependence of the ruby luminescence the Viña-equation can be applied:

$$\nu(T) = \nu_{o(T=0)} - \frac{\alpha}{exp(\Theta/T) - 1}$$

Viña *et al.* developed this equation to describe the temperature dependence of the bandgap of semiconductors [63].
Table 3.1 summarizes the parameters which were used for the calibration of pressure measurements by the ruby luminescence.

Table 3.1.: Calibration parameters for the ruby R1 and R2 luminescence lines.

	ν_0[cm^{-1}]	α[cm^{-1}]	Θ[cm^{-1}]
R1	14421.8	76.6	482
R1	14450.8	72.4	478

For the Raman measurements under pressure and at low temperatures the whole DAC was placed in a liquid helium bath cryostat (CRYOVAC Kombi). Instead of the alcohol mixture, which would solidify at lower temperatures and thus induce uniaxial strain, liquid helium from the bath itself served as the pressure medium. Therefore after charging of the DAC with the sample, it was placed into the cryostat and cooled down until the helium was in the superfluid state. It would then automatically fill the DAC provided it had not been completely closed before. From the phase diagram of helium

in Fig. 3.3 it follows that after closing the DAC and applying pressure at temperatures around 2 K, the helium will immediately crystallize so that additional pressure would induce uniaxial strain on the sample. Therefore adjustment of the pressure always required heating of the DAC up to a temperature where the phase diagram predicts liquid helium and then again cooling down the DAC to the wanted temperature. The crystallization of the helium alters the pressure according to the equation of state but does not induce uniaxial strain.

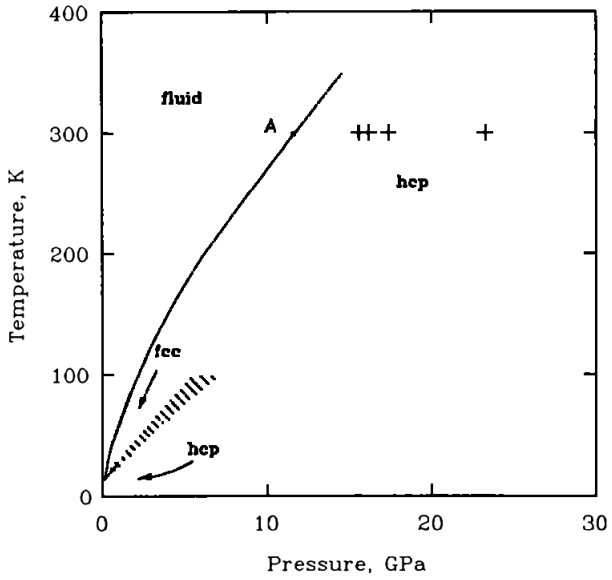

Figure 3.3.: Phase diagram of Helium-4 (reproduced from [64]). The solid line marks the boundary between the solid and the liquid state. The abbreviations denote different crystal structures in the solid phase.

3.3. Infrared Spectroscopy

The infrared spectra have been obtained with a Bruker IVS-66v vacuum Fourier spectroscope. Fourier transform infrared spectroscopy (FTIR) has in recent years advanced to the state-of-the-art method use for infrared spectroscopy. Instead of using a a dispersive element (grating, prism) for the spectral analysis a Fourier spectrometer is essentially a Michelson interferometer, which can be illuminated by different infrared sources. In one of the interferometer arms the sample is placed, either as a transparent sample for transmission measurements, or, with additional optics, as a reflecting sample surface for the measurement of the sample's reflectivity. By shifting one of the interferometer mirrors along the corresponding arm with a constant speed the signal on the detector at the interferometer output becomes time-dependent with a fundamental frequency depending of the mirror speed, usually in the range of 10^3 Hz. This signal, the interferogram, is modulated by the sample and the device characteristics. The detector output is digitized and by a numerical Fourier transformation a power spectrum of the signal is calculated. The computing power required for this step, a major obstacle one or two decades ago, is nowadays provided by any personal computer. One of the advantages of this technique compared to dispersive spectroscopy is the large throughput of the signal due to the fact

that no slits have to be employed in the beam which thus enables rapid measurements. Another advantage is the high resolution in principle achievable which is only limited by the practicable amount of optical path difference in the interferometer arms.

During measurements the whole optics are evacuated to suppress atmospheric absorption. For the far-infrared region below 700 cm^{-1}a sensitive liquid He cooled Si bolometer was used as detector, in the mid-ir a mercury-cadmium-tellurid (MCT) detector cooled with liquid nitrogen was applied. The VPO samples under investigation had well oriented sample surfaces (see 4) with sizes large enough to obtain good reflectivity spectra which could in the case of the HP-VPO sample easily be polished. It was not possible to perform transmission measurements since that would have required extremely thin samples which could not be obtained without the destruction of the whole samples. The sample reflectivity, however, is a function of the complex refraction index so that in order to obtain the phonon frequencies the absorbance of the sample had to be calculated by a Kramer-Kronig-Transformation (KKT). Since the KKT requires in principle the measurement of the reflectivity over an infinite frequency range, the numerical calculation is inherently not exact so that the phonon frequencies found by IR-spectroscopy are supposed to have larger errors than those measured by Raman scattering. They may in cases of weak lines in close vicinity of strong ones be as large as $\pm$ 2-3 cm^{-1}. The reflectivity was measured in the range between 100 and 2000 cm^{-1} but due to increased noise at low wavenumbers only the part above $\approx$ 500 cm^{-1} was useful for the evaluation of phonon frequencies. All spectra have been obtained at room temperature and the measurements were performed with polarizations along each of the crystal axes by the use of wire-grid polarizers for the infrared spectral range.

4. Structure and properties of $(VO)_2P_2O_7$

In this chapter I will discuss the structure of $(VO)_2P_2O_7$, from here on abbreviated by VPO, along with a summary of its properties relevant for the work presented here. Since from the discovery of its magnetic properties in 1987 on different models of the exchange interactions in VPO had been discussed, I will briefly summarize the major steps in the understanding of this compound. Azuma *et al.* [65] discovered in 1999 that VPO undergoes a structural phase transition under high-pressure, high-temperature conditions, and since then this novel phase, high-pressure-(HP)-VPO was examined intensively in comparison with the ambient-pressure-(AP)-phase. Hence, the following discussion will be split into two parts in the beginning for the presentation of the two crystal phases. A summary of the main differences will then follow.

4.1. Ambient-Pressure (AP) phase

4.1.1. Structure

Due to its important industrial impact, as mentioned in the introduction, a large amount of literature exists on the large scale production of AP-VPO (for a review see [66]). In its commercial available form VPO is a powder of nanocrystallites, for which the catalytic efficiency increases if the crystallites become smaller. This of course precludes investigation on this material with methods which require large single crystals,- such as Raman scattering. We obtained high quality single crystals from A.V. Prokofiev (University Frankfurt/M), who advanced the production of large single crystals by a combination of the Czochralsky and the Kyropoulos crystal growth techniques with sensible control of the oxygen content during crystal growth [67],- a crucial condition for obtaining crystals with a low defect concentration. AP-VPO crystallizes in the acentric orthorhombic $Pca2_1$ space group. This was first determined by Gorbunova *et al.* [68] in 1979. However, this refinement of the crystal structure revealed relatively large errors and hence other authors repeated the structure determination. In his study of the crystal structure Nguyen (1995) [69] concluded the lower $P2_1$ space group symmetry. Again, the refinement was not completely satisfying. Hiroi *et al.* (1999) examined powder samples of VPO and found a $Pca2_1$ space group, in accordance with Gorbunova *et al.*. Finally, a recent careful study of Geupel *et al.* [70] at l-N_2 temperature confirmed the findings of Gorbunova in 1979. The crystals examined for this work had been from the same batch than those for which Geupel determined their crystal structure.
Meanwhile it has been established (see above) that during the crystal growth the oxygen partial pressure has to be biased precisely, and crystal studies which came to other results than Gorbunova in 1979 used probably crystals with a somehow higher defect

concentration. In appendix A.1 a comparison of the different symmetries and the assignment of the crystallographic axis to directions in relation to the structure is given.
The unit cell of VPO comprises z=8 formula units. VPO (Figures 4.1 and 4.2) is com-

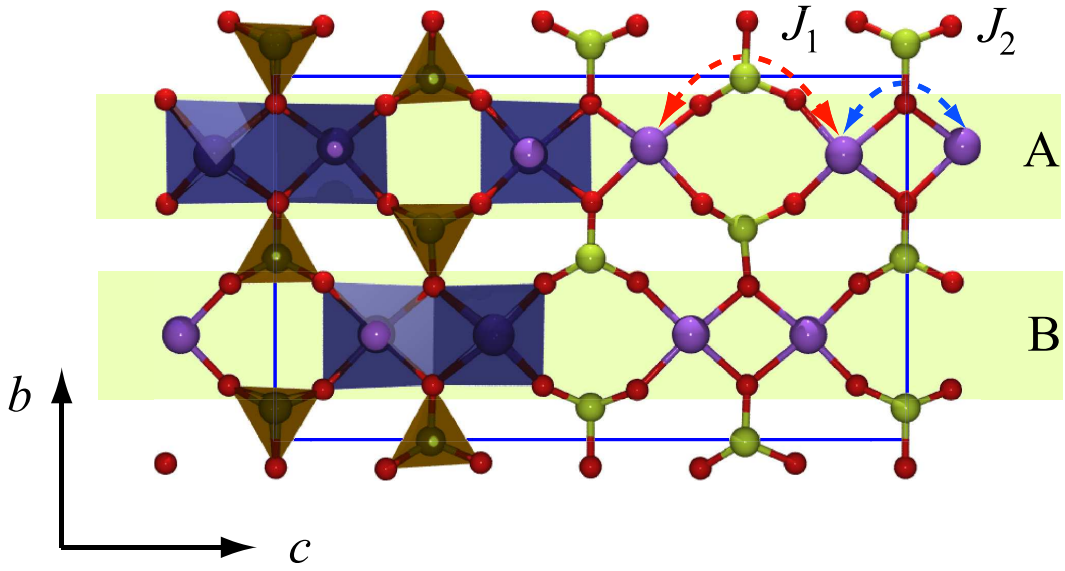

Figure 4.1.: Structure of AP-VPO, view of the b-c plane. The unit cell is framed in blue. One of the exchange paths (J_2) is formed between two neighboring VO_5 pyramids via the common oxygen atoms. The dominant exchange path (J_1) is formed, however, by a coupling through the PO_3 tetrahedron. The chains **A** and **B** are crystallographically not equivalent and have thus different magnetic coupling constants.

posed of vanadyl $(V{=}O)^{2+}$ cations and pyrophosphate $(P_2O_7)^{2-}$ groups. The vanadyl group, a doubly bonded V=O pair where the oxygen atom accepts two electrons from the V atom and thus possesses strong ionic character, is a characteristic feature of most vanadium oxide compounds. Together with six terminal oxygen atoms of the pyrophosphate group two edge sharing coordination pyramids are formed around the vanadium atoms which occupy sites almost in the basal planes. As a result of this coordination V is in the oxidation state 4+ and thus possesses an unpaired electron with spin-$\frac{1}{2}$ which is responsible for the magnetic properties of VPO. The pairs of VO_5 pyramids are in the b-c-plane arranged to layers which in a-direction are linked by the $(P_2O_7)^{2-}$ groups. Adjacent pairs of VO_5 pyramids form chains in the direction of the b-axis. Due to the symmetry of the crystal a unit cell comprises two inequal chain systems **A** and **B** formed by the vanadium atoms V_1-V_4 and V_5-V_8, respectively. This feature turned out to be essential for the explanation of the magnetic properties of VPO.
A different conception of the vanadium coordination led to the discovery of the magnetic properties of VPO. In this picture the vanadium atoms are octahedrally coordinated by 6 oxygen atoms. The V atoms in two edge sharing coordination octahedra form spin dimers in the b-c-plane which represent the rungs of infinite spin ladders formed by cor-

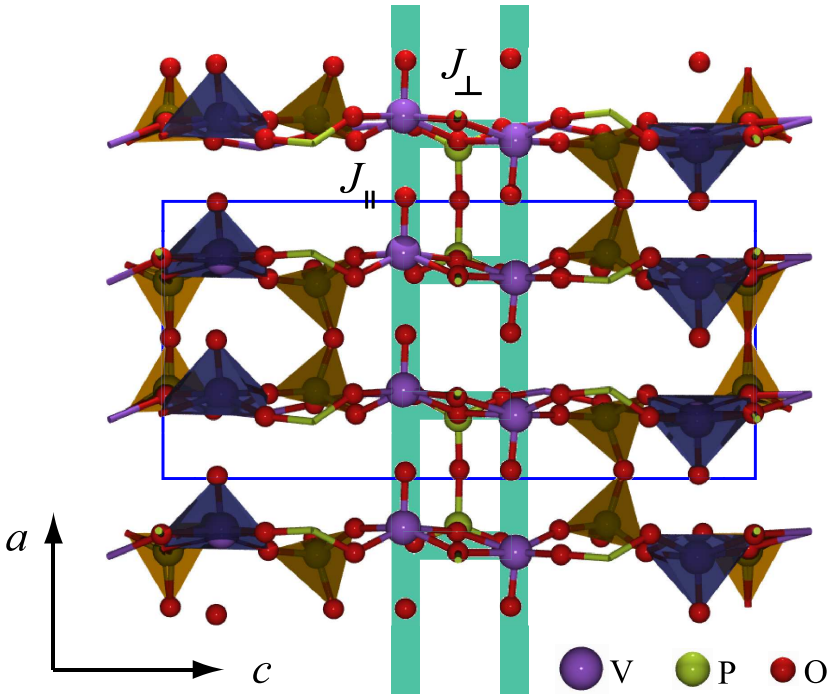

Figure 4.2.: Structure of AP-VPO, view of the a-c plane. In the conception of VPO as a spin ladder compound the legs of the hypothetical ladder structure ($J_\parallel$) run along the V=O vanadyl bonds, the rung coupling $J_\perp$ is identical with the weak coupling J_2 of the spin-chain model.

ner sharing octahedra running along the a-axis, as shown in Fig. 4.2.

4.1.2. Magnetic properties

In a systematic quest for compounds revealing quantum Heisenberg spin-systems Johnston *et al.* examined VPO in 1987 [1] and measured the magnetic susceptibility as a function of temperature. They were led by the conception of the crystal structure as described on the above. A previous study of the precursor material $VO(HPO_4) \cdot \frac{1}{2}H_2O$ (see references 16, 17 in [1]) had shown that the magnetic properties of the precursor were those of isolated V^{4+}-V^{4+}-dimers (α=0) hence they expected for VPO a coupling of the dimers to a spin-ladder structure. Since at that time there had been no theoretical predictions for spin-ladders they fitted their experimental $\chi(T)$ by the model of Bonner *et al.* [71] for an spin-$\frac{1}{2}$ alternating antiferromagnetic spin chain and found a good correspondence between model and experiment for α=0.7. This was surprising because the magnetic properties of spin ladders were expected to differ from that of alternating spin chains with $\alpha \rightarrow 1$ (see ref.[71] and references herein).
The discovery that the magnetic properties of VPO were probably that of an alternating

spin chain or even a spin ladder system triggered subsequent examinations, (since both systems reveal gaps in their excitation spectra). In particular the possibility of VPO being a spin-ladder compound arose interest because for this systems the excitation gap should be present only in even-leg ladder compounds, which VPO seemingly was. In the

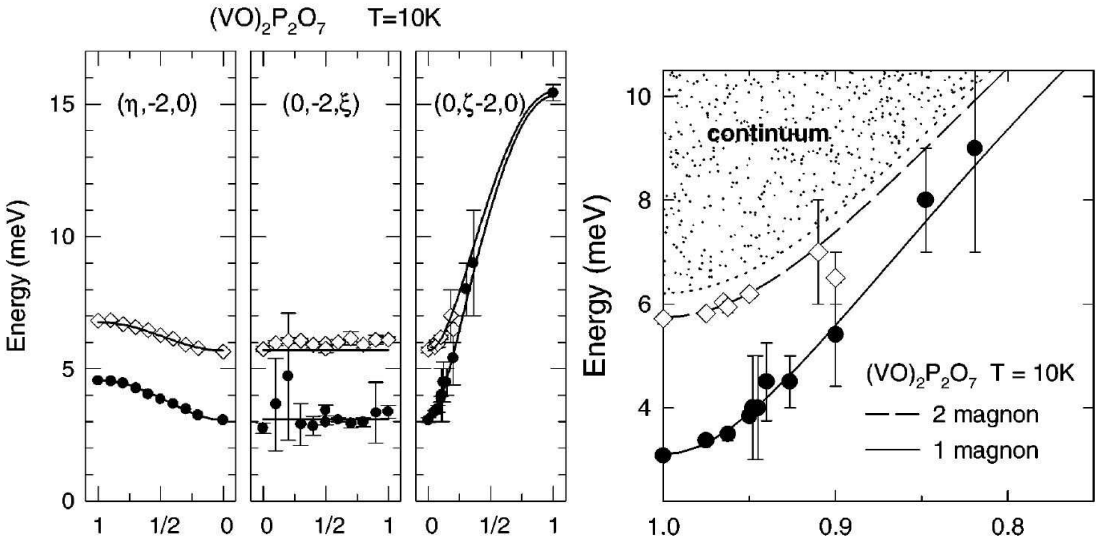

Figure 4.3.: (left) Magnon dispersion of VPO measured by INS, reproduced from [72]. Two branches were observed with an energy ratio of ≈2:1 (lower bound). The strong dispersion along the *c*-axis (the ζ-axis in the graph) indicates the strongest exchange interaction. Weak interaction was found along the proposed ladder direction (ξ). (right) Magnified view of the *c*-axis dispersion with a hypothesized two-magnon continuum.

study of Eccleston *et al.* (pulsed inelastic neutron scattering [73]) a spin-gap of 3.7 meV was measured and interpreted as a confirmation of the spin ladder model. In a later neutron scattering experiment performed by Garret *et al.* [72] a second spin excitation near 6 meV was discovered which is inconsistent with a simple spin ladder model. Hence the same authors undertook a study of the spin dynamics in VPO single crystals [74]. It is noteworthy that to achieve sufficient sample volume for neutron scattering ≈ 200 small single crystals had to be aligned and arranged into an array. Their results showed clearly that the dominant exchange interaction is along the crystallographic *b*-axis whereas in ladder direction a weak ferromagnetic coupling was observed. The second mode was suggested to be a two-magnon bound state, which had been predicted by Uhrig *et al.* in a theoretical work on the excitations of an alternating $S = \frac{1}{2}$ Heisenberg chain [75].

An inelastic neutron scattering study on $VO(DPO_4) \cdot \frac{1}{2}D_2O$, which is the deuterated counterpart of the VPO precursor $VO(HPO_4) \cdot \frac{1}{2}H_2O$ revealed the superexchange pathways in this spin dimer compound. They authors found that the dominant superexchange pathway involves the covalently bonded PO_4-group, – a surprising result because it means that the spin dimers are build up by V atoms 4.43 Å apart instead of the next neighbor V-V distance of 3.09 Å (Fig.4.4). Since the coordination of the V atoms in VPO is essentially the same they concluded similar exchange pathways here which un-

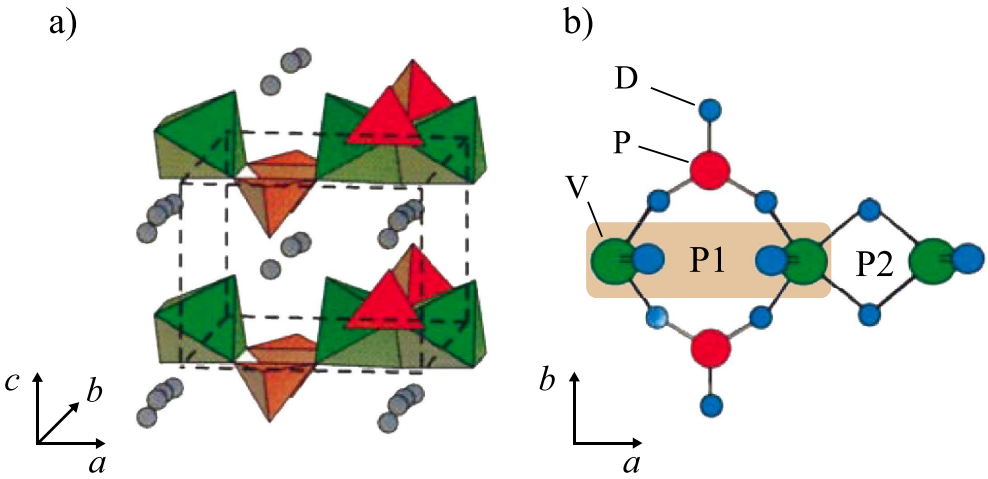

Figure 4.4.: Spin dimers in VODPO, reproduced from [76]. a) Structure. b) Possible superexchange pathways between V^{4+} ions. An unusual strong exchange interaction was found along the path V-O-P-O-V (P1) which is thus forming a spin dimer.

derpinned doubts of VPO actually being a spin ladder. Instead it confirmed the model of an alternating antiferromagnetic spin chain.

Further theoretical and experimental work focused on the possible two-magnon bound state at 6 meV. Kikuchi *et al.* [77] examined VPO by nuclear magnetic resonance (NMR) of the ^{31}P and ^{51}V nuclei and on basis of their results proposed an alternative explanation of the second mode. They suggested a model of two independent spin-chain systems with each possessing its own spin gap, due to the crystallographic inequality of both chains. An extension of this work was given by Yamauchi *et al.* [78], who employed high-field magnetization measurements. Their results gave evidence for two spin gaps at 33 and 62 K, or 2.8 and 5.3 meV, respectively.

4.2. High-Pressure (HP) phase

Azuma *et al.* demonstrated in 1999 that AP-VPO could be transformed into a simplified structure by annealing to 700 °C under a pressure of 2 GPa [65]. The resulting structure with the centric space group symmetry Pnab (standard setting Pbcn) has only one crystallographic vanadium site and hence contains only one kind of spin-chain (Fig.4.5). The structures of AP-VPO and HP-VPO are very similar and Hiroi *et al.* [79] suggested that the high-pressure phase could already exist as a defect phase in AP-VPO, thus explaining the elevated defect concentration usually found in AP-VPO crystals. For the bridging oxygen of the P_2O_7-group large thermal parameters were found, their mobility seems to play an important role in the phase transition. By high-field magnetization, susceptibility and specific heat measurements Azuma *et al.* could prove the presence of a single singlet-triplet-gap in HP-VPO with energy $2\Delta_{01}/k_B \approx 25$ K. The existence of only one gap in HP-VPO was considered as an indirect proof for the model of two

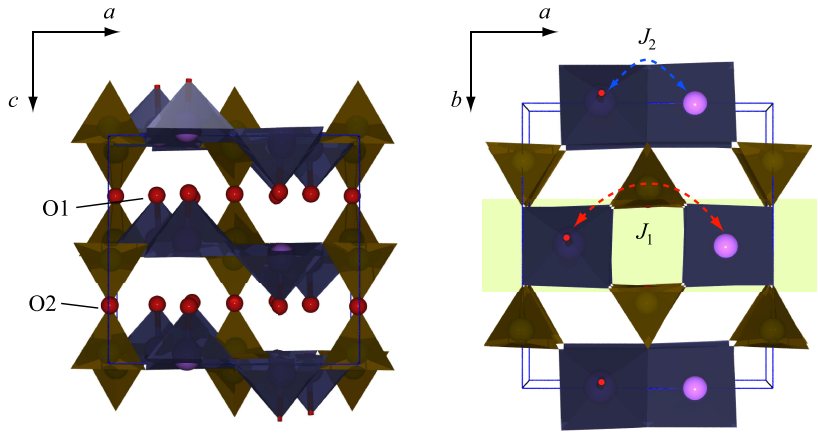

Figure 4.5.: Structure of HP-VPO, shown in Pbcn standard setting. No oxygen atoms are displayed apart from the vanadyl O1 atom and the bridging O2 atom of the P_2O_7 group. The superexchange pathways are assumed to be the same as in AP-VPO.

independent spin chains in AP-VPO. In a study of Narumi *et al.* [80] both compounds were compared by high-field magnetization measurements, their results are shown in Fig. 4.6. Again, the appearance of two critical field strengths in AP-VPO indicates the existence of two independent spin-system here whereas the higher symmetrical HP-VPO consequently reveals only one such value.

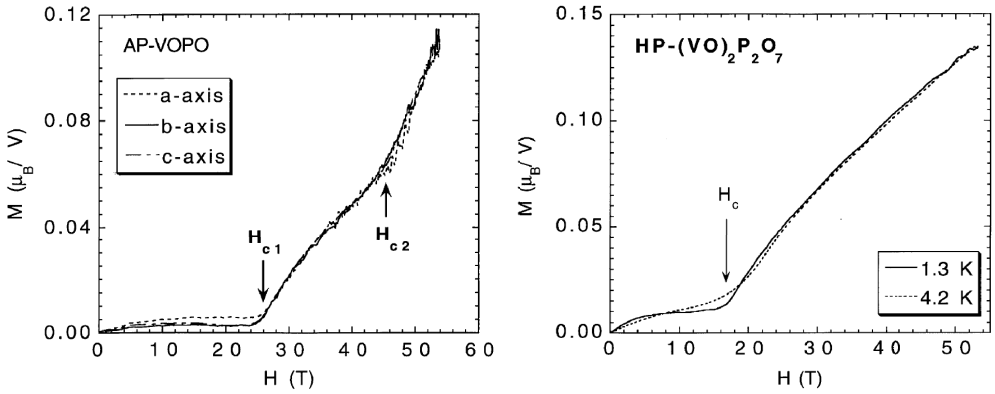

Figure 4.6.: High-field magnetization of AP-VPO (left) and HP-VPO (right), reproduced from [80]. The critical field H_{c1} and H_{c2} for AP-VPO correspond to singlet-triplet-gap energies Δ_{01}/k_B of 33.6 K and 60.6 K, respectively. For HP-APV the critical field equals Δ_{01}/k_B=22.0 K.

Compared with the AP-phase there is only few literature on the magnetic properties of HP-VPO. A study with inelastic neutron scattering on HP-VPO, as it has been performed with AP-VPO [74] would be highly desirable to elucidate about the magnon dispersion, but is unlikely to happen.

5. Normal Mode Analysis

It is an elementary proposition of many particle mechanics that a system comprising of n particles will have $3n$ degrees of freedom. Hence in the case of the unit cell of AP-VPO with 104 atoms it follows that the phonon system consists of 309 vibrational modes, or 309 optical branches in the phonon dispersion, leaving out in this number the acoustic vibrations, i.e. motions of the whole unit cell. To gain further insight into the quality of the vibrational modes I analyzed VPO by applying standard factor group analysis (FGA) to the crystal structure, making use of the tables provided by Rousseau *et al.* in [81]. The number of Raman or infrared active phonons of a particular space group symmetry is given by the irreducible representation of the space group. However, more than that FGA enables us to classify the vibrational modes into motions of certain atoms or molecular groups in the crystal, whether they are internal or external, i.e. uniform motions of whole groups of atoms, which will exhibit very low frequencies due to the large mass involved. In the case of molecular groups FGA allows to correlate the lattice modes to the modes in the isolated molecular groups and thus provides additional information helpful for the assigning of observed spectral features to vibrational modes. As in the preceding chapter, the discussion will be split in separate parts for AP-VPO and HP-VPO, respectively.

5.1. AP-VPO

As described in the chapter on the crystal structure, VPO may be regarded as composed of vanadyl groups V=O and pyrophosphate groups P_2O_7, so the FGA has been performed in respect to these components of the unit cell. The results of the FGA are summarized in table 5.1. The structure VPO has the irreducible representation (without acoustic modes):

$$\Gamma_{\mathrm{AP-VPO}} = 77A_1 + 78A_2 + 77B_1 + 77B_2 \tag{5.1}$$

Since the space group is noncentrosymmetric these modes are Raman active as well as infrared active. If we exclude all external modes, they are supposed to exhibit the lowest frequencies, VPO will possess $46A_1 + 46A_2 + 46B_1 + 46B_2$ Raman-active vibrations with selection rules xx, yy, zz (A_1) and xy (A_2), xz (B_1), yz (B_2) and $46A_1 + 46B_1 + 46B_2$ infrared-active vibrations with polarizations z, x, y, respectively. Table 5.1 predicts four internal vanadyl dimer vibrations in every representation. The only internal degree of freedom of the vanadyl group is a stretching vibration of the dimer axis, and since there are four nonequivalent vanadium sites in the unit cell this mode is split into four by the crystal field. We know from the structure determinations that the crystallographic differences are small so that this mode will most likely appear as a quadruplet in the

Table 5.1.: Summary of the factor group analysis of AP-VPO. R, T, r and i.r. denote rotations, translations, Raman active modes and IR active modes, respectively. Internal, external, optical and acoustic modes are abbreviated by in.m., ex.m., o.m. and a.m, respectively

Factor group C_{2v}	8 P_2O_7 (C_1) in.m.	ex.m.	16 VO (C_1) in.m.	ex.m.	V_{1-4} C_1	P_{1-4} C_1	O_{1-18} C_1	o.m.	a.m.
A_1 r, i.r.	42	6T, 6R	4	12T, 8R	12	12	54	77	1
A_2 r	42	6T, 6R	4	12T, 8R	12	12	54	78	0
B_1 r, i.r.	42	6T, 6R	4	12T, 8R	12	12	54	77	1
B_2 r, i.r.	42	6T, 6R	4	12T, 8R	12	12	54	77	1
312	168	24T, 24R	16	48T, 32R	48	48	216	309	3

Table 5.2.: Correlation scheme for the internal modes of $P_2O_7^{4-}$ in AP-VPO

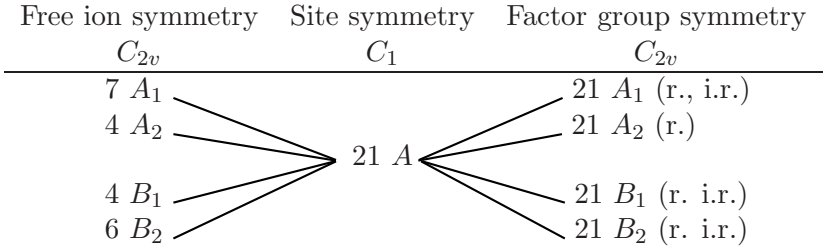

spectra. The vibrations of the pyrophosphate group are not that easy to predict. Table 5.2 below shows the correlation of the modes of an isolated pyrophosphate molecule to the pyrophosphate groups in the lattice. To make the correlation table more significant I assumed a C_{2v} point group for the isolated pyrophosphate, that is the symmetry in which pyrophosphate will usually be described in inorganic chemistry. Actually the pyrophosphate groups *in* the crystal are distorted from that symmetry to the lowest C_1 symmetry. However, the correlation diagram emphasizes that in either case due to the low *site* symmetry C_1 all molecular modes are spread uniformly over all representations of the factor group. Nevertheless we can infer from this correlation diagram that any particular mode of the isolated molecule will appear in each crystal representation as frequently as it appears in the isolated molecule. In order to facilitate the discussion of the spectra below and to provide the notation, the 21 vibrational modes of the free molecule are depicted in table A.4 in the appendix A.4.

5.2. HP-VPO

The analysis of the lattice vibrations of HP-VPO follows the scheme used above for the AP-phase and the results can be adapted. The centrosymmetric space group $Pnab$ instead of the acentric $Pca2_1$ group causes a considerable simplification of the spectra. In addition to the halving of the number of atoms, i.e. the number of vibrational modes, the Raman (g-modes) and i.r (u-modes) vibrations are mutually exclusive and therefore we should observe about one quarter of the lines of AP-VPO in the HP-phase. This is reflected in the irreducible representation, given (without acoustic modes) as

$$\Gamma_{\mathrm{HP-VOPO}} = 19A_g + 19A_u + 20B_{1g} + 19B_{1u} + 19B_{2g} + 18B_{2u} + 20B_{3g} + 19B_{3u}. \quad (5.2)$$

The FGA is summarized in table 5.3. The analysis demonstrates that due to the higher symmetry all modes show degeneracy compared to the AP-phase. The vanadyl vibrations e.g. should degenerate to one line in the spectra.

Table 5.3.: Summary of the factor group analysis of HP-VPO. The abbreviations are explained in table 5.1

Factor	4 P_2O_7 (C_2)		8 VO (C_1)							
group	int.	ext.	int.	ext.	V	P	$O_{1,3-5}$	O_2	opt.	aco.
D_{2h}	mode	mode	mode	mode	C_1	C_1	C_1	C_2	mode	mode
A_g r.	11	1T, 1R	1	3T, 2R	3	3	12	1	19	
A_u s.	10	1T, 1R	1	3T, 2R	3	3	12	1	19	
B_{1g} r.	11	2T, 2R	1	3T, 2R	3	3	12	2	20	
B_{1u} i.r.(z)	10	2T, 2R	1	3T, 2R	3	3	12	2	19	1
B_{2g} r	11	1T, 1R	1	3T, 2R	3	3	12	1	19	
B_{2u} i.r.(y)	10	1T, 1R	1	3T, 2R	3	3	12	1	18	1
B_{3g} r	11	2T, 2R	1	3T, 2R	3	3	12	2	20	
B_{3u} i.r.(x)	10	2T, 2R	1	3T, 2R	3	3	12	2	19	1
156	84	12T, 12R	8	48T, 32R	24	24	96	12	153	3

Building the correlation table of the pyrophosphate molecule to the crystal lattice (table 5.4) gives more information as in the case of AP-VPO, since in HP-VPO the pyrophosphate groups are undistorted and have indeed symmetry C_{2v}. However, more important is the site symmetry C_2, and this results in additional selection rules for the modes. The modes originating from A_1 or A_2 modes of the molecule are found only in $A_{g,u}$ or $B_{2g,u}$ symmetries in the crystal, and similarly those modes which originate from B_1 or B_2 modes of the molecule are found only in $B_{1g,u}$ or $B_{3g,u}$ symmetries.

Table 5.4.: Correlation scheme for the internal modes of $P_2O_7^{4-}$ in HP-VPO

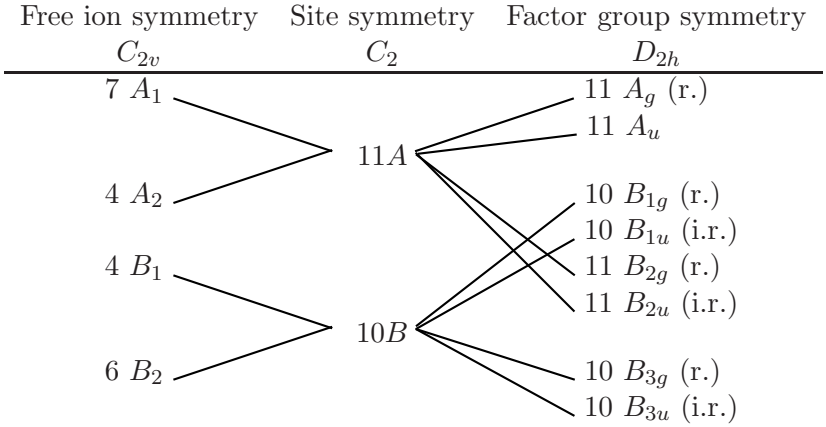

6. Overview of the Experiments

In the preceding chapters I compiled most of the previous knowledge about VPO relevant for this work. Before I start to present the results of my examinations in detail I will, in order to facilitate the discussion in the following chapters, give in this intermediate chapter a brief overview over the experiments I have performed and the results they have yield. Therefore some exemplary findings will be presented here without any further discussion, for which I refer to later chapters.

The findings can be roughly assigned to different spectral regions in the phonon spectra of VPO. Hence I will put ahead in Fig. 6.1 Raman spectra of AP-VPO and HP-VPO. The spectra consist of three discernible regions and most of the following discussion

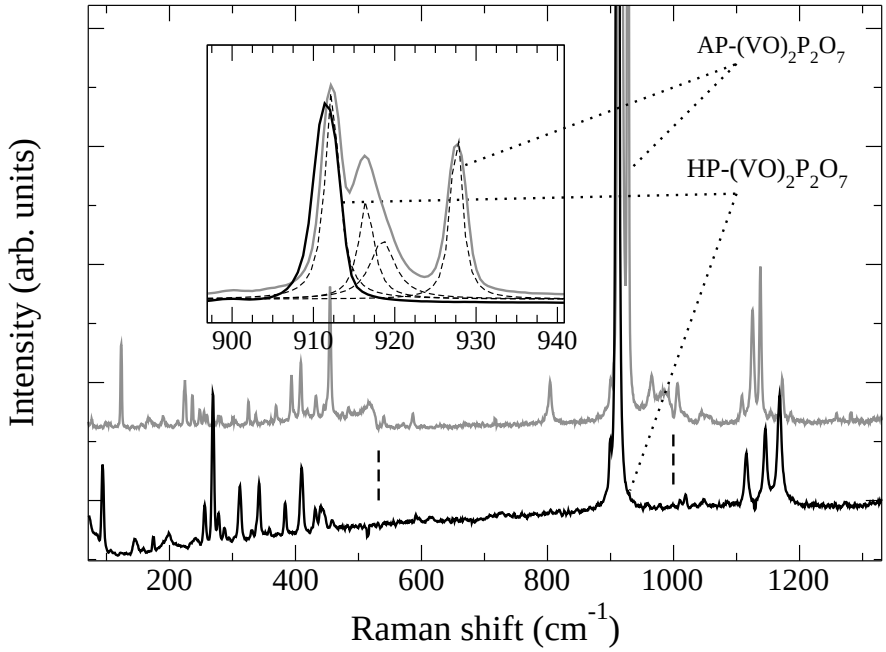

Figure 6.1.: Raman spectra of AP-VPO and HP-VOPO. Shown in the inset is a magnified view of the region of the VO vibrations.

will be organized along this distinction. The modes in the high energy region above ≈ 1000 cm^{-1} will be discussed in chapter 7.1.2 and will be assigned to vibrations of the P_2O_7-groups. Below them some prominent peaks appear around 915 cm^{-1} in the Raman spectra of AP-VPO, which apparently degenerate to one peak in the spectra of the HP-phase. This will be examined in 7.1.1 and the modes will be assigned to vibrations of

the vanadyl V=O group. The peaks lying below ≈ 600 cm^{-1} cannot easily be attributed to one of the two molecular groups in the crystal unit cell, only few of them will find a reliable assignment. The most important region is the spectral range below roughly 200 cm^{-1}, because it is there where interaction with the spin-system can be observed.

6.1. Temperature-Dependent Raman scattering

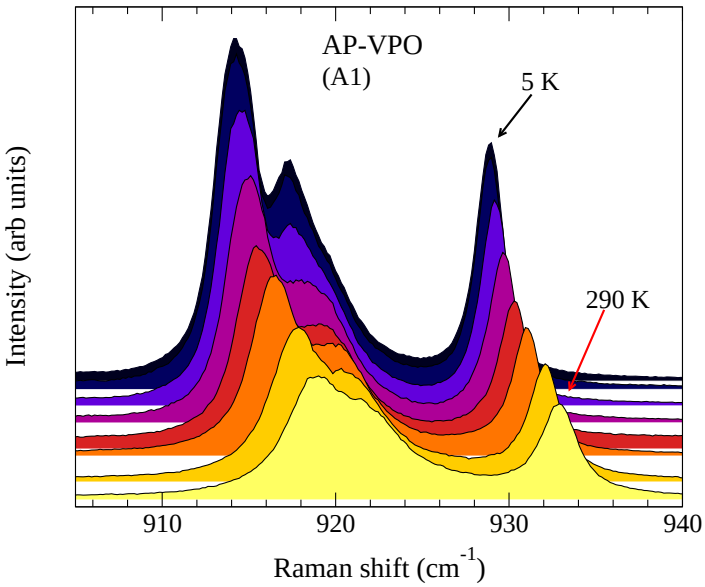

Figure 6.2.: Temperature dependence of the VO-vibrations of AP-VPO. The peaks are shifting to higher energies as a function of temperature, opposite to usual lattice anharmonicity.

Raman measurements as a function of temperature revealed several temperature dependent features. The modes around 915 cm^{-1} showed an unusual peak shift to higher energies with rising temperature, which is opposite to the usually observed anharmonicity of lattice modes (Fig.6.2). This point will be addressed in detail in 7.1.1. At temperatures below ≈ 20 K two shoulders appear in the Raman spectra of AP-VPO, shown in Fig. 6.3. This will be interpreted in chapter 9.1 as being spin-gap related Raman scattering. As shown in 4 the structure of AP-VPO revealed two inequal spin-chain systems. Scattering of two independent spin-chains would thus be a natural explanation of the appearance of two shoulders. Regarding the magnetic properties of AP-VPO and HP-VPO there are some remarkable differences in the spectra despite their crystallographic similarity. One of them is the "spin-phonon" mode in AP-VPO at 123 cm^{-1}. We have seen in chapter 2.4 how the temperature behavior of this mode was attributed to vibrations of the VO-plaquette and could be modeled theoretically. In contrast to the expectations the modes of HP-VPO in this range revealed pronounced differences (Fig. 6.4) to the AP-findings so that it will turn out in 9.3.2 that the Uhrig-model cannot be transferred to the HP-phase.

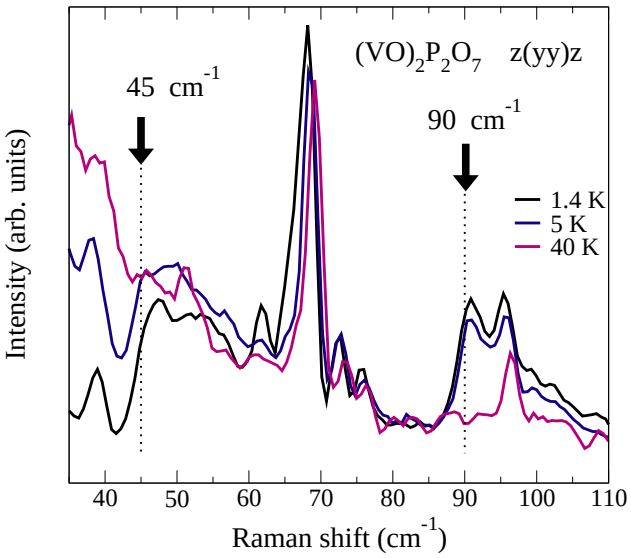

Figure 6.3.: Spin gap induced Raman scattering in AP-VPO. Excitations into the two-magnon continuum of two independent spin-chains appear at temperatures below ≈10 K as shoulders in the spectra, disappearing at higher temperatures.

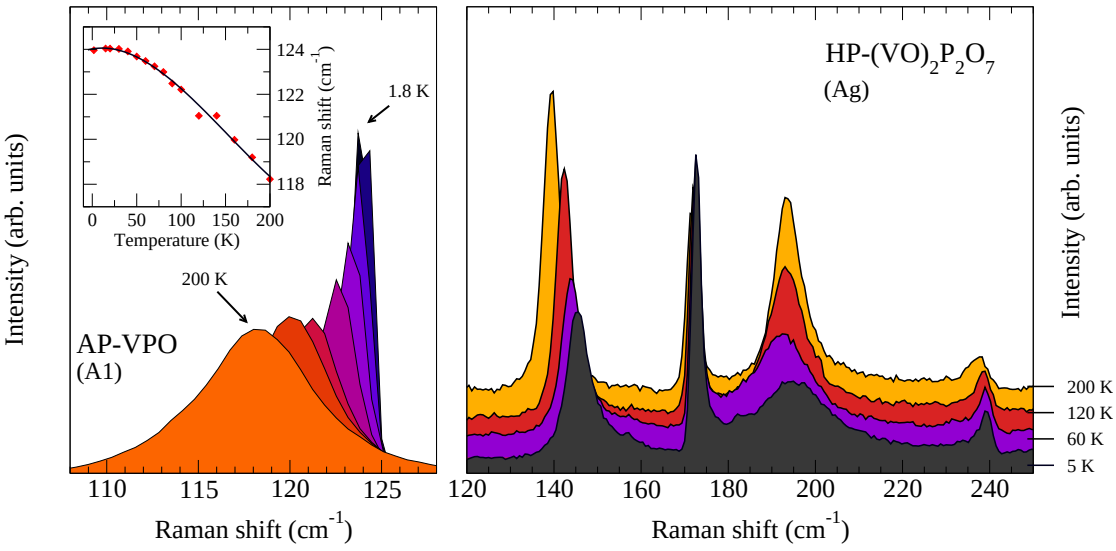

Figure 6.4.: Evidence for strong pin-phonon coupling in AP- and HP-VPO. (left) The "spin-phonon" mode of AP-VPO is strongly renormalizing with temperature. Shown in the inset is the temperature induced mode shift.(right) A comparable spectral range in HP-VPO revealed Fano line shape of some modes and opposite temperature behavior of line widths.

6.2. Raman scattering under high hydrostatic pressure

The results of the Raman measurements under high hydrostatic pressure revealed supplementary information about the features observed by the measurements as a function of temperature. We will see that the behavior of the VO-vibrations under pressure (Fig. 6.5) fits well into the model which will be developed in chapter 7.2.3 for the temperature dependence of these modes.

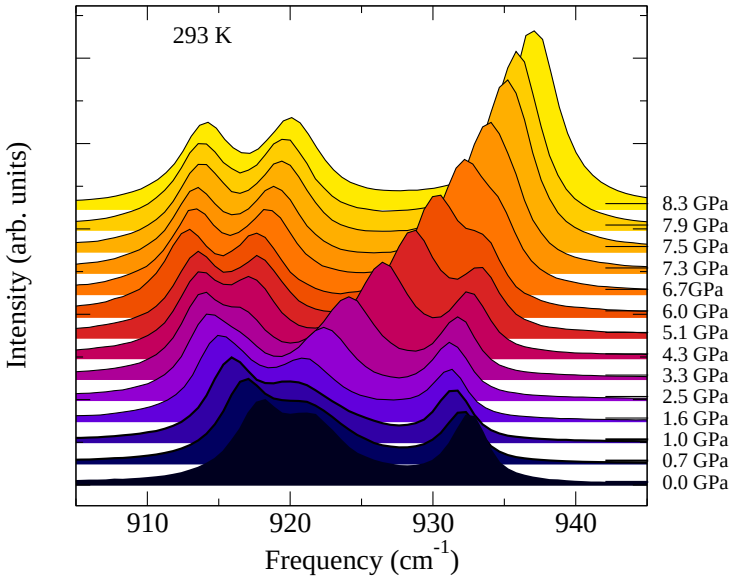

Figure 6.5.: Energy shift of VO-vibrations as a function of applied hydrostatic pressure

6.3. Infrared-Spectroscopy

The polarized infrared reflection spectra of AP-VPO and HP-VPO, to be displayed below in Fig. 7.3, show a similar distribution of modes as the Raman spectra and are dominated by the high-energy modes above ≈900 cm^{-1}. Since only room temperature spectra were recorded phonon anharmonicities or low-temperature effects do not show up in these spectra.

7. Experimental Results I: Phonon dynamics

In this chapter I will present the results of the Raman and infrared spectroscopy and discuss them as far as the observed features are related to lattice vibrations. The factor group analysis (FGA), which has been presented in chapter 5, revealed information about which normal mode can in principle be observed depending on the experimental conditions, however, it does of course not predict the frequencies of the normal modes. This information has to be drawn from other sources. The assignment presented below will be based on a comparison of spectroscopic results on related compounds and in combination with the FGA many of the observed lines can be assigned to eigenmodes of the crystal lattice. In both phases of VPO I found phonon lines which exhibit remarkable anharmonicities, which either are pure lattice effects or have to be contributed to interactions with the spin-system. However, the discussion of these modes will be postponed to chapter 9. The discussion of the mode assignment follows the argument in [82], the discussion of the mode anharmonicities is based on [83]

7.1. Interpretation of Raman- and IR spectra: Assignment of normal modes

7.1.1. VO vibrations

As shown in the overview in chapter 6, the Raman spectra of VPO consists of three distinct regions, with peaks around 915 cm^{-1} as the most prominent feature. In Fig. 7.1 this spectral range is displayed in an expanded view. The spectra were fitted by a sum of Lorentzian functions and four lines at 912, 916, 919 and 927 cm^{-1} are found for AP-VPO whereas in HP-VPO only one line at 911 cm^{-1} remains at this energy, thus indicating mode degeneracy in the HP-phase.

All peaks are most intense in xx polarization and less but equally intense in yy and zz polarizations. The depolarized spectra show weak peaks at the positions found in the polarized spectra. This is most likely due to some leakage of the polarized modes which, due to their high intensity has to be taken into account. Therefore the peaks have A_1 or A_g symmetry, respectively. If we compare these findings with the results of the FGO we see that the VO-stretching vibrations possess all observed properties, in particular the mode degeneracy of the four AP-modes into one HP-mode is predicted there. From a symmetry point of view an assignment to the VO stretching vibrations seems evident, however, how do the observed frequencies fit to that assignment? This question can be answered from literature where measurements on similar compounds have been re-

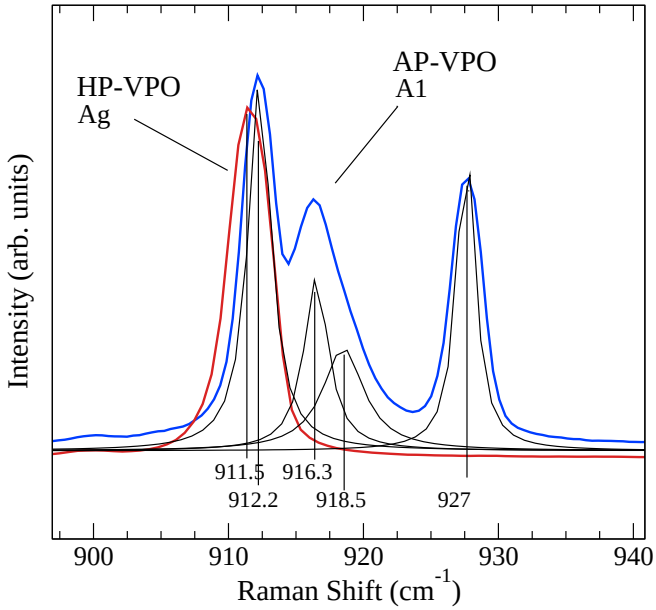

Figure 7.1.: Fit to the Raman spectra of the VO vibrations around 915 cm^{-1}. Four lines in the AP-phase (blue) degenerate to one line in the HP-spectra (red)

ported, e.g.[84, 85, 86]. Mahadevan *et al.* (1999) [86] examined $Rb_3(VO)_3(P_2O_7)_2$ and $CsVOP_2O_7$. They observed the VO stretching vibration at 978 cm^{-1} in the Cs compound and at 913 cm^{-1} in the Rb compound and related it to the different bond lengths of the apical oxygen of 1.592 and 1.606 Å, respectively. In crystalline V_2O_5 and alkali vanadates like LiV_2O_5 and NaV_2O_5 the related vibrations were found to exhibit frequencies at 994, 984 and 969 cm^{-1}, respectively [87, 88, 89]. Although the VO_5 pyramids are stacked in a similar way in the vanadates and in VPO, the interlayer distance between the vanadium atom and the apical oxygen atom from neighboring layers ($V - O1'$) is smaller in VPO. This point will turn out to be essential for the interpretation of the temperature dependence of these modes and will be discussed in detail below. Numerical calculations of the vanadyl vibrations have become available only recently. A density functional (DFT) study on geometrical, thermodynamic and electronic properties of vanadium oxide clusters [90] reported for the VO vibration frequencies around 1100 cm^{-1} for bond lengths of 1.55 Å between doubly bonded terminal oxygen atoms and vanadium. A conclusion may be drawn from the figures presented here which seems evident: the frequency of the vanadyl stretching vibrations scales with the bond length. However, as I will demonstrate soon, there is a large influence of the crystal environment, too.

As the VO dipoles are almost entirely oriented along the a axis of the VPO crystal, IR activity should occur in the corresponding polarization, which can be seen in Fig. 7.3. Therefore we assigned the strong band at 926 cm^{-1} in the IR(x) spectra to the infrared active counterpart of the V0 vibration.

7.1.2. P_2O_7 vibrations

The phonon spectra of the pyrophosphate (diphosphate, P_2O_7) group was studied intensively in solution [91, 92], in melted [93, 94] and in crystalline compounds [95, 96, 97, 98,

99, 86]. All authors accordingly found that the pyrophosphate vibrations are distributed with decreasing frequency in the order $\nu_{as}PO_3 > \nu_sPO_3 > \nu_sPOP > \delta OPO > \delta POP$, which was established by Bues *et al.* [93]. ν_{as} and ν_s refer to asymmetric and symmetric stretching vibrations of the terminal (PO_3) or bridge (POP) bonds, respectively; δ refers to the corresponding-bond bending vibrations, which are naturally lower in frequency. The frequencies for each of these types of vibrations in different compounds are always within the same frequency range, so that an unambiguous assignment of the high energy modes of VPO is possible.

Vibrations of PO_3 tetrahedra

The discussion of the high energy P_2O_7-modes will be quite detailed despite them being mere lattice vibrations. However, these modes and the fingerprint-like selection rules had been very useful to determine the orientation of unoriented crystal samples and for the validation of the MD calculations so that a closer look is justified.

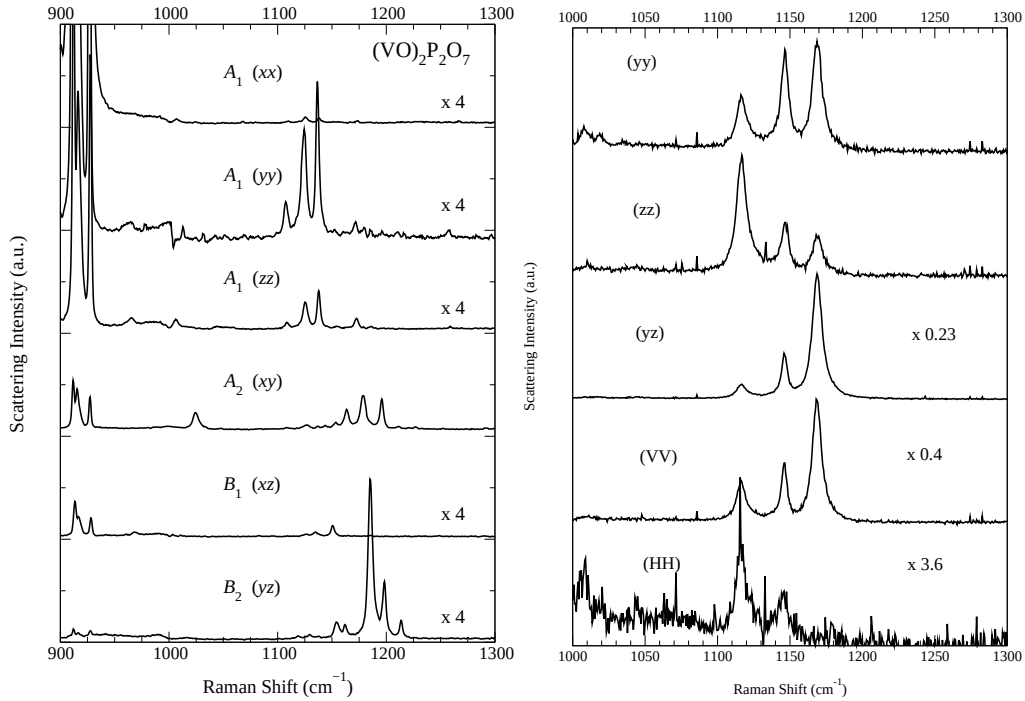

Figure 7.2.: Raman spectra of AP-VPO (left) and HP-VPO (right) in the energy range of the PO_3 stretching vibrations. The spectra of HP-VPO labeled with HH and VV were recorded from facets oblique to the crystal axes, therefore the peaks have mixed symmetry.

The asymmetric PO_3 terminal stretching vibrations ($\nu_{as}PO_3$) of the P_2O_7 group of different compounds are usually observed in the high-energy region from roughly 1050

to 1250 cm^{-1}. Figure 7.2 depicts the Raman spectra of this energy region. An inspection of the correlation tables for AP-VPO and HP-VPO (Tab. 5.2,5.4) predicts a total of 32 asymmetric PO_3 stretching modes for AP-VPO and 16 modes for HP-VPO. In AP-VPO the Raman-active modes are distributed equally among the symmetries A_1, A_2, B_1 and B_2 whereas in HP-VPO only 8 modes possess Raman activity, distributed among the A_g, B_{1g}, B_{2g} and B_{3g} symmetries. 24 Modes with A_1, B_1 and B_2 symmetry are IR active in AP-VPO, in HP-VPO the 6 IR modes possess B_{1u}, B_{2u} and B_{3u} symmetry, respectively.

In AP-VPO I observed 4 strong or medium intense modes in A_1, 3 in A_2 and 5 in B_2 symmetry, respectively. Due to the lack of suitable crystals faces on the HP-VPO crystals under investigation the Raman data are not complete in this energy range. Reliable spectra had been obtained only from a face which was oriented almost parallel to the xy-plane with some uncertainty and hence mixing from other scattering symmetries has to be assumed. I observed 3 lines in A_g symmetry at 1115, 1145 and 1170 cm^{-1}. The same peaks appear in the B_{3g} symmetry with the peak at 1170 cm^{-1} now being very strong. Considering the mode mixing the peaks at 1115 and 1145 cm^{-1} could be assigned to A_g symmetry and the peak at 1170 cm^{-1} to B_{3g} symmetry. This strong peak corresponds to a strong line at 1185 cm^{-1} in AP-VPO, there being observed in the same scattering symmetry (yz). The IR spectra (Fig. 7.3) of AP-VPO revealed 12 medium or intense peaks between 1100 and 1300 cm^{-1}. With the exception of the modes with the highest energy ($\geq$ 1219 cm^{-1}), the majority of the observed vibrational frequencies are close to those of the Raman lines which supports the premise of the crystal structure not being centrosymmetrical. In HP-VPO most of the PO_3 vibrations are degenerated, most noticeable at the modes polarized along the c-axis, but the distribution of the modes is preserved.

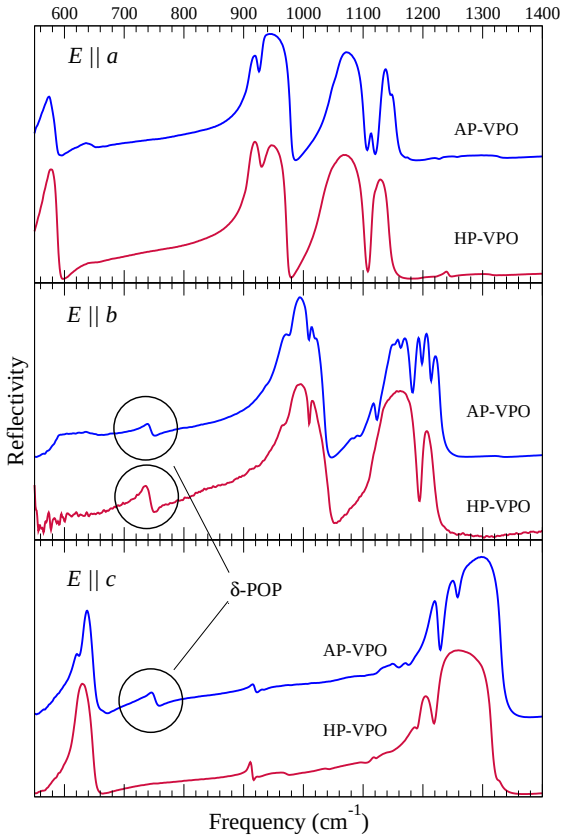

Figure 7.3.: IR spectra of AP-VPO and HP-VPO. The characteristic δ-POP vibration is labeled. In AP-VPO the vibration is present in b and c polarization, whereas in HP-VPO the vibration exists only in b polarization. The explanation is given in the text.

The frequencies of the symmetric PO_3 terminal stretching vibrations are, in general, expected below the asymmetric ones in the region between 900 and 1100 cm^{-1}. I'm restricting the discussion of these modes now to AP-VPO, because the arguments pre-

sented will apply for HP-VPO as well. For AP-VPO the factor group analysis predicts 4 Raman-active modes in each of the symmetries A_1, A_2, B_1 and B_2 and 12 IR active modes. We observed them in the Raman spectra as weak peaks at 965, 1005, 1020, 1047 cm^{-1} in A_1 symmetry and as a medium intense peak in A_2 symmetry at 1024 cm^{-1}. Strong modes appear in the IR spectra at 937, 976, 1011, 1062 and 1083 cm^{-1}. Again, the number of observed Raman and IR modes is smaller than predicted by group theory. For obvious physical reasons (see for example Cornilsen (1984) [98]) it has been established that those vibrational modes of the factor group are strong in the Raman spectra, which are derived from totally symmetric vibrational modes of the free-ion and, vice versa, those are strong in the IR spectra, which are derived from antisymmetric free-ion vibrations. If we consider the correlation of the terminal stretching modes of the P_2O_7 polyhedra to the factor group symmetry, we find in A_1 symmetry (with the symmetry of the free-ion mode given in parentheses) 2 $\nu_s(A_1)$ and 2 $\nu_{as}(A_1)$ modes and the same numbers for the other symmetries allowed in the factor group. Whereas this argument holds reasonably for the region of the $\nu_{as}PO_3$ vibrations, where 3 stronger peaks could be observed in most scattering geometries, it fails for the region of the ν_sPO_3 modes, where only weak peaks with less than 1/3 of the intensity of the $\nu_{as}PO_3$ vibrations could be observed. This is one of the remarkable differences of the spectra of VPO in comparison to other compounds containing P_2O_7 groups. In the alkaline earth compounds α-$Ca_2P_2O_7$, α-$Sr_2P_2O_7$ and α-$Ba_2P_2O_7$ the ν_sPO_3 vibrations appear as dominant peaks between 1050 and 1100 cm^{-1} [96], whereas the $\nu_{as}PO_3$ have lower intensities in the spectra. A similar picture is given by the Raman spectra of $Rb_2(VO)_3(P_2O_7)_2$ [86] or $Fe_2P_2O_7$ [100].

In the IR spectra strong modes appear between 900 an 1000 cm^{-1} in x and z polarization, which could be assigned to the ν_sPO_3 vibrations since they are expected in this range. However, this assignment is doubtful. First, in x polarization it would not be free of ambiguity. Here I was expecting the VO vibrations assigned to the 926 cm^{-1} mode before as well as the asymmetric ν_{as}POP bridge stretching vibration. Second, from a symmetry point of view, to be demonstrated in the next chapter, it is not possible for any pure ν_sPO_3 vibration to have a finite dipole moment in x or z polarization. This statement is supported by the absence of strong IR-modes in y polarization and thus the nature of the strong modes around 980 cm^{-1} in y polarization remain unclear.

POP stretching vibrations

The νPOP-bridge stretching vibrations are to a certain extent characteristic for the P_2O_7 polyhedra, since in the free-ion symmetry C_{2v} there is only one symmetric ν_sPOP vibration (A_1) and one asymmetric ν_{as}POP vibration (B_2). Factor-group splitting leads to 2 symmetric or asymmetric bridge stretching vibrations in all representations of the group C_{2v}^5. On the above stated grounds that crystal modes derived from symmetric or antisymmetric molecular vibrations are strong in the Raman or IR spectra, respectively, the symmetric vibration is usually (i.e. in a variety of compounds) found to appear strongly in the Raman spectra around 750 cm^{-1}[96, 97, 98, 99], whereas the IR activity depends on the amount of the POP-angle and disappears with vanishing dipole moment when the bridge is stretched linearly. The frequency of the ν_{as}POP vibration is expected

to be about 200 cm^{-1} higher than the symmetric one.

In AP-VPO I observed the symmetric POP stretching vibration in the IR spectra in *b* and *c* polarization at 743 and 750 cm^{-1}, respectively (Fig. 7.3). A closer examination of the polarization of the free-ion vibration as well as the orientation of the pyrophosphate groups on the two nonequivalent sites within the crystal unit cell reveals that the set of P_2O_7 polyhedra with P-O-P angles of 161 degrees is oriented to interact predominantly with radiation polarized in *b* direction whereas the set of P_2O_7 polyhedra with angles of 144 degrees interacts predominantly with *c* polarized light. A clear confirmation of this assignment is the polarization of this mode in HP-VPO. Here the plane of the POP-angles lies in the *a*-*b* crystal plane and thus the mode appears only in *b* polarization. For the same reasons which have been mentioned in the discussion of the νPO_3 vibrations the ν_sPOP vibration, as derived from a totally symmetric free-ion mode, is expected to appear in the Raman spectra with fairly large intensity. Surprisingly this was not found to be the case and the mode appears only very weakly in the Raman spectra at 750 cm^{-1}. I'm assigning the asymmetric ν_{as}POP stretching vibration to a strong peak in the IR spectra at 937 cm^{-1}. If this mode has the same frequency in the Raman spectra, it may be hidden by the very strong vanadyl vibrations around 920 cm^{-1}.

In the spectral region below 600 cm^{-1} the PO_3 terminal bending vibrations are expected. Since about two thirds of all internal modes of the P_2O_7 group appear in this region, an unambiguous assignment of vibrational modes to spectral features was not possible. In the study of Sarr *et al.* (1987) a linear relation between the bridge angle and the frequency of the bridge bending vibration δPOP was established. Applying this relation to the vanadyl anion of VPO and considering bridge angles of 144 and 161 degrees, we expect Raman and IR lines around 300 cm^{-1} and 245 cm^{-1}, respectively. A specific assignment was not carried out although some candidates for this mode are present in both the Raman and the IR spectra.

7.2. temperature dependence of anharmonic phonons

7.2.1. VO-vibrations

Lattice vibrations usually show a shift to higher energies when the temperature is lowered below room temperature. Only few cases are known where the reverse takes place, i.e. a phonon softening with lowering temperature and in those cases this behavior is restricted within a limited temperature range. Thus the temperature dependence of the VO-vibrations around 915 cm^{-1} of both phases of VPO, displayed in Fig. 7.4, has to be considered as remarkably unusual. The modes exhibit a continuous shift to higher energies when the crystal temperature rises from $\approx$ 2 K up to 290 K. The shift is almost linear at 290 K so that even above room temperature the frequencies will probably continue to rise. Obviously neither at 5 K nor at 290 K the observed energies are corresponding to the bare phonon frequencies so that an additional interaction which increases at lower temperatures seems to influence the VO-vibrations. In contrary to "normal" behavior, i.e. a shift to lower energies with rising temperatures, the anharmonicity of the bond potential seems to be inverted in the sense that higher temperatures lead to smaller

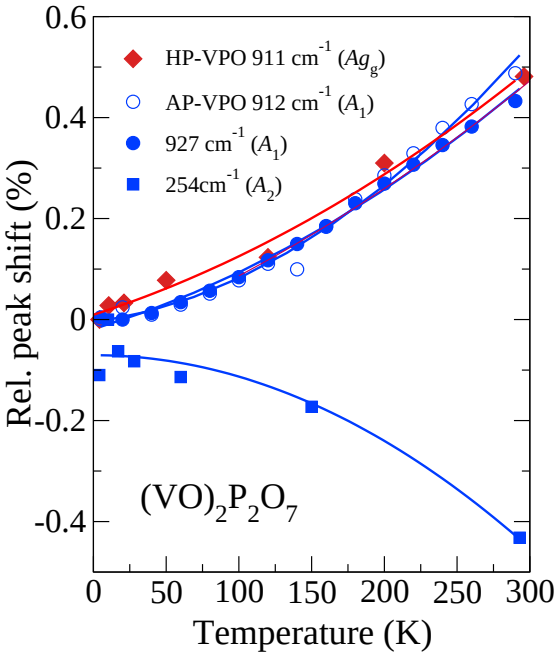

Figure 7.4.: Temperature dependence of the VO vibrations in AP- and HP-VPO, together with fitting functions. A mode at 254 cm^{-1} (AP-VPO, A_2) with "normal" behavior is shown for comparison. The energy shift of the VO vibration in AP-VPO and HP-VPO is all about the same.

mean distances during vibration. Before I discuss this feature it should be noted that all modes in this energy range, whether they belong to AP-VPO or the HP-phase reveal similar slopes for the shift. Since no further modes show this unusual shift this feature gives an additional justification for the assignment to the same lattice mode, the stretching vibrations of the vanadyl group.
Whereas to my knowledge no other vibrational spectra with such a temperature dependence has been reported a comparable feature had been observed in NaV_2O_5 with Raman scattering under high pressure [101, 102]. In this compound the vanadium atoms are pyramidal coordinated to the oxygen atoms, too, and the VO_5 pyramids form layers with the Na atoms intercalated in between. The vanadyl group (vanadium + apical oxygen) stretching vibration has a frequency of 969 cm^{-1} at ambient pressure and it decreases to $\sim$ 919 cm^{-1} under a hydrostatic pressure of 15 GPa. A study of the lattice parameters as a function of pressure revealed a significant anisotropy in the compression moduli of the crystal axis. The distance between the VO_5 pyramid layers along the crystallographic c-axis decreases more than x times stronger than in the other crystal directions. Hence the distance of the apical oxygen to a neighbor layer decreases strongly so that the pyramidal coordination changes into a more octahedral one. Both, the oxygen and the vanadium atom carry charges and therefore are supposed to interact by coulomb forces. Thus the increasing influence of the interlayer $V-O1'$ bond effectively weakens the intralayer V=O1 bond which leads to the observed softening.

As far as concerning the coordination of the vanadium atom we have a similar situation in VPO when the temperature is changed. The lattice constants are expected to decrease and thus by decreasing the interlayer $V-O1'$ distance an increased interaction between these atoms takes place which results in an energy loss of the VO-vibration.

In order to compare the above model for NaV_2O_5 with the situation in VPO quantitatively I made an estimation of the thermal expansion coefficient along the vanadyl axis in VPO by transferring the observations from NaV_2O_5. In NaV_2O_5 a contraction from 3 to 2.3 Å corresponds to a frequency shift of 50 cm^{-1}, giving a relative shift of 71.4 cm^{-1}/Å. In VPO the relative shift caused by temperature change is 0.0154 cm^{-1}/K. With the assumption that similar changes in the length of the crystal axes cause similar frequency shifts of the VO-vibrations dividing both numbers reveals a relative change of the crystal cell length of 2.16^{-4}Å/K. By dividing this number by the length of the a-axis, the vanadyl axis in VPO, we finally obtain a linear expansion coefficient of $\approx 2.8 \times 10^{-5} K^{-1}$. In order to prove this value I suggested a temperature sensitive crystallographic study of the length of the crystal axes in AP-VPO which was performed by P. Daniels in the laboratory of crystallography at the University of Bayreuth [103]. In his X-ray study of

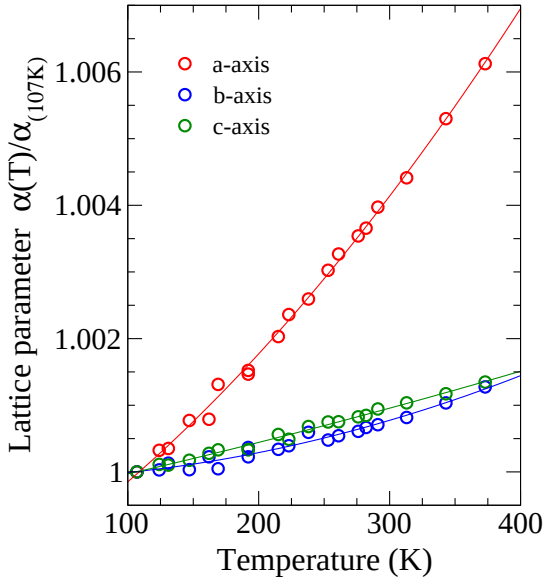

Figure 7.5.: Lattice parameter of VPO as function of temperature, determined by x-ray diffraction [103]. The a-axis has a large thermal expansion coefficient and a contraction of this axis is likely to have a large influence on the vanadyl vibration, which is oriented along this direction.

the lattice constants of VPO between 107 K and room temperature, depicted in Fig. 7.5, he found VPO to exhibit a strong anisotropic thermal expansion with expansion coefficients of $\alpha_{b,c} \approx 5 \times 10^{-6}\,K^{-1}$ perpendicular to the vanadyl axis and $\alpha_a \approx 2.3 \times 10^{-5}\,K^{-1}$ in the direction of the VO-bond,- which fits well to the value I have obtained above.

7.2.2. Low-energy anharmonic modes in AP-VPO

Due to the low crystal symmetry the spectral region below $\approx$ 600 cm^{-1} is densely filled with lines, originating in bond bending and external modes. One of them, an A_{1g}-mode at 123 cm^{-1} shows a remarkable temperature dependency which has first been reported in [104] and was displayed above in Fig. 6.4. The unusual large mode softening was attributed to a coupling of this mode to the spin-system, therefore a detailed discussion of the mode will follow in the forthcoming chapters. Here I will only note that this mode was supposed to originate in a vibration of the whole VO_4 plaquette and since AP- and

HP-VPO are similar in this respect the question raised whether there was as similar mode in the HP-phase. The discussion of this point will be resumed in the presentation of the Raman measurements under hydrostatic pressure. Apart from the spin-phonon mode at 123 cm^{-1} most of the other modes show normal temperature behavior. However, a few very weak lines exhibit an unusual decay of their intensity with increasing temperature, which is displayed in Fig.7.6. The energy of these modes decreases sharply around ≈

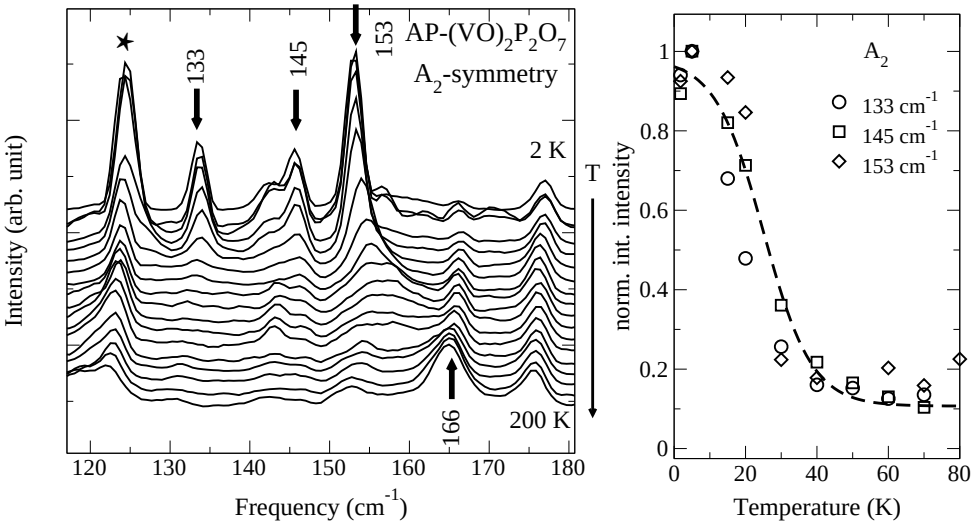

Figure 7.6.: Low energy modes of AP-VPO exhibiting a sharp intensity decay around 20-30 K. The transition temperature corresponds to the energy of the lower spin-gap (≈ 30 K), which suggests that interaction with the spin system is responsible for the decay.

22 K, which in general would indicate a structural phase transition. However, no other evidence for that assumption was observed and in view of the vast majority of phonon modes with "normal" behavior a phase transition seems unlikely. The nature of this decay could not be resolved finally but rather than being related to a phase transition I would suggest a connection to the dynamic of the spin-system, which I will show below to scale on the same energy range (i.e. below 200 cm^{-1}).

7.2.3. Low-energy anharmonic modes in HP-VPO

To complete the presentation of phonon anharmonicities I will briefly address the low energy modes in HP-VPO. From the structural similarity of both phases I expected to observe a mode corresponding in behavior to the "spin-phonon" mode in AP-VPO at 123 cm^{-1}. Instead of that the measurements revealed a different picture. In the overview in Fig. **??** the spectra of the low-energy range of HP-VPO as a function of temperature have already been shown. At low temperatures peaks at 145, 172 and 194 cm^{-1} exhibit a Fano lineshape, which usually indicates a strong interaction with a background of elementary excitations. From these the mode at 194 cm^{-1} displays the most pronounced temperature dependency. Apparently the interaction strength increases at low temperatures. The

detailed discussion of these findings will take place in a later chapter, where the fano lineshape will be connected with the continuum of spin excitations.

7.3. pressure dependence of anharmonic phonons

7.3.1. VO-vibrations

In the preceding paragraphs I have shown how the interlayer interaction between the vanadyl groups stacked along the *a*-axis has a significant influence on their phonon frequencies which manifests itself in an unusual energy shift as a function of the lattice temperature. The question was whether applying high pressure would cause a similar effect, such as it has been observed in NaV_2O_5 [101, 102]. In Fig. 7.7 the impact on the vanadyl vibrations of applying hydrostatic pressure on AP- and HP-VPO up to 8.6 GPa are summarized. Up to a moderate pressure of about 2.5 GPa (HP-phase: 1GPa) a softening of all modes is observed thus partly confirming the above supposition. However, above these values the behavior returns to the normal increase of energy with pressure. Different from NaV_2O_5 where it has been shown that the compression modulus along the vanadyl axis is very small, the vanadyl layers in VPO are linked along the *a*-axis by pyrophosphate groups. A potential explanation for the reverse of the pressure induced shifts would be that the linking over the pyrophosphate group prevents the lattice from further contraction along the *a*-axis at pressures above 2.5 GPa. However, this assumption could only be proven by a detailed X-ray examination of the lattice parameters under high pressure as it had been performed with NaV_2O_5. A mode at 919 cm^{-1} in the AP- phase deviates from the otherwise almost uniform pressure dependence and sheds some doubt on the assignment of this mode to a vanadyl VO vibration since from a symmetry point of view none of the vibrations split by factor group should differ

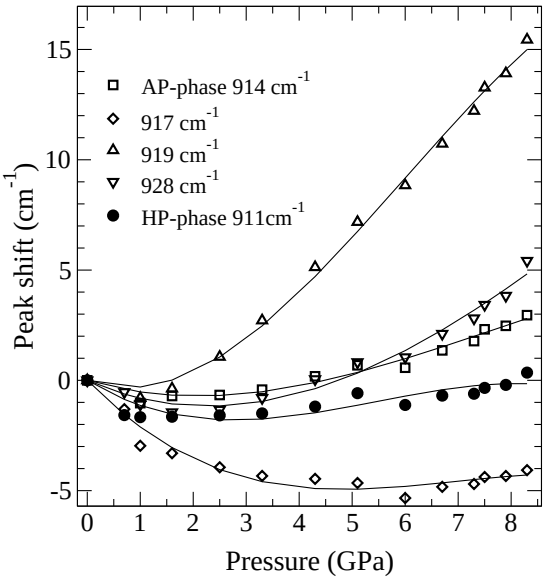

Figure 7.7.: Raman shift as a function hydrostatic pressure of the V-O vibrations in AP- and HP-VPO. The curves of both graphs are 3rd order fits to the peak positions as a function of applied pressure. A small downshift is apparent before all modes tend to harden with increased pressure. The offset of the mode shifts between 5 and 6 GPa is a calibration artifact.

from the average frequency by more than a small amount. Furthermore, with increasing pressure this mode becomes much more intense than the others (see Fig. 6.5) so that it is more likely a vibration of different origin, too weak and therefore covered at ambient pressure. A possible candidate for such a vibration is the asymmetric ν_{as} POP vibration expected at this energy [82].

7.3.2. Low-energy modes

By measurements under high pressure further information about the nature of the observed vibrations can be obtained from their specific energy shift and thus provide additional clues for the assignment of these modes. In figures 7.8 I juxtaposed the Raman spectra of AP-VPO and HP-VPO as a function of applied pressure. By fitting each of the lines in the spectra with Lorentzians I obtained the slopes for the observed modes. Fig. 7.9 (left) displays a selection from these.

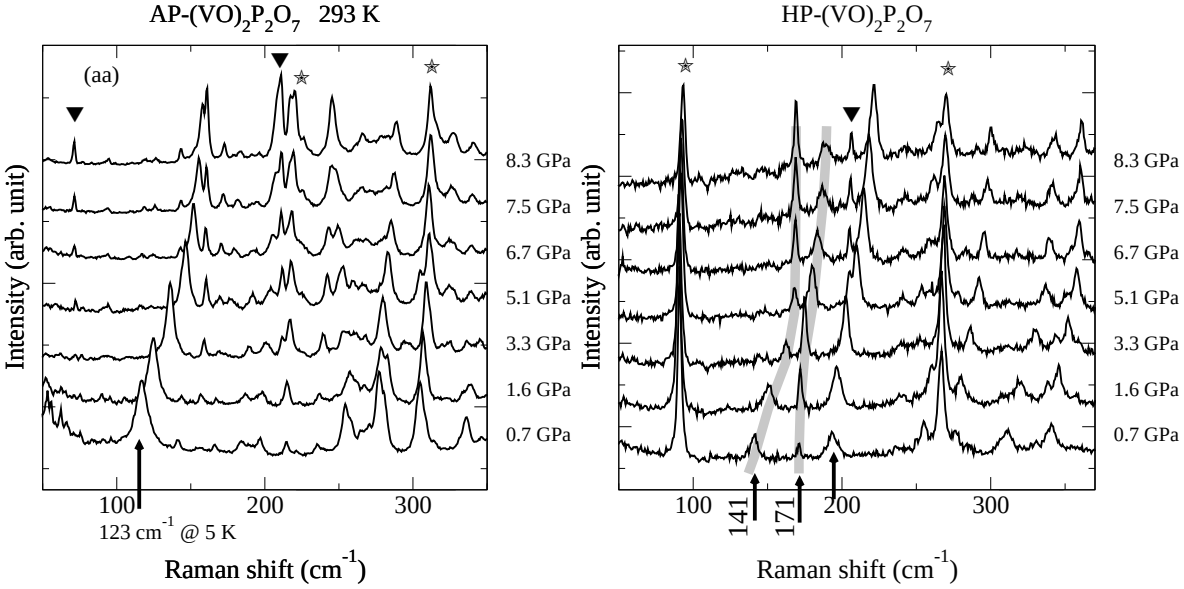

Figure 7.8.: Low-energy Raman spectra of AP-VPO and HP-VPO. The measurements on AP-VPO were performed on small unoriented fractures of single crystals whereas HP-VPO was investigated as polycrystalline material. Compare the HP-VPO spectra with Fig. 6.4, where some of the modes are displayed, too.

Following an idea evolved by Zallen in 1974, recently applied by Jakšić [105, 106], I tried to sort the vibrations into those with more *internal* and more *external* character, in order to find evidence for the distinction formulated in the FGA (5). Zallen noted that the Grüneisen approximation, where the mode Grüneisen parameters $\gamma_i(\nu_i)$ of a crystal are assumed to be equal $= \gamma$, is broken down in molecular crystals and two different scaling laws hold for both types of modes. For the external modes $\gamma_i = \text{const}$ whereas the internal modes follow approximately the scaling law $\gamma_i(\nu_i) \propto \nu_i^2$ [105, 107]. The pressure effect on a mode ν_i can be expressed in terms of the mode Grüneisen parameter

$\gamma_i(\nu_i)$ as:

$$\gamma_i = -(\partial \ln \nu_i / \partial \ln V) = (1/\beta\nu_i)(\partial\nu_i/\partial P), \tag{7.1}$$

where V denotes the crystal volume, P the pressure and β the isothermal compressibility. With that the fractional change in frequency under pressure P is connected to the volume dilation by:

$$(\Delta\nu_i/\nu_i) = -\gamma_i(\Delta V/V) = \gamma_i\beta P. \tag{7.2}$$

Since $(1/\nu_i)(\partial\nu_i/\partial P) \propto \gamma_i$, by plotting this value over ν_i the frequency dependence of

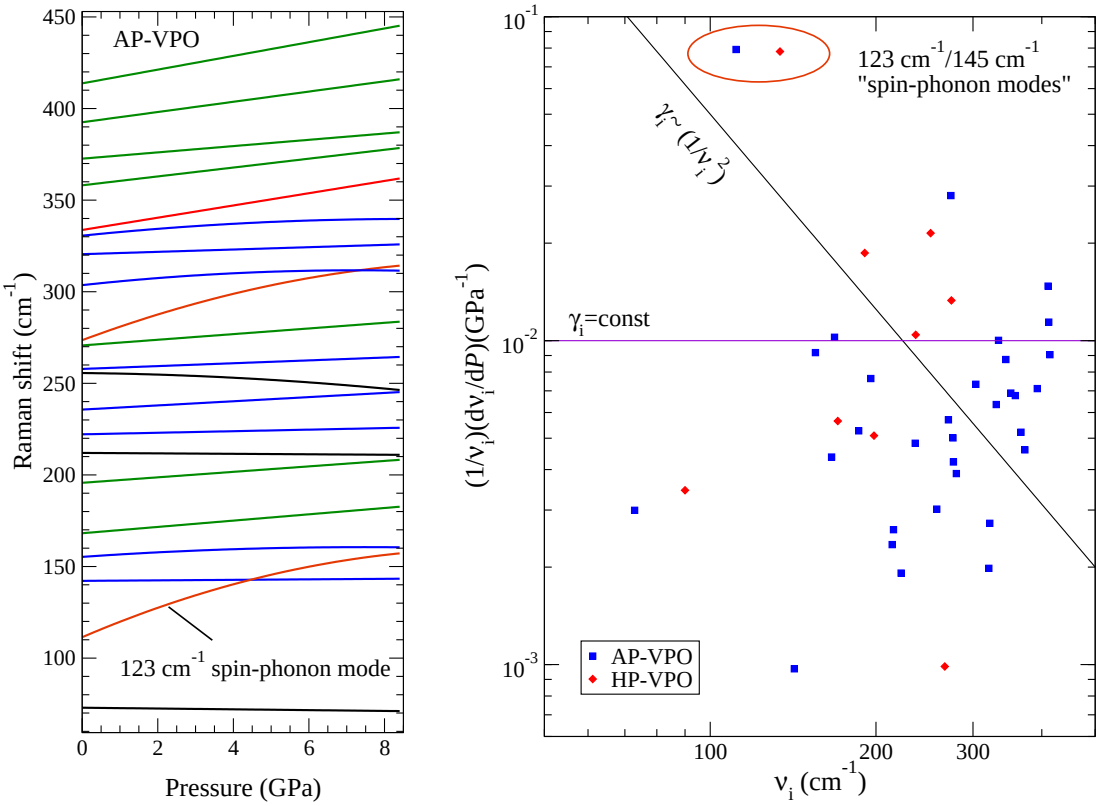

Figure 7.9.: (left) Pressure slopes of selected low-energy modes of AP-VPO. Only fits to the data are shown for clarity. The colors mark modes with similar mode shifts. Black – negative shift; blue, green – moderate positive shift; red – large positive shift. (right) Evaluation of the mode shifts according to [105]. Blue and red symbols denote shifts of modes of AP-VPO and HP-VPO, respectively. Refer to text for the explanation of this graph.

γ_i can be shown, displayed in Fig. 7.9 (right). In this graph the mode shifts of several AP-VPO and HP-VPO low energy modes are included. The two lines mark $\gamma_i = \text{const}$ and $\gamma_i(\nu_i) \propto \nu_i^2$. This evaluation reveals that the modes of VPO do neither follow the

usual behavior of $\gamma_i \approx$ const, typical for covalent crystals, nor a clear tendency towards a scaling law of molecular crystals is discernible, although some tendency in that direction is present. Two modes with striking high γ_i which are marked in the graph are the spin-phonon mode in AP-VPO and its supposed counterpart in HP-VPO, more on that below. In conclusion, VPO shows a very heterogeneous character where presumably the inter- and extramolecular forces are different, but not so much to establish full molecular crystal properties. The complicated character of the inter- and extramolecular forces of VPO are subject of the next chapter, too.

I am resuming now the discussion of Fig. 7.8. Some modes show a very strong positive energy shift as a function of applied pressure. This applies in particular for the SPP-mode in AP-VPO at 123 cm^{-1}, which revealed a strong pressure shift whereas the majority of the modes show only small or even negative slopes. Besides that a few new lines seem to appear. Comparing the measurements of both crystal phases in Fig. 7.8 there is a noticeable similarity between the pressure induced shift of the SPP-mode at 123 cm^{-1} in AP-VPO, which is supposed to be a vibration of a whole VO_4 plaquette [104], and a mode at 141 cm^{-1} in HP-VPO, also visible in Fig. 7.9. This mode has already been described in the preceding section as revealing an unusual temperature dependence. However, in the course of my research the measurements under pressure had been performed on polycrystalline samples first and the unusual temperature behavior of this mode was not revealed before high-quality single crystals became available. The slope of the 141 cm^{-1} mode seems to saturate around 5 GPa whereas the mode

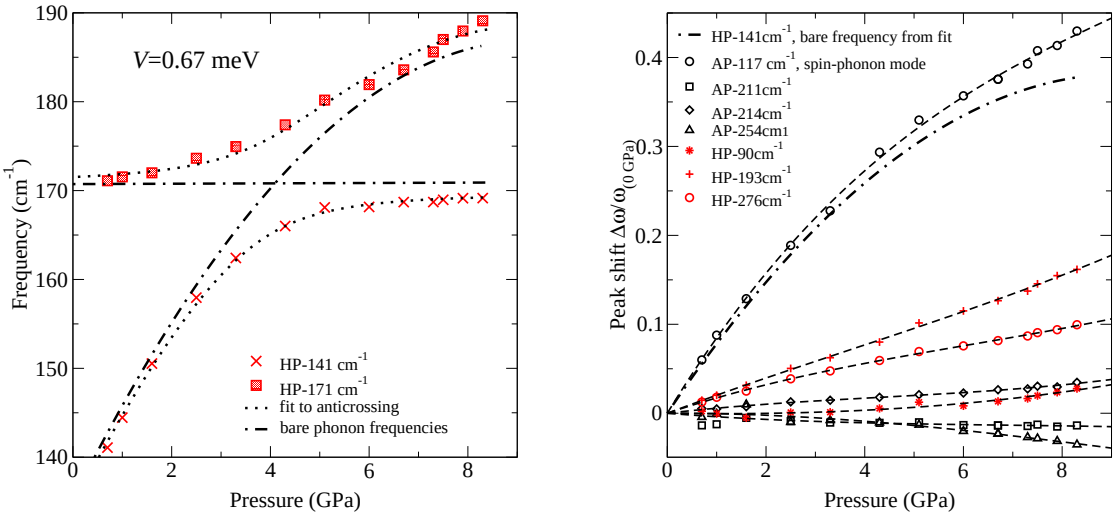

Figure 7.10.: The spin-phonon mode at 123 cm^{-1} in AP-VPO and a mode at 145 cm^{-1} in HP-VPO reveal similar large mode shifts under pressure (right panel) if a mode anticrossing of the latter mode with a mode at 171 cm^{-1} is taken into account (left panel).

at 171 cm^{-1} (0 GPa) begins to shift strongly at this pressure. Such behavior is usually contributed to a mode anticrossing, which is possible if both modes are interacting

with each other and possess the same symmetry. I examined this by fitting both modes under the assumption of a constant interaction potential of 0.67 meV and obtained a linear pressure slope of 0.23 cm^{-1}/GPa for the 171 cm^{-1} and a quadratic dependence of $\omega(p) = 11.2(cm^{-1}/GPa)p - 0.61(cm^{-1}/GPa^2)p^2$ for the 141 cm^{-1} mode, displayed in Fig. 7.10 (right panel). With these functions as the "bare" pressure dependency both modes, the SPP-mode at 123 cm^{-1} (AP-VPO) and at 141 cm^{-1} (HP-VPO) reveal same slopes , displayed in Fig. 7.10 (left panel), thus giving strong evidence of the assignment of this mode as being the counterpart of the SPP-mode in the HP-phase. However, as stated above the measurements at low temperature revealed a very different temperature dependency of both modes which seems to contradict this assignment. Since this aspect is most likely related to interactions with the spin system I will no longer pursuit the discussion of this findings here. Instead, I will refer to the chapter on spin dynamics where I am going to put up this point again with the discussion of the fano-modes under pressure.

7.4. Summary

In this chapter I discussed the Raman and IR spectra of both crystal phases of VPO with focus on lattice vibrations. By comparison with literature data of related compounds and symmetry considerations I was able to assign all spectral features above 700 cm^{-1} to definite eigenvectors of the crystal. The higher symmetry of the HP-phase compared with the AP-phase is reflected in a mode degeneracy of the phonons. Measurements at temperatures between room temperature and 4 K and measurements under high hydrostatic pressure revealed that some lattice vibrations of VPO show remarkable anharmonic behavior. The prominent V=O vibrations around 910 cm^{-1} exhibit a shift to higher energies almost proportional to the crystal temperature, which contrasts with the usual observed phonon behavior. I presented an interpretation of this behavior based on a temperature induced change of crystal environment influence on that particular vibration and derived a simple model potential which renders this effect.

By comparing the pressure induced energy shifts of the low energy modes I identified the phonon counterpart of the spin-phonon mode of AP-VPO in the HP-phase at 145 cm^{-1}. Measurements at low temperature revealed that this vibration, which is supposed to be a vibration of the VO_4 plaquette, exhibits a strong anharmonicity in HP-VPO, too. The discussion of this mode will be resumed in the chapter on spin-dynamics in VPO.

8. Molecular dynamics simulation of the phonon spectra

The phonon dynamics and the interpretation of vibrational spectra of VPO is complicated by the large unit cell, which was examined in chapter 4. By comparison of related compounds and by making use of symmetry properties I have shown in the preceding chapter that many spectral features, in particular those in the high-energy range, could nevertheless be assigned to eigenvibrations of the lattice. In order to examine further certain kinds of vibrations, e.g. the spin-phonon mode or the unusual anharmonicity of the VO vibrations I tried to model the system with standard molecular dynamics (MD) and to calculate the eigenfrequencies and eigenvectors of the lattice vibrations. Although the final objective, the simulation of lattice anharmonicities could not yet be achieved, a basis for further developments is given.

This chapter is organized as follows: after briefly addressing the computational techniques I will describe the model and the steps required to calculate lattice vibrations. I will then report on the results of MD of a harmonic lattice and compare the results with my spectroscopic observations.

8.1. Molecular Dynamics

Molecular dynamics, in contrast to ab-initio methods, are based on empirical knowledge of the system under consideration. The predictability of the method is therefore restricted to cases where the essential model parameters are not changed during the simulation. The MD approach is essentially the stepwise integration of Newtons equation for a system consisting of N particles with interaction potentials $U_{ij}(r)$:

$$m\ddot{x}_i = F_i, \boldsymbol{F}_i = -\sum_{j=1,j\neq i}^{N} \frac{\partial u_{ij}(r)}{\partial \boldsymbol{r}_{ij}} \tag{8.1}$$

During MD simulation certain macroscopic variables, as of temperature T, pressure p or volume of the simulation cell V are controlled by the MD-code to ensure compatibility with the boundary conditions, which are imposed e.g. by the choice of a thermodynamical ensemble for the simulation. The main input of a MD run is the structure information, i.e. the position of all particles in the simulation, and the force-field (FF), which comprises information of all kinds of interactions between the particles as well as external forces as e.g. gravity or an electric or magnetic field. In the following description of the MD input I will refer to the program DL-POLY, which I have used for the simulation. DL-POLY is a molecular dynamics simulation package developed at Daresbury

Laboratory by W. Smith and T.R. Forester an is issued free under licence to academic institutions. Details can be found on the homepage of the program at DL-POLY[108].

8.1.1. Input Files

Structure: CONFIG

The structure information required for the simulation is provided by the CONFIG file. This comprises of at least one unit cell, and thus 52 or 104 atoms in HP-VOPO and AP-VPO, respectively, for which absolute coordinates in the simulation space have to be given. However, I found that for the calculation of eigenfrequencies which are not depending on the simulation size, simulation cells of 3x3x3 or even 5x5x5 unit cells had been necessary. A cubic simulation cell is required for the calculation of eigenvalues by diagonalization. In the case of AP-VPO that means that 13000 atoms are involved in the simulation, just about the number of atoms which could be handled in a manageable time. DL-POLY, as most MD programs involves a mirroring algorithm, which means that calculations are performed on an unbound lattice and all forces wrap over the faces of the simulation cell. The data for the CONFIG file are based on recent structure determinations for VPO, ref. [70] for AP-VPO and ref [65] for HP-VPO, respectively.

Force-field: FIELD

The force-field is the essential input to MD because it comprises a full description of the interatomic forces in the simulation. The ingredients are prepared in the form of force constants for several types of valence bonds, e.g. bond stretching constants between pairs of atoms and bond bending constants describing the bend of the angle between three atoms (triples) and others as well as non-local forces as the Van-der-Waals potentials. Many MD packages have their own FF implemented so that e.g. for the simulation of a CH or CO bond only atomic numbers and positions are fed into the program which will then choose the required potentials. For DL-POLY a complete FF has to be built up in the FIELD file where for *each* given bonded pair, triple or quartuple of atoms in the simulation cell the force constants of bond-stretching, bond bending and others have to be given. In a small simulation cell this can be done manually. In the large cells which I applied in my simulations it is no longer trivial and it has to be performed automatically requiring additional software which in parts I had to develop for this purpose. From N atoms in the simulation cell in principle $np = \binom{N}{2}$ tuples of atoms can be formed. From these those which are bonded, that is which have distances smaller than some preadjusted value have to be selected. This is performed by software supplied with DL-POLY which has as its output all pairs, triples, quartuplets of atoms which are *potentially* bonded in a specific way. In a last step in the generation of the FIELD file for only those atom pairs, triplets etc. which are *actually* to be bonded in a selected way the force constants have to be supplied. Last not least it is important to check here whether the mirror-convention is obeyed correctly, i.e. whether all bonds wrap around the simulation cell reliable. A FIELD file for AP-VPO (13000 atoms) has a

size of 3.5 MByte and consists of 18000 bond stretching constants (pairs), 26430 bond angle constants (triples) and 950 bond torsional constants (quartuplets) together with the VdW parameters. From that it is clear that stepping to an even larger simulation cell or introducing a more evolved simulation model would blow up the size of the FIELD considerably and preclude calculations to be finished in reasonable intervals.

8.1.2. The force-field for VPO

The description of the FF above referred only to a certain type, the valence FF, which is applied mainly for the modelling of molecules and covalent crystals. However, for the modelling of pure ionic crystals or crystals with mixed ionic-covalent character as represented by VPO this is not appropriate. In solid state physics several models had been developed to deal with the polar character of the bonding. I will note here only the core-shell model and the valence-shell model. In the core-shell model the ionic polarizability of an ion crystal is modeled by splitting the charge of an ion into two parts: in the simplest case a rigid core with charge q_c and a spherical shell with charge q_s an mass m_s. The polarizability of the ion is then represented by a core-shell spring force constant $k = q_s m_s \omega_0^2$, where the frequency ω is chosen to be much larger than the expected phonon frequencies. To model the interaction between neighboring ions a variable number of parameters were chosen to represent the mutual interaction between cores, shells and cores and shells. Cochran applied a five parameter model to fit the phonon dispersion of Ge [109]. Others applied extended models with 11 parameters to fit the phonon dispersion of Si [110]. However, it should be added here that W. Weber developed a better model for the lattice dynamics of semiconductors, the adiabatic bond-charge model [111].

The valence-shell model is essentially a combination of the aforementioned core-shell model with a valence force model, that is, directional bonds are represented by valence forces between the shells and ionic polarizabilities are introduced by a core-shell force constant. With a model of this type Popović *et al.* [89] were able to calculate the lattice vibrations of NaV_2O_5, a spin-Peierls compound structurally related to VPO. Although in principle this model could be set up with DL-POLY, it is rather complex and therefore I started with a pure valence force field.

The parameters used as starting values were taken from a work of Ritschl *et al.* [112]. In this work the structure of VPO has been examined with regard to the catalytic properties and lattice dynamics had not been taken into account. The force constants provided by Ritschl and coworkers render the observed vibrational frequencies only in some cases and had to be adjusted to approximate the observed spectra.

The FF for AP-VPO and HP-VPO were taken as almost identical, i.e. atoms or groups of atoms on similar sites of both phases are bonded with the same force constants. This was chosen in order to investigate the effects of mode degeneration. The valence forces could in principle be given as anharmonic forces which would then require the input of additional parameters. However, the choice of the force constant parameters requires some knowledge *a-priori*, e.g. frequencies of certain vibrations which in the case of the anharmonic terms are not known and could only be guessed. With the exception of the

VO vibrations which are dominated by anharmonic effects (see 7.2.1) I have therefore excluded anharmonicity from the simulations and could thus limit the calculation time considerably.

Values for the force constants as well as for the VdW parameters were compared with MD calculations of related compounds and were successively improved by optimizing the resulting phonon spectra towards the observed ones. A great difficulty in the construction of the FF of VPO was found in the specific mixture of valence and coordination bonding. The valence bond stretching forces are usually strong and give rise to distinct phonon lines. This made it easy to simulate the PO_x vibrations which have the highest frequencies in the phonon spectra of VPO. Likewise the short vanadyl VO vibration could be modelled by one force constant. In contrast to that coordination bonding, as e.g the corner oxygen atoms of the basal planes of the Vanadium coordination pyramids has a more non-directional character which is not easy to implement. Calculations with only VdW and Coulomb-forces for these bonds revealed no stable structures so that the coordination had to be simulated by bond-stretching and bond-angle potentials. Since in the VPO unit cell all atoms are ionized to a certain degree a core-shell model seems to be advisable and was found to be necessary for the successful simulation of transition metal compounds [113, 114, 115]. However, that would have doubled the number of particles and increase the FF considerably, therefore the ions were treated as non-polarizable units.

8.2. Calculation of eigenfrequencies and eigenvectors

The MD itself does nothing but to advance the atoms in the simulation under the influence of the mutual forces, as it integrates numerically the Newton equations of the system. To obtain vibrational frequencies several steps are required, which I will outline here briefly. Details are found in many textbooks on solid state physics as e.g. in ref. [116]. Starting point for the numerical calculation of phonon spectra is the secular equation of the system in the form:

$$\sum_{m}^{N}[D_{kk'}(\boldsymbol{q}) - \omega^2\delta_{kk'}]\boldsymbol{u}_{k'0} = 0 \tag{8.2}$$

Here D denotes the dynamical matrix in the harmonic approximation:

$$D_{kk'}(\boldsymbol{q}) = \sum_{m}^{N}\Phi(mk, 0k')(M_k M_{k'})^{-1/2}\exp[-\mathrm{i}\boldsymbol{q}\cdot\boldsymbol{R}_m]. \tag{8.3}$$

The force constant matrix Φ describes the force exerted on atom kl

$$\boldsymbol{F}_{kl} = -\Phi(kl, k'l')\boldsymbol{u}_{k'l'} \tag{8.4}$$

by a small displacement $\boldsymbol{u}$ of atom $k'l'$. Thus $\Phi(kl, k'l')$ is given by $-\boldsymbol{F}_{kl}/\boldsymbol{u}_{k'l'}$. To obtain these force constants numerically, n.b *force constant* has a different meaning here

in contrast to the force constants of the FF, one has to displace all the atoms of the unit cell along the three Cartesian components by $\boldsymbol{u}_{k'l'}$ and to calculate the forces induced on all atoms in a neighboring unit cell. On the beginning of the calculation the lattice has to be completely relaxed so that all atoms are free of forces. If the FF would give an accurate representation of the crystal, this step would not be necessary but the chosen FF is of course only a more or less good approximation of the real situation. Therefore the system has to be relaxed for some simulation time in order to render the atoms free of forces. The deviation of the crystal after the relaxation step from the starting configuration is a direct measure of the quality of the FF, and several adjustments had to be done until the deviations of the atom positions where small enough so as to assume that they do not have influence on the frequencies obtained. The simulation is then run with the displacement of one atom in one direction and the forces exerted on the other atoms are then collected from the program output. This step has to be repeated $6N$ times for the N atoms in the unit cell. If the force constant matrix has been constructed in this way, frequencies are then calculated by diagonalizing the matrix. The DL-POLY package does not provide code for that, therefore I adapted the procedure for the utilization of the program VIBRATOR of the SIESTA ab-initio package SIESTA. The output of VIBRATOR are the eigenfrequencies and eigenvectors of the lattice vibrations.

8.3. Symmetry classification and generation of computed spectra

To obtain a better overview over the literally hundreds of possible vibrations I then classified the vibrations according to their symmetry. Details of the symmetry classification procedure can be found in appendix A.3. From the FGA the theoretical numbers of vibrations belonging to a certain symmetry are known. The difference between these numbers and the calculated ones indicates roughly how far the numerical simulation of the crystal differs from the idealized situation. I developed another means for judging the quality of the simulation and the reliability of the symmetry assignment, described in the appendix A.3. Here it is checked which symmetry is most compatible with a given vibration and the difference between the least and the best fitting symmetry is taken as a quality measure.

Having thus obtained all lattice vibrations with their proper symmetry assignment they could now be compared with the modes experimentally obtained. In the case of the infrared active vibrations it is possible to calculate reflection spectra from the simulation data. Therefore the oscillator strengths of the lattice vibrations are required. The oscillator strength f_i of a mode ν_i is proportional to the squared derivative of the molecule dipole moment $\boldsymbol{P}$ to the mode normal coordinates $\boldsymbol{Q}_i$ of the vibration which can easily be obtained from eigenvectors $\boldsymbol{ve}_{ij}$ and effective charges e_j of the atoms in

the crystal (see e.g. [117]) and thus

$$f_i \propto \left(\frac{\partial \boldsymbol{P}}{\partial \boldsymbol{Q}_i}\right)^2 = \left(\sum_j e_j \boldsymbol{v}\boldsymbol{e}_{ij}\right)^2 . \tag{8.5}$$

With these oscillator strengths, energies and an estimated linewidth, a dielectric function was calculated on basis of an harmonic oscillator model and from that the simulated reflectivity spectra (see [116] and expressions in chapter 6). Raman spectra cannot be simulated that easy, therefore only the observed frequencies were compared with the simulation. However, in contrast to the infrared active vibrations, which had to be compared with reflection spectra where the intensity of the modes can be used as a means to distinguish between overlapping lines, the Raman lines in the high-energy region are well separated by their energy and in the low-energy region have similar intensities anyway.

8.4. Results of the molecular dynamics

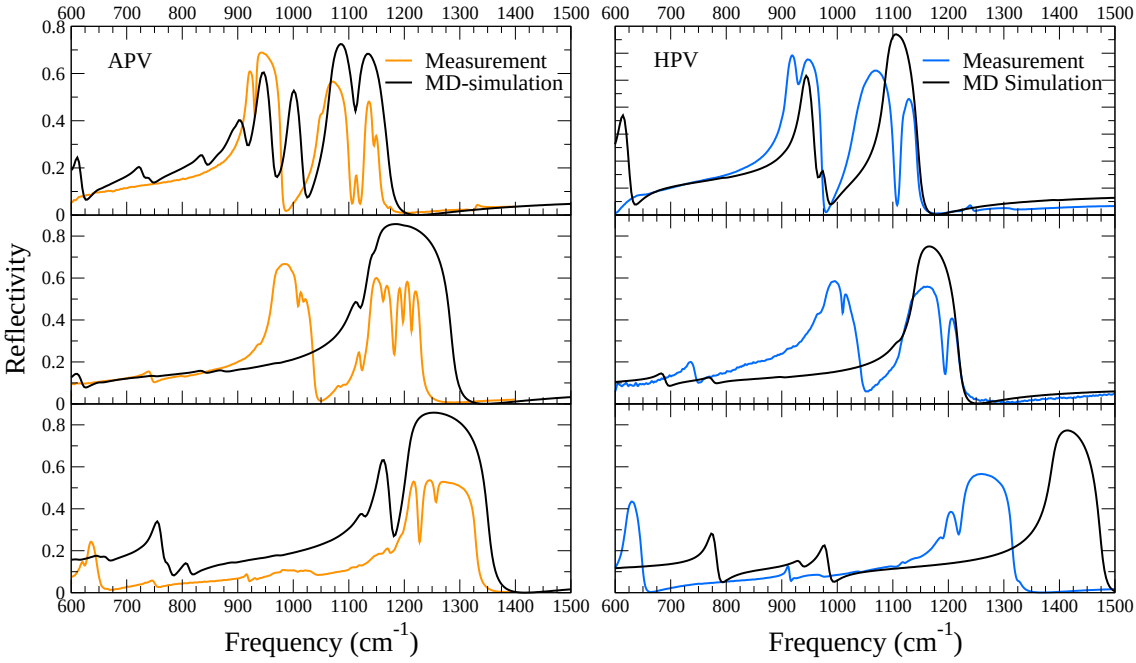

Figure 8.1.: Comparison of observed infrared spectra of APV (left side) and HPV (right side) with calculated spectra from MD-simulation.

Figure 8.1 shows the simulated reflection spectra together with the measured ones for APV and HPV, respectively. Referring to the discussion in chapter 7.1, the overall distribution of the modes in the measured spectra could at large be reproduced by the simulation. In particular the polarization containing the V=O vibration is matching

fairly good. Here the simulated spectra of APV compared to those of HPV shows symmetry splitting as was observed in the experiment. The frequency of the V=O vibration is around 900 cm^{-1} in the simulation whereas it is some 20 cm^{-1} higher in reality. I tried to fit the simulation to observed spectra by adjusting the force constants of the vibrational modes. Due to their mutual interaction this cannot be performed independently and a perfect correspondence could not yet be achieved.

The comparison of the calculated Raman active modes with the observed Raman spectra in Fig. 8.2 shows a similar picture. The distribution of modes is reasonably reproduced by the MD-simulation, even in the low energy region not shown here. The eigenvectors of some selected modes are depicted in appendix A.5.

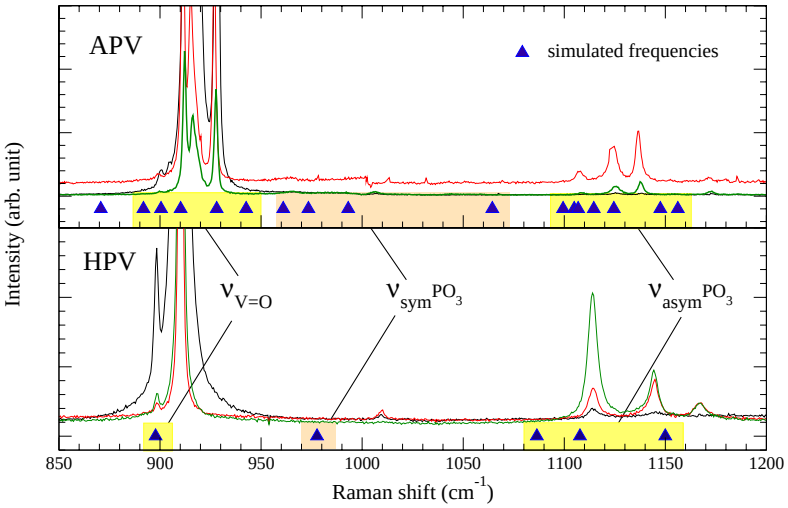

Figure 8.2.: High-energy Raman spectra of VPO in A_1 and A_g symmetry, respectively, together with vibrational frequencies of these symmetries from MD-simulation (triangles). The colored areas mark simulated vibrational modes of a certain type. Note the mode degeneracy in the HPV spectra and calculation.

A closer comparison experiment and MD-simulation reveals some of the weakness of the model applied. In the Raman spectra of APV the total splitting ($\nu_{V=O_{high}} - \nu_{V=O_{low}} \approx 50 cm^{-1}$) of the calculated V=O vibrations is too large compared with the observed frequencies, where the total splitting amounts to 16 cm^{-1}. This is surprising since all bonds of equal type had identical force constants in the FF so that any mode splitting is due only to the crystallographic inequality of the atoms in the simulation cell. In the simulation of APV 5 modes involving V=O vibrations were found instead of 4 predicted by FGA. This is possibly due to an admixture of $\nu_s PO_3$ vibration which can be seen in the simulation which seems to further split one of the modes. However, it is questionable whether this could explain the large total splitting, too. The splitting of the $\nu_{as} PO_3$ vibrations in the HPV spectra is matched rather good. The fact that the simulated IR spectra of this range look different from the measured ones may come from the fact, that as a matter of course the simulation yielded no information about the mode linewidth so that this parameter was chosen arbitrarily.

In some respect the observed IR spectra and the simulated ones differ significantly. The $\nu_{as}PO_3$ mode with the highest frequency is observed in APV and HPV in the spectra polarized along the spin-chains. The simulation of APV represents this very good whereas the very same vibrations in HPV are found more than 100 cm^{-1} above the observed ones. In fact, the HPV simulation reveals a gap in the spectra between 1156 cm^{-1} and 1381 cm^{-1}, these values marking $\nu_{as}PO_3$ vibrations with dipole moment perpendicular and parallel to the spin-chains.

Another point where simulation and observation differ strongly, is a mode around 970 cm^{-1} in polarization perpendicular to the spin chains. The simulated spectra do not reveal any mode in this symmetry with comparable dipole moment,- and in this respect the MD-simulation is in full accordance with the FGA, as I will show now. Since this is the range which is usually assigned to the symmetric PO_3 stretching vibrations, as discussed in the preceding chapter, it seems obvious to assign this mode to a ν_sPO_3. However, the analysis of the vibrations of the isolated P_2O_7 group (see appendix A.4, representations A_1 and B_1 of the point group C_{2V}) reveals that the symmetric terminal stretch vibration has a negligible dipole moment along an axis perpendicular to the P-P axis and it is thus clear that no combination whatsoever of those vibrations in the crystal induces a dipole moment of the observed strength in the *b*-*c*-plane. Therefore it can be excluded that this mode originates in a symmetric PO_3 stretching vibration, and on the basis of the valence force model there seems to be no other explanation for the observed dipole moment.

8.5. Summary

The phonon dynamics of VPO was examined by molecular dynamic calculations based on a valence force field and eigenfrequencies and eigenvectors of the lattice vibrational modes were calculated. By analyzing the simulated eigenvectors with regard to their symmetry infrared spectra could be simulated and the model parameters were adjusted successively in order to match the observed vibrational frequencies. The overall appearance of the IR-spectra and the distribution of Raman modes could thus be reproduced. However, I found that the model chosen is not sufficient to render the full lattice dynamics of VPO. The valence force field is only a coarse approximation of the situation in VPO and cannot render e.g. the splitting of the high-energy modes correctly. As a conclusion of my results a revised approach to the lattice dynamics of VPO by MD-simulation should base on an extended FF as e.g. a valence-shell model.

Nevertheless, when the above results are compared with calculations of lattice modes of e.g. the high-T_c superconductors [115] or NaV_2O_5 [89] and their impressive results, it should be well noted that in these works the calculation had to deal with 7 (Nd_2CuO_4) or 16 atoms (NaV_2O_5) in the unit cell, respectively, compared to the 104 atoms of AP-VPO.

9. Experimental Results II: Spin dynamics

In the preceding chapters the discussion of the rich lattice dynamics in VPO has predominantly been the the subject. However, as outlined in the introductory chapters VPO gained most attention of solid state physicists in the last decade due to its magnetic properties. Initially considered as being the realization of a spin ladder — in fact VPO would have been the first known example of this kind – the decision had already fallen in favor of the spin-chain model when I came to the subject. This was mainly due to the INS study of Garrett *et al.* [74] where antiferromagnetic coupling along the alleged ladder directions could be ruled out and instead strong antiferromagnetic dispersion was observed along the y-axis. This observation clearly established that VPO would be better described as an alternating antiferromagnetic spin-chain (AF-SC) with chains along the y-axis. The lower-boundary energy at $\Delta = 3.1$ meV of this excitation was interpreted as the magnetic zone-center energy gap $\Delta = \Delta_{01}$ of a magnon expected for an alternating AF-spin-chain. In addition a second excitation almost parallel to the one at Δ_{01} meV had been observed at 5.9 meV, which is just below $2\Delta_{01}$. Due to this fact Garret *et al.* suggested that this excitation might be a two-magnon bound state, which had theoretically been predicted for those systems [75], rather than a second magnon branch whose existence is implied by the model of two independent spin chains. Hence Grove *et al.* [104] discussed the results of their Raman scattering study on VPO on the above grounds and since they observed only one excitation at 47 $cm^{-1} \triangleq 5.8$ meV they interpreted it as being a two-magnon bound-state, which could in principle be accessible by Raman scattering. Apart from the observation of an excitation at 5.8 meV they observed a phonon at 123 cm^{-1} exhibiting strong anharmonic behavior at low temperature which they attributed to a coupling to the spin system, – the spin-phonon mode already mentioned before. In this chapter I will present my examinations of this features which on the one hand provided evidence for the model of two independent alternating AF spin-chains thus disproving a bound-state and on the other hand revealed spin-system related effects in the high pressure phase HP-VPO.

9.1. Magnetic excitation in AP-VPO at low temperatures

In their light scattering experiments on VPO Grove *et al.* observed at temperatures below T=75 K a shoulder appearing at 47 cm^{-1} in their spectra. This energy corresponds approximately to $2\Delta_{01}$, twice the energy of the singlet triplet gap, so that either an excitation into the two magnon continuum or the two-magnon bound state suggested by Garret *et al.* could be the origin. The authors stated that no further excitations around 95 cm^{-1} had been observed, which would have been the $2\Delta_{01}$-energy of the second excitation described by Garret *et al.*, and thus inferred that this line would rather

arise from a two-magnon bound state than from excitations of another spin system. Furthermore in their opinion it seems to be very unlikely that the other spin chain would accidentally have a gap energy $\Delta_{01}^{B} \approx 2\Delta_{01}^{A}$ since the crystallographic differences are of order $10^{-3} - 10^{2}$

In Fig. 9.1 the low energy portion of the Raman spectra of VPO at several temperatures is displayed. The Raman measurements of AP-VPO revealed two shoulders

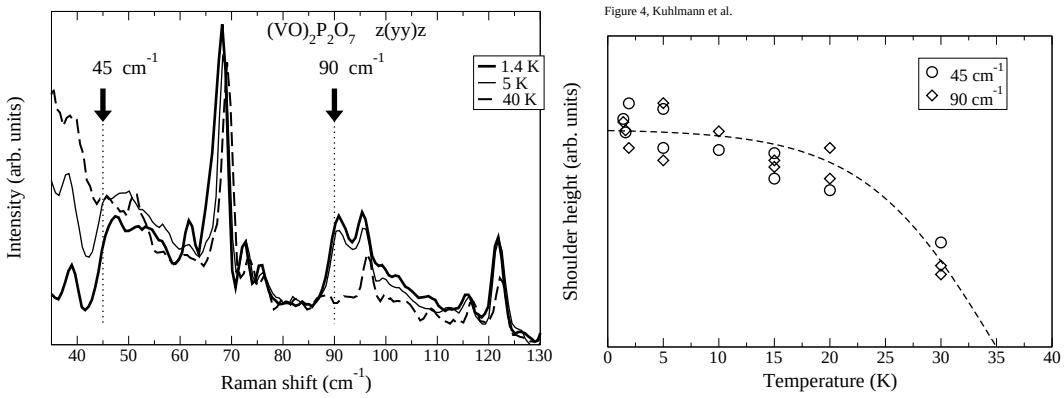

Figure 9.1.: Low-energy Raman spectra of VPO along the chain direction. Two shoulders at 45 and 90 cm^{-1} appear in the spectra at low temperatures

appearing in the spectra at low temperatures at 45 and 90 cm^{-1} with sharply decreasing intensity with rising temperature [118]. Above $\approx$ 30 K the intensity has almost vanished and could no longer be detected. The sharp drop in intensity is in accordance with the data from Ref. [104], however, neither a second temperature range between 30 and 70 K nor the observation of the shoulders in other than the yy-direction could be verified by these measurements.

Both shoulder are almost identical in appearance and temperature dependence so that it seems obvious that they originate from two independent spin-chain systems.

The energies of the observed shoulders are closely below 2Δ of the energies of the excitation branches observed by INS. This raises the question whether the shoulders are related to excitations into the two-magnon continua or are in fact two-magnon bound states, as was proposed for the lower excitation in Ref. [104]. Grove *et al.* examined the shoulder at 45 cm^{-1} by applying a magnetic field and found no splitting of the signal and thus no contradiction to their assumption of a singlet (S=0) bound-state. However, the sum energy required for the simultaneous excitation of two magnons each having a k-vector of q and $-q$, respectively, does not depend on the magnetic field since the energy of a magnon with $E(k = q)$ is altered by the same amount but in opposite direction to that of a magnon with $E(k = -q)$. Thus, from experiments in a magnetic field it is not possible to decide between a singlet bound state or the excitation of two magnons. This question has been addressed in recent calculations of the magnetic properties of VPO based on the model with two independent spin chains. Uhrig and Normand revisited the model they had developed in Ref. [46] and extended it by introducing a second spin-chain plane [52]. A major result of their calculations is that the frustrated

interchain coupling is significantly weaker than in their original model and the authors concluded: "Any bound states of the elementary magnons can be expected to be, at best, only very weakly bound, and, in addition, to have very low weight."[52]. This opinion is further supported by recent calculations [33] (see Fig. 2.8) of the magnon spectral weight which demonstrate that for low frustration the spectral weight is dominated by the two-magnon continuum. I will therefore attach to the conclusion of Uhrig and Normand and interpret the observed shoulders as excitations into the two-magnon continua of two independent spin-chain systems. As to why the gap energies are related as 2:1 despite the small crystallographic differences Uhrig and Normand stressed that the dominant superexchange path is mediated by the PO_4 group and that "... the interaction magnitude is well known to have a very strong dependence on both interatomic spacings and bond angles."

9.2. Spin-phonon coupling in AP-VPO

Besides the observation of excitations into the spin system another feature was reported in Ref. [104], which has to be attributed to the magnetic properties AP-VPO. A phonon line observed at 123 cm^{-1} at 5 K in (chain-pol) shows a strong energy renormalization with increasing temperature. This is depicted in Fig. 9.2. The mode appears in (xx) and (zz) polarization, i.e. perpendicular to the spin-chains. The peak energy is shifting towards lower values with increasing temperature but the integrated intensity is conserved. In contrast to that is the behavior of two weak peaks which appear in (yy) at 123 and 132.5 cm^{-1}. Their integrated intensity is seemingly not conserved and they thus remind to the modes which have been mentioned already above (see Fig. 7.6).

It should be noted that these measurements differ from the results of Grove *et al.* with regard to the assignment of the crystal axis. Whereas I found the anharmonicity of the 123 cm^{-1} mode only in polarization perpendicular to the chains Grove reported them to have (bb) or (cc) polarization. However, from comparison of the spectra I suppose that in their work the crystal axis have been inadvertently interchanged. Then the mode at 123 cm^{-1} in (aa) polarization which they reported to disappear at higher temperatures is identical with the mode shown in Fig. 9.2 in (bb) polarization. But this does not dissolve all discrepancies. Grove claimed to observe the singlet bound-state in (aa) and (bb) whereas I found it to have (bb) in-chain polarization only. Rather than having simply interchanged the crystal axis their observations indicate to my opinion towards the possibility of having examined a twinned crystal so that the same feature could appear in two polarizations.

I will discuss now the strongly renormalizing phonon at 123 cm^{-1}. The energy of this phonon lies close to the upper boundary of the magnon dispersion ($\approx$ 125 cm^{-1}[74]) so that an interaction with the spin system is possible. Grove assigned the phonon at 123 cm^{-1} to vibration of the PO_4 plaquette from a comparison to similar compounds. I have shown in the preceding chapter (md) that there are some possible candidates for a vibration of that kind where the essential feature is the alteration of bond angles along the superexchange

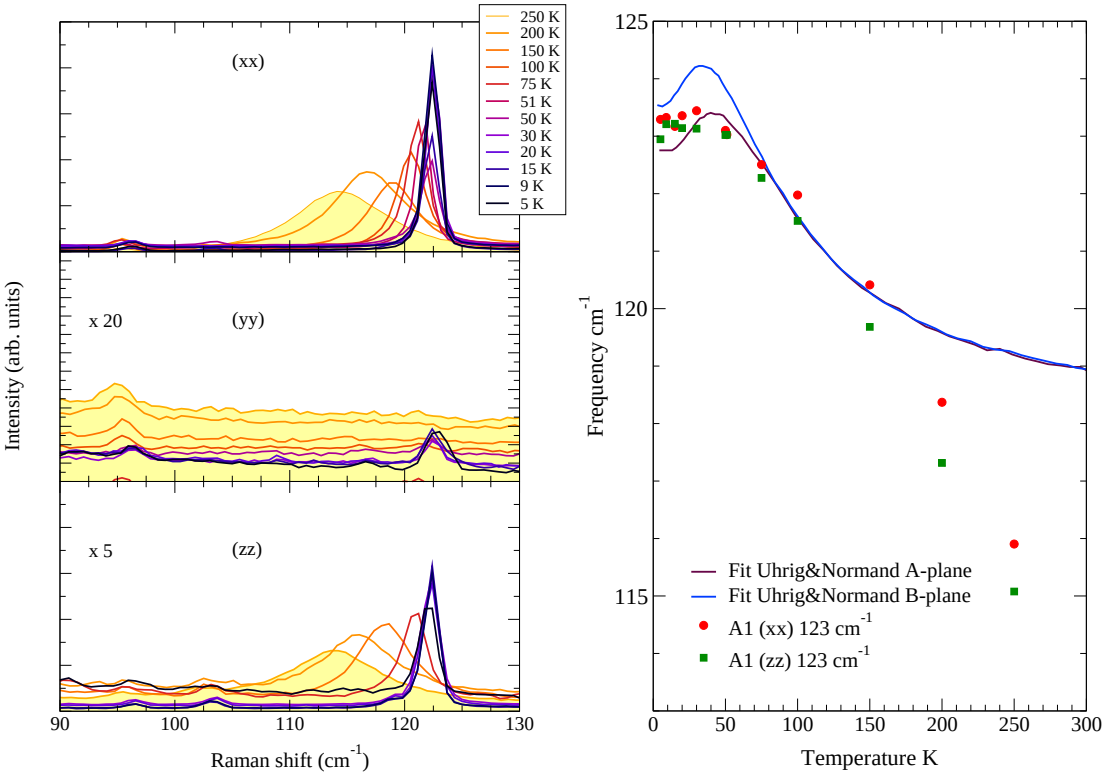

Figure 9.2.: (left) The spin-phonon mode of AP-VPO at 123 cm^{-1} in A1 symmetry. (right) The mode shift compared to calculations of Ref. [52]. Above 150 K the fitting function deviates from the observation, the residual shift has to be attributed to lattice anharmonicity.

path and which therefore modulates strongly the J_1/J_2 ratio. In the work of Uhrig and Normand [52] this has been chosen as a starting point for the modelling of the spin-phonon coupling. They assumed a coupling of a nondispersive Einstein mode with frequency ω_0 to the dominant exchange parameters J_1^A, J_1^B and computed corrections for the energy of the magnon system as well as to the phonon by applying continuous unitary transformations to diagonalize the spin-phonon hamiltonian. The result of their calculations is displayed in Fig. 9.2 together with the experimental shifts obtained from my measurements. Up to $\approx$ 150 K the data is represented well by the calculations. There is a small upshift predicted around 35 K, which would not be expected from lattice anharmonicity which could be confirmed by my measurements. However, it is not as pronounced as it appears in the calculations. It is noteworthy that the spin-phonon coupling constant of G=6.6 meV which was used in the calculations was found to be considerably larger than in $CuGeO_3$, the prototypical spin-Peierls compound. Below $\approx$ 70 K a splitting of roughly 1 cm^{-1} is predicted for a coupling of the phonon to the nonequivalent planes of spin chains assuming the same coupling strength. This could not be observed, possibly because the linewidth of the phonon (about 2 cm^{-1}) is too large.

Above ≈ 150 K the calculated shift deviates from the experimentally observed shift and has a tendency to saturate. Rather than spin-phonon coupling lattice effects may account for the large shift of this mode in the range from 150-300 K. The reported strong shift under hydrostatic pressure, which has been discussed above (7.3.2), supports this picture as well as measurements of sound velocity e.g. on AP-VPO. Summarizing, I would like to point out the conclusions a bit more: what in the beginning has been seen as a clear signature of spin-phonon coupling, i.e. the strong shift of the mode, has in fact to be attributed mainly to the unusual phonon dynamics whereas it is the small deviation from lattice anharmonicity at low temperature that spin-phonon coupling is responsible for.

An important consequence of the calculations of Uhrig and Normand (loc.cit) which has yet to be confirmed experimentally is a renormalization of the magnon energies due to the large spin-phonon interaction. The magnon renormalization leads to a flattening of the magnon dispersion with increasing temperature, see Fig. 2.11 in chapter 2.4. It will be discussed in the next section which effect this flattening may have on other phonons, if we transfer the Uhrig-model to HP-VPO.

9.3. Spin-phonon coupling in HP-VPO

9.3.1. Temperature dependence

I have shown in the preceding chapters that the crystallographic similarity of AP- and HP-VPO leads to very similar phonon spectra. When single crystals of HP-VPO became available the expectation was to observe similar magnon related effects in the Raman spectra or even the observation of spin gap related scattering. Because of the smaller unit cell there should exist only one spin-chain system with a single spin gap. First measurements of the magnetic susceptibility and with high field magnetization by Azuma *et al.* [65] and Saito *et al.* [119] and calculations based upon their data [120] had pointed towards a gap energy of ≈ 33 K $\hat{=}$ 2Δ=46 cm^{-1},- a value comparable to that of the lower gap in AP-VPO. However, no gap related scattering could be observed above 30 cm^{-1}, which was the lower boundary of the useful energy range to which Raman measurements were restricted due to the sample quality. Subsequent measurements which compared AP-VPO and HP-VPO demonstrated that the spin gap of the HP-phase is more likely of the size of 22 K [80] corresponding to 2Δ= 30.6 cm^{-1}, which would explain the missing gap in the Raman spectra above 30 cm^{-1}.

Whereas the direct observation of the spin gaps by Raman scattering seems to be hindered by the sample quality I expected to observe a mode similar to the spin-phonon mode in AP-VPO. Instead a very different picture was revealed by the measurements [121]. In Figure 9.3 the low energy portion of the raman spectra in xx and zz polarization are shown. Several phonons show asymmetric lineshapes of Fano-type and strong broadening at lowest temperatures but regain the usual lineshape at higher temperatures. On a first impression this behavior seems to be opposed to that of the SP-mode in AP-VPO where renormalizing effects increase at higher temperature. A Fano-type lineshape indicates an interaction of a discrete excitation with a background continuum

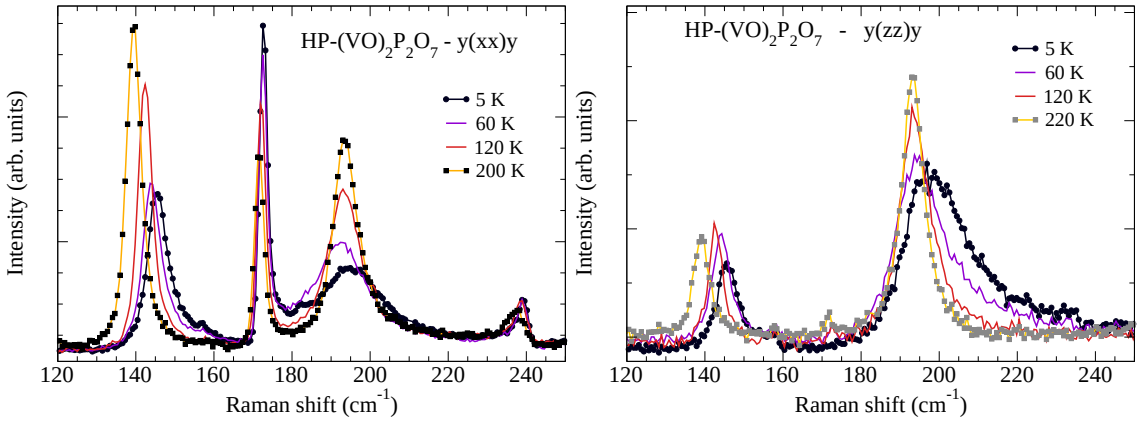

Figure 9.3.: Raman spectra of HP-VPO in the low-energy region with Fano-lines.

of states. This universal phenomenon was first analyzed by U. Fano [122] to describe asymmetrical lineshapes occurring in the autoionization spectra of He. It is the result of a quantum mechanical interference between the transition paths into the discrete states and into the continuum of states. The main characteristic of the resulting lineshape is an increase of intensity on one side of the discrete level and a suppression of intensity below the continuum level on the other side. The lineshape can be parametrized in the form [123]:

$$f(\omega) \propto \frac{\pi\varrho(V + (\omega - \omega_p))^2}{(\pi\varrho V^2)^2 + (\omega - \omega_p)^2} \tag{9.1}$$

where ω_p is the energy of the uncoupled phonon, ϱ represents the density of states (DOS) of the background continuum and V is the interaction potential between these excitations. The Fano-profile is frequently parametrized with a lineshape parameter q and the linewidth Γ, which are related to the V and ϱ as $V \propto q\Gamma$ and $\varrho \propto 1/\Gamma q^2$.
With regard to a possible magnon renormalization as proposed for AP-VPO [52] V was kept constant at its 5 K-value. The results for the ratio of the DOS to the value at 5 K are displayed in Fig. 9.4 (top) for the mode at 145 cm^{-1} and the mode at 195 cm^{-1}. The fit to the mode at 195 cm^{-1} shows a decrease in the DOS of the background continuum. The 145 cm^{-1} mode follows this behavior at low temperatures but above 100 K shows an increasing DOS. The difference of both modes is underlined by comparing the bare phonon frequencies obtained from the fit (Fig. 9.4 (bottom)).

For the mode at 195 cm^{-1} there is only little variation of the phonon energy as one would expect from the usual temperature-dependent lattice anharmonicities. The mode at 145 cm^{-1} on the other hand shifts by more than 8 % from 5 K to 300 K to lower energies. For this mode I have concluded in chapter 7.3.2 from their similar pressure shifts that it is most likely the counterpart of the SP-mode in AP-VPO. This is further supported here by the observed energy shift as a function of temperature, which is almost the same for both modes. However, both modes differ strongly in one respect. The spin-phonon mode in AP-$(VO)_2P_2O_7$ shows a considerable broadening with rising

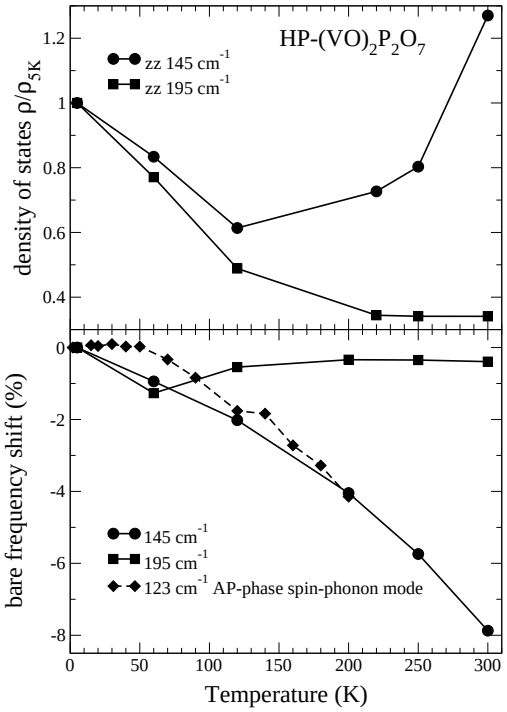

Figure 9.4.: Lineshape parameters of the fano-modes in HP-VPO. (top) Density of states $\varrho/\varrho_{5\mathrm{K}}$. (bottom) Energy shift of the uncoupled phonon. The energy shift of the HP-phonon at 145 cm^{-1} shows little decrease of the background DOS and follows the shift of the AP-spin-phonon mode thus underlining their common origin. The HP-mode at 195 cm^{-1} shows a strong decrease in the background DOS.

temperature whereas in HP-$(VO)_2P_2O_7$ the inverse takes place: The linewidth decreases with rising temperature indicating an increasing interaction towards lower temperatures.

The observations can be summarized as follows I) both modes show an interaction with a background continuum of states and an increase of the DOS of the background continuum at low temperatures. II) Both modes, however, differ in their respective response to the change in DOS, and the energy of the phonon at 145 cm^{-1} behaves more like that of its counterpart, the spin-phonon mode in AP-$(VO)_2P_2O_7$. III) The lineshape temperature dependence of the 145 cm^{-1} mode is opposite to its AP-counterpart. Since an interaction with an electronic background is excluded, $(VO)_2P_2O_7$ is clearly an isolating compound, the observed background continuum can be assigned to the two-magnon continuum of the AF spin-chains.

I will now discuss the results in relation to the spin-phonon mechanism in AP-$(VO)_2P_2O_7$ as proposed in Ref. [52]. Uhrig and Normand explained the modeshift of the spin-phonon mode in AP-$(VO)_2P_2O_7$ by a renormalization of the magnon dispersion, which they show to be a band flattening with rising temperature. It is easy to show that this band flattening leads to an increase of the DOS within the bands under the assumption of the conservation of the total number of states. A similar magnon renormalization in HP-$(VO)_2P_2O_7$ would therefore lead to an increase in the DOS in an energy range between the magnon dispersion boundaries. Phonons in that energy range should thus show an increasing Fano asymmetry as a function of temperature. Since the opposite was observed I conclude that either the phonon at 195 cm^{-1} lies outside the energy range of the magnon dispersion at high temperatures or the mechanism proposed by Uhrig and Normand cannot be transferred directly to HP-$(VO)_2P_2O_7$. In particular the unusual

behavior of the 145 cm^{-1} mode at temperatures above 100 K needs more theoretical consideration.

9.3.2. Pressure dependence

In the previous chapter on phonon dynamics (7.3.2) I have shown that the SPP-modes in both phases of VPO revealed a strong dependence on hydrostatic pressure applied at room temperature. However, the effects of a possible spin-phonon coupling in HP-VPO can only be observed at temperatures below ≈ 60 K. Therefore in order to study the effect of hydrostatic pressure on the spin-phonon coupling the measurement of the pressure dependence had to be performed within a He bath cryostat. Details on how measurements at low temperature under high hydrostatic pressure were performed have already been described in 3.2. The result of this measurement is summarized in Fig.9.5. Since the small crystal fragments used for this experiments could not be oriented within the diamond anvil cell after loading, it was necessary to examine several loadings until the orientation of the crystallites had at least approximately the wanted orientation. The crystallite in the spectra presented below seems to be aligned with some inclination to the crystal axes thus only the fano mode around 195 cm^{-1} can be observed and not the A_g mode at 145 cm^{-1}. At 5 K and not too high hydrostatic pressure, the mode

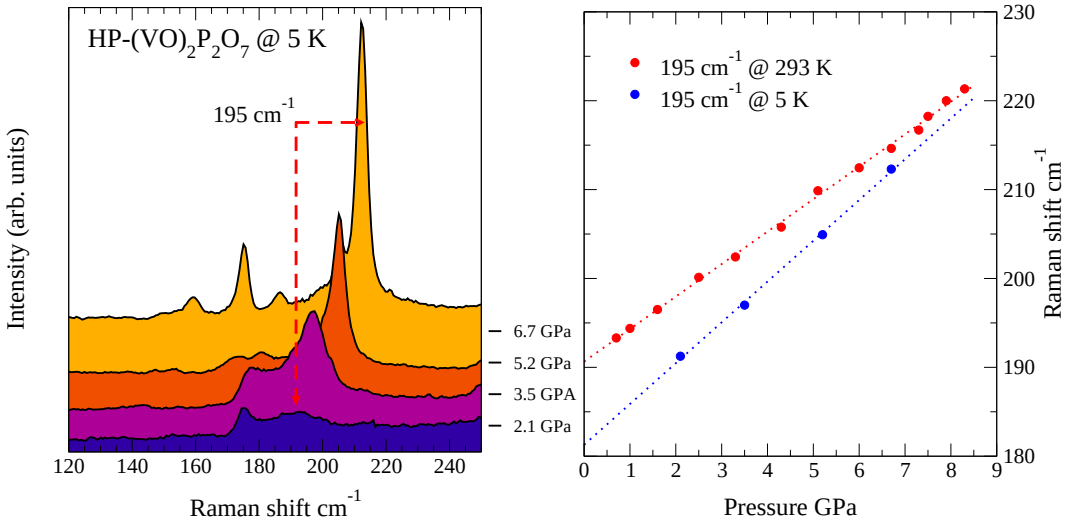

Figure 9.5.: (left) Raman spectra of HP-VPO at 5 K and different hydrostatic pressure. (right) Pressure induced shift of the phonon at 195 cm^{-1} at 293 and 5 K. Linear fits to the data are given as guidelines. The data at room temperature had been obtained by fitting Fano lineshapes to the spectra and therefore represent the bare frequencies whereas the data at 5 K are fits by Lorentzian peaks. Thus the deviation of the curves at low temperature is due to the spin-phonon coupling, which otherwise would have similar slopes.

at 195 cm^{-1} is strongly broadened, comparable to the measurement displayed in Fig. 9.3. With increasing pressure the mode shifts to higher energy and simultaneously

develops a "normal" lineshape together with an increased intensity. Apparently the interference of this phonon with the background continuum, responsible for the Fano-lineshape, can be switched off by applying hydrostatic pressure. The pure mode shift of this phonon is at 5 K of the same size as it is at room temperature (Fig. 9.5 right side). As was already discussed on the above, the appearance of the Fano effect depends on two ingredients in addition to a phonon ω_0,- the presence of a background continuum represented by a DOS ϱ together with an interaction potential V between the competing excitations ω_0 and ω_ϱ. Therefore a change in the Fano-lineshape may occur either by a change in the background-DOS or in the interaction potential V. Since the phonon energy ω_0 of the phonon at 195 cm^{-1} is a function of energy, a possible explanation of the vanishing Fano-lineshape could be that ω_0 moves out of the energy range of the background continuum so that the phonon "sees" a changing DOS rather than experiencing a changing V. This would imply an upper boundary for the background spin continuum located approximately around 200 cm^{-1}. Up to now no data for the magnon dispersion of HP-VPO is available so that this value can still not be verified by other experiments. However, with regard to the upper (two-)magnon boundary in AP-VPO at $\approx$ 240 cm^{-1} [74] this value seems to be of reasonable size.

9.4. Summary

The Raman measurements at low temperatures and/or high hydrostatic pressure on AP-VPO and HP-VPO revealed several findings. First, the observation of a second shoulder at 90 cm^{-1} in the low temperature spectra of AP-VPO produced strong evidence for the model of two independent spin-chains. It is meanwhile the established model for AP-VPO and was successfully applied e.g. in the calculations of spin-phonon coupling by Uhrig and Normand [52]. The scattering intensity of the two spin-gaps is in accordance with calculations of the magnon spectral weight of Schmidt *et al.* [33] for low frustration α. This was assumed in the calculations of Ref. [52], too. The spin-phonon mode in AP-VPO at 123 cm^{-1} has been revisited and, with the information from Chapter 7 concerning the counterpart of this mode in HP-VPO at 145 cm^{-1}, it was found that most of the observed mode shift has to be attributed to the large anharmonicity of these modes.

In HP-VPO the low temperature measurements revealed some modes showing a Fano-lineshape, which indicates a coupling to a background continuum of states,- most likely the magnon continuum. The coupling decreases with increased temperature, and this behavior is different from the spin-phonon mode in AP-VPO, where the coupling is assumed to be constant. The conclusion which can be drawn from the observations is that the Uhrig/Normand model of spin phonon coupling in AP-VPO cannot be transferred to HP-VPO without modifications.

The measurements at various temperatures have shown that the HP-phonon at 195 cm^{-1} is apparently affected by a changing DOS of the background continuum. The measurement under high pressure confirms this observation. Whereas this mode shows a Fano-lineshape at low temperatures, an increased pressure, at constant temperature,

is apparently lifting the influence of the background DOS and the mode returns to a symmetric lineshape, accompanied by a positive energy shift. Two scenarios can be responsible for the observed behavior. First, by applying pressure the mode may shift out of the range of the background DOS. This would fix its higher boundary somewhat around 200 cm^{-1}, as already concluded from the temperature dependence of the mode. Or, second, the lattice is strained such that the magnon dispersion itself is altered by the pressure.

10. Summary

The electronically one-dimensional transition metal compound $(VO)_2P_2O_7$ (VPO) was studied by means of Raman and infrared spectroscopy. Under normal conditions VPO crystallizes into the orthorhombic phase AP-VPO (space group $Pca2_1$) and changes under high-pressure and high-temperature conditions into the orthorhombic phase HP-VPO (space group Pbcn). Samples of both modifications were examined. The Raman measurements were performed at temperatures of 2-300 K. Additionally, Raman spectroscopy was carried out under high hydrostatic pressure up to $\approx$ 8 GPa by using a diamond anvil cell. These measurements were performed at low temperatures, too. The polarized infrared spectra were taken at room temperature within a spectral range of 200-2000 cm^{-1}.

Initially AP-VPO had been considered as being a prototypical spin ladders compound, based on the crystal structure and the arrangement of the spin carrying V^{4+} ions, but subsequent research, in particular INS measurements of Garrett and coworkers proved that AP-VPO has instead to be described by an alternating antiferromagnetic Heisenberg spin-chain model. The INS measurements revealed a second excitation in the magnon dispersion whose origin was not clear and was tentatively attributed to a singlet bound state, which had been predicted for frustrated spin chains. The observation of only one mode in first Raman measurements at 45 cm^{-1} seemed to confirm this proposition. By recognizing the true crystal symmetry of AP-VPO, however, another explanation for the second mode was put forward. The V^{4+} ions occupy four nonequal sites in the crystal and every two of them belong to one spin-chain, so that in fact two independent spin systems exist in AP-VPO, thus providing a straightforward explanation of the second mode.

The structure of the higher symmetric phase HP-VPO is very similar to AP-VPO. The main difference between the phases is the degeneracy of the two nonequivalent spin-chains of AP-VPO to one spin-chain in HP-VPO. Susceptibility and magnetic high-field measurements consequently proved the existence of a single alternating antiferromagnetic Heisenberg chain in HP-VPO with a singlet-triplet gap of $\approx$ 30 cm^{-1}.

The main objective of the thesis has been the comparison of the two phases in respect to the phonon spectrum, the magnetic excitations of the spin-chains and a coupling of phonons to the spin system, which had already been observed to be strong in AP-VPO. As a preparatory work I performed a full factor group analysis (FGA) of the phonons in VPO where I elaborated how vibrations of isolated molecular groups correlate to vibration in the crystal lattice. With this information I could precisely predicted how often a certain type of vibration would occur in the spectra and how AP-VPO and HP-VPO would differ in this respect.

The results from the FGA were compared with the Raman and infrared spectra and

most of the observed lines could be assigned to lattice eigenmodes. The predicted mode degeneracy in HP-VPO compared to AP-VPO was verified. One example are the prominent VO stretching vibrations at 915 cm^{-1}, where four lines in AP-VPO degenerate to one line in HP-VPO. These lines were examined more closely because of the unusual anharmonicity they exhibit. Instead of softening with increased sample temperature, as usually observed with lattice vibrations, these modes show a shift to higher energy. An explanation was given based on an increased interlayer interaction between adjacent VO-groups along the crystallographic *a*-axis. From the frequency shift a thermal expansion coefficient of $\alpha_a \approx 3 \cdot 10^{-5} K^{-1}$ was concluded, indicating towards a rather anisotropic lattice expansion. This could be verified by a temperature dependent X-ray diffraction study on AP-VPO which I had suggested.

A further insight into the lattice dynamics of VPO was attempted by a molecular dynamics simulation of the lattice vibrations. Starting from a valence force field the energies and the eigenvectors of AP-VPO and HP-VPO were calculated and classified according to their symmetry. The zone-center phonon spectra of VPO could thus be reproduced by the simulation. In respect of number and symmetry of the modes the achieved accordance was very good. The distribution of the modes with energy was only approximative, as was shown by comparison of simulated infrared spectra with the experimental ones. The applied force-field was found to be incomplete, concluding from the fact that certain modes with high dipole moment could not be reproduced.

The Raman measurements on AP-VPO at low temperatures revealed a second shoulder in the spectra at 90 cm^{-1} similar to the known one at 45 cm^{-1}. This observation is a strong evidence in favor to the model of two independent spin-chains in AP-VPO, which in the meantime is commonly accepted. A similar structure, expected around 30 cm^{-1} and originating from a single spin-chain, could not be observed in HP-VPO. Two reasons might be responsible for that: 1. the sample quality was not as perfect as needed for Raman measurements at very low (< 30 cm^{-1}) wavenumbers and 2. the scattering intensity, already very weak in AP-VPO is probably much lower in HP-VPO. This could indicate that the magnon dispersion in HP-VPO is more flat, but that conclusion could only be proved by INS measurements.

The spin-phonon mode in AP-VPO at 123 cm^{-1} was examined closely and the pressure dependence of this mode was determined. The unusual large pressure shift of this mode allowed to identify a mode with similar pressure shift in the HP-VPO spectra, which is most likely a vibration of same type. If both modes are of similar type then spin-phonon coupling should affect both modes in a similar manner. The measurements revealed a different picture. Whereas the spin-phonon mode in AP-VPO broadens considerably with increased temperature, hereby conserving the integrated intensity its HP-VPO analogue sharpens at higher temperatures, although showing a similar energy shift. This observation indicates that, although most likely a coupling of the spin-system to the modes is responsible for the observed behavior, the coupling *mechanism* is apparently very different. The observation of further modes in HP-VPO which show a broadened Fano-lineshape at low temperatures and a normal lineshape at room temperature adds to that picture. Some conclusions of this observations were discussed, the main one is certainly that the model for the spin-phonon coupling in AP-VPO developed by Uhrig

and Normand cannot be transferred to HP-VPO without modifications. The up to now unexplained strong and — compared with AP-VPO — unusual spin-phonon coupling of HP-VPO has recently been the topic of a talk given by Wolf [124] on thermodynamical and magnetoelastical investigations on HP-VPO. The unusual strong effects they observed, which seem to indicate in the same direction as my observations led the authors to raise doubt of HP-VPO being a dimerized Heisenberg chain. A profound INS study on HP-VPO would be very desirable to clear up this puzzle.

A. Appendix

A.1. Synopsis of crystal axis assignment by different authors

Reading literature about VPO can sometimes be confusing due to the fact that different crystal symmetries are being used depending to which structure determination the respective authors refer, so that e.g. the *b*-axis in AP-VPO of one author will be referred to as the *c*-axis of another one, which, even more confusing, corresponds to the *a*- or *c*-axis in HP-VPO. To facilitate the discussion I therefore compiled the table below where the axis denotations are juxtaposed together with a sketch of the crystal structure of VPO in Fig. A.1. The structure of HP-VPO was given by Azuma *et al.* in the nonstandard setting Pnab of the 60. space group, but for the MD I applied the standard setting Pbcn, therefore both are listed.

Table A.1.: Crystal axis denotations of VPO by different authors.

Compound	AP-VPO		HP-VPO	
Author	Nguyen [69]	Bayreuth [70]	Azuma [65]	standard setting
symmetry	$P2_1$	$Pca2_1$	Pnab	Pbcn
POP-*bridge*	a	a	a	c
PO_3-*link*	c	b	b	b
chain	b	c	c	a

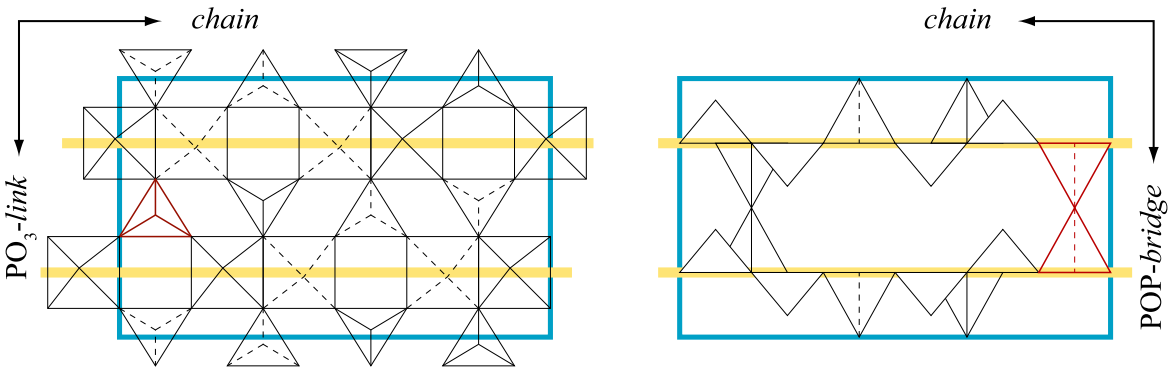

Figure A.1.: Schematic structure of AP-VPO with axis denotations referring to table A.1. The crystal axis in HP-VPO are denotes likewise.

A.2. Character tables

Character tables for the point groups C_{2v} and D_{2h} of the space groups $Pca2_1$ (AP-VPO) and Pbcn (HP-VPO), respectively.

Table A.2.: C_{2v}

C_{2v}	E	C_2(z)	σ_v(xz)	σ_v(yz)	IR − activity	Raman activity
A_1	1	1	1	1	z	x^2, y^2, z^2
A_2	1	1	-1	-1		xy
B_1	1	-1	1	-1	x	xz
B_2	1	-1	-1	1	y	yz

Table A.3.: D_{2h}

D_{2h}	E	C_2(z)	C_2(y)	C_2(x)	i	σ(xy)	σ(xz)	σ(yz)	IR-activity	Raman activity
A_g	1	1	1	1	1	1	1	1	-	x^2, y^2, z^2
B_{1g}	1	1	-1	-1	1	1	-1	-1	-	xy
B_{2g}	1	-1	1	-1	1	-1	1	-1	-	xz
B_{3g}	1	-1	-1	1	1	-1	-1	1	-	yz
A_u	1	1	1	1	-1	-1	-1	-1	-	-
B_{1u}	1	1	-1	-1	-1	-1	1	1	z	-
B_{2u}	1	-1	1	-1	-1	1	-1	1	y	-
B_{3u}	1	-1	-1	1	-1	1	1	-1	x	-

A.3. Determination of normal mode symmetry of computed eigenvectors

With the normal mode frequencies i.e. the eigenvalues of the dynamical matrix given it is a straightforward and routinely performed task to calculate the corresponding eigenvectors. In compounds with a large unit cell and a low symmetry such as $(VO)_2P_2O_7$ the eigenvectors form complicated patterns of moving atoms which cannot easily be classified into point group symmetry just by visual inspection. I developed therefore an algorithmic way to calculate the symmetries of the Γ-point modes by a computer program, which is outlined in the following.

Let $\boldsymbol{G}$ be the space group of the crystal under consideration and $\boldsymbol{R}$ be the point group which is isomorph to the factor group $\boldsymbol{G}/T$ of the crystal, i.e. its crystallographic point group. The group $\boldsymbol{R}$ has the irreducible representation $\Gamma = \sum_i m_i \Gamma_i$ (m_i multiplicity of rep. Γ_i), and each eigenvector $\boldsymbol{ve}_i$ is said to belong to one of the Γ_i, all $\boldsymbol{ve}_i$ forming itself an representation of $\boldsymbol{R}$. Evidently the representations obey the symmetry operations $\boldsymbol{S}_j$

of $\boldsymbol{R}$, that is if we transform the eigenvector $\boldsymbol{ve}_{ik}$ belonging to the Γ_i representation attached to the unit cell atoms $\boldsymbol{a}_k$ according to the symmetry operation $\boldsymbol{S}_j$ we may write

$$V_{ik} = \boldsymbol{S}_j(\sum_k(\boldsymbol{a}_k + \chi_{ij}\boldsymbol{ve}_{ik})) - \sum_k(a_k + \boldsymbol{ve}_{ik}) \equiv 0 \tag{A.1}$$

Here χ_{ij} denotes the character of the symmetry operation $\boldsymbol{S}_j$ in the representation Γ_i. Hence in order to determine to which representation a given eigenvector belongs, the validity of the above equation has to be checked for each representation with all symmetry operations $\boldsymbol{S}_j$ of $\boldsymbol{R}$, thus

$$V_i = \sum_k V_{ik} \equiv 0. \tag{A.2}$$

However, this equation is not expected to hold exactly since the eigenvectors come out of a numerical and therefore slightly inaccurate calculation. Instead, for a given eigenvector $\boldsymbol{ve}$ we check for which representation V_i is a minimum and assign that Γ to $\boldsymbol{ve}$. With the comparison of the maxima and minima we have a means to qualify the above assignment and take

$$Q = \frac{V_{i,max} - V_{i,min}}{V_{i,max}} \tag{A.3}$$

as the measure of quality. Thus $Q \approx 1$ would mean a satisfactory assignment whereas lower Q leaves increasing doubt on the assignment. In other words, a very low Q-value means that the vibration in question is more or less compatible with all symmetries.
While the above procedure works well with the one-dimensional representations, the higher-dimensional representations cannot be handled so easily, since here any linear combination of a set of basis eigenvectors is an eigenvector, too. The program was designed to be extensible for calculations with all space groups, however, the implementation is currently restricted to the orthorhombic space groups of $(VO)_2P_2O_7$.

A.4. Vibrations of an isolated pyrophosphate group (P_2O_7)

Table A.4.: Schematic depiction of the bond stretching vibrations of the free P_2O_7 molecule, yellow: Phosphorus and red: Oxygen.

$\mathbf{A}_1$	$\mathbf{A}_2$	$\mathbf{B}_1$	$\mathbf{B}_2$
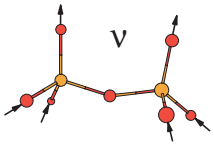	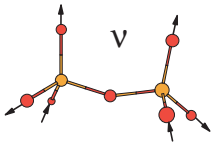	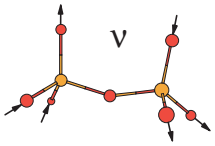	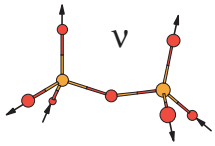
$\nu_{as}PO_3$	$\nu_{as}PO_3$	$\nu_{as}PO_3$	$\nu_{as}PO_3$
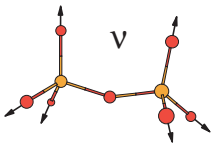		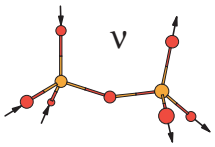	
ν_sPO_3		ν_sPO_3	
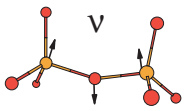		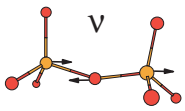	
ν_sPOP		$\nu_{as}POP$	

Table A.5.: Schematic depiction of the bond bending vibrations of the free P_2O_7 molecule, yellow: Phosphorus and red: Oxygen.

$\mathbf{A}_1$	$\mathbf{A}_2$	$\mathbf{B}_1$	$\mathbf{B}_2$
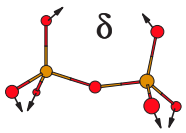	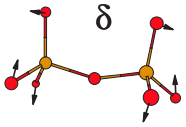	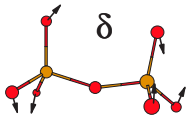	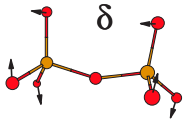
$\delta_{as}PO_3$	$\delta_{as}PO_3$	$\delta_{as}PO_3$	$\delta_{as}PO_3$
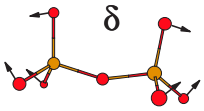		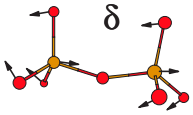	
δ_sPO_3		δ_sPO_3	
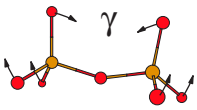	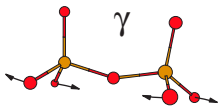	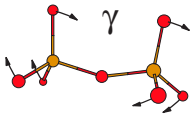	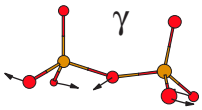
γPO_3	γPO_3	γPO_3	γPO_3
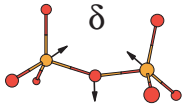	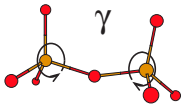		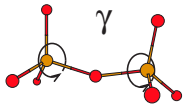
δ_sPOP	$\gamma_{rot}PO_3$		$\gamma_{rot}PO_3$

A.5. Selected eigenmodes of HP-VPO

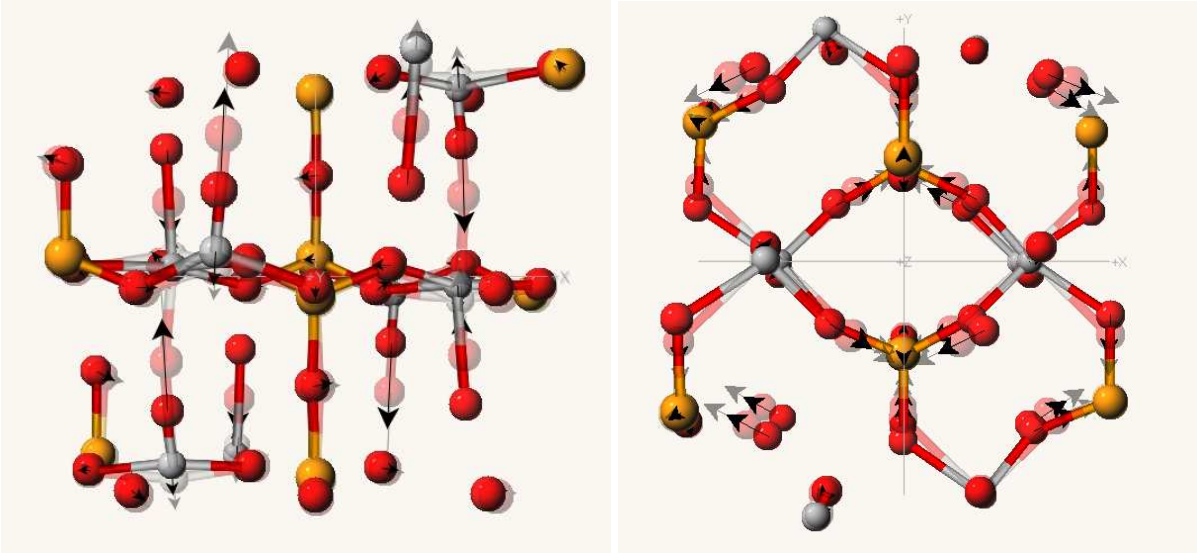

Figure A.2.: Two high-frequency vibrations of HP-VPO in Ag symmetry. V-atoms grey, P-atoms yellow and O-atoms red. (left) The total symmetric VO stretching vibration responsible for the peak at 911 cm^{-1}. (right) A symmetric stretching vibration of the PO_3 groups.

Bibliography

[1] D. C. Johnston, J. W. Johnson, D. P. Goshorn, and A. J. Jacobson, "Magnetic susceptibility of $(VO)_2P_2O_7$: A one dimensional spin-1/2 Heisenberg antiferromagnet with a ladder spin configuration and a singlet ground state," *Phys. Rev. B* **35** (1987) 219. 3, 31

[2] M. H. and R. W. Mayer, A. K.-G. and H. Bluhm and E. Kleimenov and A. Liskowski, D. Su, . Follath, F. G. Requejo, D. F. Ogletree, M. Salmeron, J. A. Lopez-Sanchez, J. K. Bartley, G. J. Hutchings, and R. Schlögl, "In situ investigation of the nature of the active surface of a vanadyl pyrophosphate catalyst during *n*-butane oxidation to maleic anhydride," *J. Phys. Chem. B* **107** (2003) 4587. 3

[3] N. W. Ashcroft and N. D. Mermin, *Solid State Physics*. Holt-Saunders, Philadelphia, 1976. 5

[4] W. Heisenberg, "Mehrkörperproblem und Resonanz in der Quantenmechanik," *Z. Phy.* **38** (1926) 411. 5

[5] P. A. M. Dirac, "On the theory of quantum mechanics," *Proc. Roy. Soc.* **112** (1926) 661. 5

[6] G. E. Uhlenbeck and S. Goudsmit, "Ersetzung der Hypothese vom unmechanischem Zwang durch eine Forderung bezüglich des inneren Verhaltens jedes einzelnen Leuchtelektrons," *Naturwiss.* **13** (1925) 953. 5

[7] K. Yosida, *Theory of Magnetism*, vol. 122 of *Springer Series in Solid-State Sciences*. Springer Verlag, Berlin, 1996. 6

[8] H. A. Kramers, "L' interaction entre les atomes magnétogenès dans un cristal paramagnétique," *Physica* **A I.1** (1934) 182. 6

[9] P. W. Anderson, "Antiferromagnetism. theory of superexchange interaction," *Phys. Rev.* **79** (1950) 350. 6

[10] R. M. White, *Quantum Theory of Magnetism*, vol. 32 of *Springer Series in Solid-State Sciences*. Springer Verlag, Berlin, 1983. 7

[11] P. W. Anderson, "New approach to the theory of superexchange interactions," *Phys. Rev.* **115** (1959) 2. 7

[12] J. Goodenough, *Magnetism and the Chemical Bond*. J. Wiley & Sons, New York, 1963. 7

[13] W. Geertsma and D. Khomskii, "Influence of side groups on the 90^o superexchange: A modification to the Goodenough-Kanamori-Anderson rules," *Phys. Rev. B* **54** (1996) 3011. 7

[14] G. S. Uhrig, "Habilitationsschrift," Universität zu Köln, 1999. 8

[15] J. Goldstone, A. Salam, and S. Weinberg, "Broken symmetries," *Phys. Rev.* **127** (1962) 965. 8

[16] P. W. Anderson *Science* **235** (1987) 1196. 8

[17] S. Liang, B. Doucot, and P. W. Anderson, "Some new variational resonating-valence-bond-type wave functions for the spin-1/2 antiferromagnetic heisenberg model on a square lattice," *Phys. Rev. Lett.* **61** (1988) 365. 8

[18] H. Bethe, "Zur Theorie der Metalle, I. Eigenwerte und Eigenfunktionen der linearen Atomkette," *Z. Phys.* **31** (1931) 205. 9

[19] N. D. Mermin and H. Wagner, "Absence of ferromagnetism or antiferromagnetism in one- or two-dimensional isotropic heisenberg models," *Phys. Rev. Lett.* **17** (1966) 1133. 9

[20] J. des Cloiseaux and J. J. Pearsons, "Spin-wave spectrum of the antiferromagnetic linear chain," *Phys. Rev.* **128** (1962) 2131. 9

[21] L. D. Faddeev and L. A. Takhtajan, "What is the spin of a spin wave?," *Phys. Lett. A* **85** (1981) 375. 9

[22] G. Müller, H. Thomas, H. beck, and J. Bonner, "Quantum spin dynamics of the antiferromagnetic linear chain in zero and nonzero magnetic field," *Phys. Rev. B* **24** (1981) 1429. 10

[23] C. K. Majumdar, "Antiferromagnetic model with known ground state," *J. Phys. C* **3** (1970) 911. 10

[24] B. S. Shastry and B. Sutherland, "Excitation spectrum of a dimerized next-neighbor antiferromagnetic chain," *Phys. Rev. Lett.* **47** (1981) 964. 11

[25] T. Tonegawa and I. Harada, "Ground-state properties of the one-dimensional isotropic spin-1/2 heisenberg antiferromagnet with competing interactions," *J. Phys. Soc. Jp.* **56** (1987) 2153. 11

[26] K. Okamoto and K. Nomura, "Fluid-dimer critical point in s = antiferromagnetic heisenberg chain with next nearest neighbor interactions," *Phys. Lett. A* **169** (1992) 433. 11

[27] G. S. Uhrig, F. Schönfeld, M. Laukamp, and E. Dagotto, "Unified quantum mechanical picture for confined spinons in dimerized and frustrated spin s=1/2 chains," *Eur. Phys. J. B* **7** (1999) 67. 12

[28] I. Affleck, "Soliton confinement and the excitation spectrum of spin-peierls antiferromagnets," in *Dynamical Properties of Unconventional Magnetic Systems, NATO ASI Series E*, vol. 349, (Dordrecht), p. 123, 1998. cond-mat/9705127. 12

[29] R. B. Laughlin, "Evidence for quasiparticle decay in photoemission from underdoped cuprates," *Phys. Rev. Lett.* **79** (1997) 1726. 13

[30] G. S. Uhrig, "Symmetry and dimension of the magnon dispersion of inorganic spin-peierls systems," *Phys. Rev. Lett.* **79** (1997) 163. 13

[31] G. Bouzerar, A. P. Kampf, and F. Schönfeld, "Magnetic excitations in the spin-peierls system $CuGeO_3$," *cond-mat/9701176* (1997). unpublished. 13

[32] G. Bouzerar, A. P. Kampf, and G. I. Japaridze, "Elementary excitations in dimerized and frustrated Heisenberg chains," *Phys. Rev. B* **58** (1998) 3117. 13

[33] K. P. Schmidt, C. Knetter, and G. S. Uhrig, "Spectral properties of the dimerized and frustrated s=1/2 chain," *Phys. Rev. B* **69** (2004) 104417. 14, 67, 73

[34] E. Dagotto, J. Riera, and D. Scalapino, "Superconductivity in ladders and coupled planes," *Phys. Rev. B* **45** (1992) 5744. 14

[35] F. D. M. Haldane, "Continuum dynamics of the 1-d Heisenberg antiferromagnet: Identification with the O(3) nonlinear sigma model," *Phys. Lett. A* **93** (1983) 464. 15

[36] E. Dagotto and T. M. Rice, "Surprises on the way from one- to two-dimensional quantum magnets: The ladder materials," *Science* **271** (1996) 618. 15

[37] D. C. Johnston, "Antiferromagnetic exchange in two-leg spin-1/2 ladders," *Phys. Rev. B* **54** (1996) 13009. 15

[38] Z. Hiroi, M. Azuma, M. Takano, and Y. Bando, "A new homologous series $Sr_{n-1}Cu_{n+1}O_{2n}$ found in the SrO—CuO system treated under high pressure," *J. Sol. Stat. Chem* **95** (1995) 230. 15

[39] T. Nagata, M. Uehara, J. Goto, J. Akimitsu, N. Motoyama, H. Eisaki, S. Uchida, H. Takahashi, T. Nakanishi, and N. Môri, "Pressure-induced dimensional crossover and superconductivity in the hole-doped two-leg ladder compound $Sr_{14-x}Ca_xCu_{24}O_{41}$," *Phys. Rev. Lett.* **106** (1998) 1090. 15

[40] M. Azuma, Z. Hiroi, M. Takano, K. Ishida, and Y. Kitaoka, "Observation of a spin gap in $SrCu_2O_3$ comprising spin-1/2 quasi-1d two-leg ladders," *Phys. Rev. Lett.* **73** (1994) 3463. 15

[41] A. Gößling, U. Kuhlmann, C. Thomsen, A. Löffert, C. Gross, and W. Assmus, "Magnetic exitations in $SrCu_2O_3$: a Raman scattering study," *Phys. Rev. B* **67** (2003) 52403. 15

[42] K. Schmidt, A. Gössling, U. Kuhlmann, C. Thomsen, A. Löffert, C. Gross, and W. Assmus, "Raman response of magnetic excitations in cuprate ladders and planes," *Phys. Rev. B* **72** (2005) 094419. 15

[43] R. F. Peierls, *Quantum Theory of Solids*. Claredon, Oxford, 1955. 15

[44] J. W. Bray, H. R. Hart, Jr., L. V. Interrante, I. S. Jacobs, J. S. Kasper, G. D. Watkins, S. H. Wee, and J. C. Bonner, "Observation of a spin-peierls transition in a heisenberg antiferromagnetic linear-chain system," *Phys. Rev. Lett.* **35** (1975) 744. 16

[45] D. A. D. Poilblanc, "Dynamical properties of low-dimensional $CuGeO_3$ and NaV_2O_5 spin-peierls systems," *Eur. Phys. J. B* **1** (1998) 19. 16

[46] G. S. Uhrig and B. Normand, "Magnetic properties of $(VO)_2P_2O_7$ from frustrated interchain coupling," *Phys. Rev. B* **58** (1998) 14705. 16, 66

[47] D. Augier, D. Poilblanc, E. Sørensen, and I. Affleck, "Dynamical effects of phonons on soliton binding in spin-peierls systems," *Phys. Rev. B* **58** (1998) 9110. 16

[48] M. Hase, I. Terasaki, and K. Uchinokura, "Observation of the spin-peierls transition in linear Cu^{2+} (spin-1/2) chains in an inorganic compound $CuGeO_3$," *Phys. Rev. Lett.* **70** (1993) 3651. 16

[49] M. C. Cross and D. S. Fisher, "A new theory of the spin-peierls transition with special relevance to the experiments on TTFCuBDT," *Phys. Rev. B* **19** (1979) 402. 16

[50] J. Fivez, B. D. Raedt, and H. D. Raedt, "Low-temperature phonon dynamics of a classical compressible heisenberg chain," *J. Phys. C* **14** (1981) 2923. 16

[51] C. Gros and R. Werner, "Dynamics of the peierls-active phonon modes in $CuGeO_3$," *Phys. Rev. B* **58** (1998) 14677. 16

[52] G. S. Uhrig and B. Normand, "Magnetic properties of $(VO)_2P_2O_7$: Two-plane structure and spin-phonon interactions," *Phys. Rev. B* **63** (2001) 134418. 16, 17, 66, 67, 68, 70, 71, 73

[53] C. V. Raman, "A change of wavelength in light scattering," *Nature* **121** (1928) 619. 17

[54] T. C. Damen, S. P. S. Porto, and B. Tell, "Raman effect in zinc oxide," *Phys. Rev.* **142** (1966) 570. 18

[55] M. G. Cottam and D. J. Lockwood, *Light scattering in Magnetic Solids*. J. Wiley & Sons, New York, 1986. 18, 20

[56] M. Cardona, "Resonance phenomena," in *Light Scattering in Solids II* (M. Cardona and G. Güntherodt, eds.). Springer-Verlag, Berlin, 1982. 19, 20

[57] W. Hayes and R. Loudon, *Scattering of Light by Crystals*. J. Wiley & Sons, New York, 1978. 20

[58] T. Moriya, "Theory of light scattering by magnetic crystals," *J. Phys. Soc. Jp.* **23** (1967) 490. 20

[59] P. Fleury and R. Loudon, "Scattering of light by one- and two-magnon excitations," *Phys. Rev.* **166** (1968) 514. 20, 21

[60] G. Els, P. H. M. van Loosdrecht, P. Lemmens, H. Vonberg, G. Güntherodt, G. S. Uhrig, O. Fujita, J. Akimitsu, G. Dhalenne, and A. Revcolevschi, "Observation of three-magnon light scattering in cugeo3," *Phys. Rev. Lett.* **79** (1997) 5138. 21

[61] J. D. Barnett, S. Block, and G. J. Piermarini, "An optical fluorescence system for quantitative pressure measurement in the diamond-anvil cell," *Rev. Sci. Instrum.* **44** (1973) 1. 25

[62] H. K. Mao, J. Xu, and P. M. Bell, "Calibration of the ruby pressure gauge to 800 kbar under quasi-hydrostatic conditions," *J. Geophys. Res* **91** (1986) 4673. 25

[63] L. Viña, S. Logothetidis, and M. Cardona, "Temperature dependence of the dielectric function of germanium," *Phys. Rev. B* **30** (1984) 1979. 25

[64] H. K. Mao, R. J. Hemley, Y. Wu, A. P. Jephcoat, L. W. Finger, C. S. Zha, and W. A. Bassett, "High-pressure phase diagram and equation of state of solid helium from single-crystal x-ray diffraction to 23.3 GPa," *Phys. Rev. Lett.* **60** (1988) 2649. 26

[65] M. Azuma, T. Saito, Y. Fujishiro, Z. Hiroi, M. Takano, F. Izumi, T. Kamiyama, T. Ikeda, Y. Narumi, and K. Kindo, "High-pressure form of $(VO)_2P_2O_7$: A spin-1/2 antiferromagnetic alternating-chain compound with one kind of chain and a single spin gap," *Phys. Rev. B* **60** (1999) 10145. 29, 33, 58, 69, 79

[66] B. K. Hodnett *Catal. Rev.– Sci. Eng.* **27** (1985) 373. 29

[67] A. V. Prokofiev, F. Büllesfeld, and W. Assmus, "Growth of vanadyl pyrophosphate single crystals," *Crystal Research and Technology* **33** (1998) 157. 29

[68] Y. E. Gorbunova and S. A. Linde, "Structure of vanadyl pyrophosphate $(VO)_2P_2O_7$ crystals," *Soviet Physics Doklady* **24** (1979) 138. 29

[69] P. Nguyen, R. Hoffman, and A. Sleight, "Structure of $(VO)_2P_2O_7$," *Materials Research Bulletin* **30** (1995) 1055. 29, 79

[70] S. Geupel, K. Pilz, S. van Smaalen, F. Büllesfeld, A. V. Prokofiev, and W. Assmus, "Synchrotron-radiation study of the two-leg spin ladder $(VO)_2P_2O_7$ at 120 k," *Acta Cryst. C* **58** (2002) i9. 29, 58, 79

[71] J. C. Bonner, H. W. J. Blöte, J. W. Bray, and I. S. Jacobs, "Susceptibility calculations for alternating antiferromagnetic chains," *J. Appl. Phys.* **50** (1979) 1810. 31

[72] A. W. Garrett, S. E. Nagler, T. Barnes, and B. C. Sales, "Neutron-scattering study of magnetic exitations in $(VO)_2P_2O_7$," *Physical Review B* **55** (1997) 3631. 32

[73] R. S. Eccleston, T. Barnes, J. Brody, and J. W. Johnson, "Inelastic neutron scattering from the spin ladder compound $(VO)_2P_2O_7$," *Phys. Rev. Letters* **73** (1994) 2626. 32

[74] A. W. Garrett, S. E. Nagler, D. A. Tennant, B. C. Sales, and T. Barnes, "Magnetic excitations in the $S = 1/2$ alternating chain compound $(VO)_2P_2O_7$," *Phys. Rev. Lett.* **79** (1997) 745. 32, 34, 65, 67, 73

[75] G. Uhrig and H. Schulz, "Magnetic excitation spectrum of dimerized antiferromagnetic chains," *Phys. Rev. B* **54** (1996) 9624. 32, 65

[76] D. A. Tennant, S. E. Nagler, A. W. Garrett, T. Barnes, and C. C. Toradi, "Excitation spectrum and superexchange pathways in the spin dimer $VODPO_4 \cdot \frac{1}{2}D_2O$," *Phys. Rev. Lett* **78** (1997) 4998. 33

[77] J. Kikuchi, K. Motoya, T. Yamauchi, and Y. Ueda, "Coexistence of double alternating antiferromagnetic chains in $(VO)_2P_2O_7$: NMR study," *Phys. Rev. B* **60** (1999) 6731. 33

[78] T. Yamauchi, Y. Narumi, J. Kikuchi, Y. Ueda, K. Tatani, T. C. Kobayashi, K. Kindo, and K. Motoya, "Two gaps in $(VO)_2P_2O_7$: Observation using high-field magnetization and nmr," *Phys. Rev. Lett.* **83** (1999) 3729. 33

[79] Z. Hiroi, M. Azuma, Y. Fujishiro, T. Saito, M. Takano, F. Izumi, T. Kamiyama, and T. Ikeda, "Structural study of the quantum-spin chain compound $(VO)_2P_2O_7$," *J. of Solid State Chemistry* **146** (1999) 369–379. 33

[80] Y. Narumi, S. Kimura, S. Hirai, K. Kindo, H. Schwenk, S. Schmidt, B. Wolf, B. Lüthi, T. Saito, M. Azuma, and M. Takano, "High-field magnetisation measurements on single crystals of $(VO)_2P_2O_7$," *Physica B* **294** (2001) 71. 34, 69

[81] D. L. Rousseau, R. P. Bauman, and S. P. S. Porto, "Normal mode determination in crystals," *J. Raman Spectr.* **10** (1981) 253. 35

[82] U. Kuhlmann, C. Thomsen, A. V. Prokofiev, F. Büllesfeld, E. Uhrig, and W. Assmus, "Polarized Raman and infrared vibrational analysis of $(VO)_2P_2O_7$ single crystals," *Physica B* **301** (2001) 276. 43, 53

[83] U. Kuhlmann, C. Thomsen, A. V. Prokofiev, F. Büllesfeld, E. Uhrig, M. Anton, C. Gross, and W. Assmus, "Phonon anomalies in the two phases of the low-dimensional spin compound $(VO)_2P_2O_7$," *Phys. Rev. B* **66** (2002) 064420. 43

[84] C. Julien, I. Ivanov, and A. Gorenstein, "Vibrational modifications on lithium intercalation in V_2O_5 films," *Materials Science and Engineering* **B33** (1995) 168. 44

[85] J. Gaubicher, Y. Chabre, J. Angenault, A. Lautié, and M. Quarton, "Lithium electrochemical intercalation in $\beta - VOSO_4$," *J. of Alloys and Compounds* **262-263** (1997) 34. 44

[86] V.P. Mahadevan Pillai, B. R. Thomas, V. Nayar, and K.-H. Lii, "Infrared and Raman spectra of $Cs_2VOP_2O_7$ and single crystal $Rb_2(VO)_3P_2O_7$," *Spectrochimica Acta Part A* **55** (1999) 1809. 44, 45, 47

[87] P. Clauws, J. Broeckx, and J. Vennik, "Lattice vibrations of V_2O_5.," *Phys. stat. sol. b* **131** (1985) 459. 44

[88] X. Zhang and R. Frech, "Vibrational spectroscopic study of lithium vanadium pentoxides.," *Electrochimica Acta* **42** (1997) 475. 44

[89] Z.V. Popović and M.J. Konstantinović and R. Gajić and V. Popov and Y. S. Raptis and A.N. Vasil'ev and M. Isobe and Y. Ueda, "Lattice vibrations in spin-peierls compound NaV_2O_5," *Solid State Commun.* **110** (1999) 381. 44, 59, 64

[90] M. Calatayud, . J. Andrés, and A. Beltrán, "A systematic density functional theory study of $V_xO_y^+$ and V_xO_Y (X = 2-4, Y = 2-10) systems," *J. Phys. Chem. A* **105** (2001) 9760. 44

[91] E. Steger and C. Fischer-Bartelk, "Das Schwingungsspektrum des Dihydrogen-diphosphat-Anions," *Z. anorg. allg. Chemie* **338** (1965) 15. 44

[92] H. Eysel and K. T. Lim, "Raman intensities of phosphate and diphosphate ions in aqueous solution.," *J. of Raman Spectroscopy* **19** (1988) 535. 44

[93] W. Bues and H.-W. Gehrke, "Schwingungsspektren von Schmelzen, Gläsern und Kristallen des Natrium-di-, tri- und -tetraphosphats.," *Z. anorg. allg. Chem.* **288** (1956) 291. 44, 45

[94] W. Bues, K. Bühler, and P. Kuhnle, "Raman-Spektren von Diphosphat, Diarsenat und deren Gemische in der Schmelze.," *Z. anorg. allg. Chem.* **325** (1963) 8. 44

[95] A. Hezel and S. Ross, "The vibrational spectra of some divalent metal pyrophosphates," *Spectrochimica Acta* **23A** (1967) 1583. 45

[96] B. Cornilsen and R. Condrate, "The vibrational spectra of α-alkaline earth pyrophosphates," *J. of Solid State Chemistry* **23** (1978) 375. 45, 47

[97] B. Cornilsen and R. Condrate, "The vibrational spectra of $\beta - Ca_2P_2O_7$ and $\gamma - Ca_2P_2O_7$," *J. inorg. nucl. Chem.* **41** (1979) 602. 45, 47

[98] B. Cornilsen, "Solid state vibrational spectra of calcium pyrophosphate dihydrate," *J. of Molecular Structure* **117** (1984) 1. 45, 47

[99] N. Santha, V. Nayar, and G. Keresztury, "Vibrational spectra of $M^{II}_3Pb(P_2O_7)_2(M^{II} = Ni, Co)$," *Spectrochimica Acta* **49A** (1993) 47. 45, 47

[100] E. Baran, I. Botto, and A. Nord, "The vibrational Spectrum and the Conformation of the $P_2O_7^{4-}$ Anion in $Fe_2P_2O_7$," *J. of Molecular Structure* **143** (1986) 151. 47

[101] I. Loa, U. Schwarz, M. Hanfland, and R. Kremer, "Crystal structure and optical spectroscopy of NaV_2O_5 under pressure.," *Phys. stat. sol. b* **215** (1999) 709. 49, 52

[102] I. Loa, K. Syassen, and R. Kremer, "Vibrational properties of NaV_2O_5 under high ressure studied by Raman spectroscopy.," *Solid State Commun.* **112** (1999) 681. 49, 52

[103] P. Daniels priv. commun., 2001. 50

[104] M. Grove, P. Lemmens, G. Güntherodt, B. C. Sales, F. Büllesfeld, and W. Assmus, "Magnetoelastic coupling and spin excitations in the spin-gap system $(VO)_2P_2O_7$," *Phys. Rev. B* **61** (2000) 6126. 50, 55, 65, 66, 67

[105] R. Zallen, "Pressure-raman effects and vibrational scaling laws in molecular crystals: S_8 and As_2S_3," *Phys. Rev. B* **9** (1974) 4485. 53, 54

[106] Z. M. Jakšić, "Temperature and pressure dependence of phonon frequencies in GeS_2, $GeSe_2$, and $SnGeS_3$," *phys. stat. sol. (b)* **239** (2003) 131. 53

[107] R. Zallen and M. L. Slade, "Influence of pressure and temperature on phonons in molecular chalcogenides: Crystalline As_4S_4 and S_4N_4," *Phys. Rev. B* **18** (1978). 53

[108] W. Smith and T. R. Forester *J. Molec. Graphics* **14** (1996) 136. 58

[109] W. Cochran, "Theory of the lattice vibrations of germanium," *Proc. R. Soc. A* **253** (1959) 260. 59

[110] G. Dolling and R. A. Cowley, "The thermodynamics and optical properties of germanium, silicon, diamond, and gallium arsenide," *Proc. Phys. Soc* **88** (1966) 463. 59

[111] W. Weber, "New bond-charge model for the lattice dynamics of diamond-type semiconductors," *Phys. Rev. Lett.* **33** (1974) 371. 59

[112] F. Ritschl, M. Fait, K. Fiedler, J. E. H. Köhler, B. Kubias, and M. Meisel, "An extension of the Consistent Valence Force Field (CVFF) with the aim to simulate the structures of vanadium phosphorus oxides and the adsorption of n-butane and of 1-butene on their crystal planes," *Z. Anorg. Allg. Chem.* **682** (2002) 1385. 59

[113] W. Kress, U. Schröder, J. Prade, A. D. Kulkarni, and F. W. de Wette, "Lattice dynamics of the high-T_c superconductor $YBa_2Cu_3O_{7-x}$," *Phys. Rev. B* **38** (1988) 2906. 60

[114] A. D. Kulkarni, J. Prade, F. W. de Wette, W. Kress, and U. Schröder, "Calculation of raman- and infrared-active modes of $Tl_2CaBa_2Cu_2O_x8$," *Phys. Rev. B* **40** (1989) 2642. 60

[115] E. Rampf, U. Schröder, F. W. de Wette, A. D. Kulkarni, and W. Kress, "Lattice dynamics of Nd_2CuO_4," *Phys. Rev. B* **48** (1993) 10143. 60, 64

[116] P. Y. Yu and M. Cardona, *Fundamentals of Semiconductors*. Springer-Verlag, Berlin, 1996. 60, 62

[117] S. Sanguinetti, G. Benedek, M. Righetti, and G. Onida, "Dynamical properties and related optical spectra of fullerenes: The bond-charge-model description," *Phys. Rev. B* **50** (1994) 6743. 62

[118] U. Kuhlmann, C. Thomsen, A. V. Prokofiev, F. Büllesfeld, E. Uhrig, and W. Assmus, "Raman scattering of magnetic excitations of independent antiferromagnetic spin chains in $(VO)_2P_2O_7$," *Phys. Rev. B* **62** (2000) 12262. 66

[119] T. Saito, T. Terashima, M. Azuma, M. Tanako, T. Goto, H. Ohta, W. Utsumi, P. Bordet, and D. C. Johnston, "Single crystal growth of the high pressure phase of $(VO)_2P_2O_7$," *Journal of Solid State Chemistry* **153** (2000) 124. 69

[120] D. C. Johnston, T. Saito, M. Azuma, M. Takano, T. Yamauchi, and Y. Ueda, "Modeling of the magnetic susceptibilities of the ambient and high-pressure phases of $(VO)_2P_2O_7$," *Phys. Rev. B* **64** (2001) 134403. 69

[121] U. Kuhlmann, C. Thomsen, A. V. Prokofiev, F. Büllesfeld, E. Uhrig, M. Anton, C. Gross, and W. Assmus, "Spin-phonon coupling in the high pressure phase of the low-dimensional spin compound $(VO)_2P_2O_7$," *phys. stat. sol. (a)* **196** (2003) 185. 69

[122] U. Fano, "Effects of configuration interaction on intensities and phase shifts," *Phys. Rev.* **124** (1961) 1866. 70

[123] C. Thomsen, "Light scattering in high-Tc superconductors," in *Light Scattering in Solids* (M. Cardona and G. Güntherodt, eds.), vol. VI, p. 285. Springer Verlag, Heidelberg, 1991. 70

[124] B. Wolf, "Thermodynamic and magnetoelastic investigations on high-pressure $(VO)_2P_2O_7$: Inconsistencies with a dimerized spin chain." Seminar talk held on the international workshop on collective quantum states in low-dimensional transition metal oxides, Dresden, February 22 - 25, 2005. 77

Acknowledgments

I would like to thank the people who contributed to this thesis, especially

my advisor Prof. Dr. Christian Thomsen for his continuous support and the pleasant experience of working for him, including "pilgrimage" to Kloster Walberberg and adventures in international relations during QT100.

Prof. Dr. Wolfgang Richter for reviewing this thesis.

Prof. Dr. Andreas Knorr for being the chairman of my thesis committee.

The members of Prof. Thomsen's group, in particular Bernd Schöler for his nevertiring willingness to realize my small mechanical inventions and for all the nice chats we had.

Sabine Bahrs, Christian Kristukat, María Machón and Janina Maultzsch for their cooperative support and the marvellous "Nachprüfung" they gave me.

Last not least many thanks to Alexander Gößling for the fruitful cooperation and the nice time we spent together - there's still some beer outstanding.

Prof. Dr. Frank Behrendt for giving me the opportunity to broaden my experience by harboring me for one year in his group, and for giving me any support for finishing this thesis.

All members of Prof. Behrendt's group for the friendly welcome and the nice atmosphere.

The Frankfurt people C. Gross and A. Löffert for their efforts of growing the superb VPO samples.

Thalia Deniozou for proofreading and ... *so much more*.